Structural and thermodynamic analyses of the β-to-α transformation in RfaH reveal principles of fold-switching proteins

Philipp K. Zuber[1]†, Tina Daviter[2]‡, Ramona Heißmann[1], Ulrike Persau[1], Kristian Schweimer[1], Stefan H. Knauer[1]*

[1] Biochemistry IV – Biophysical Chemistry, University of Bayreuth, Universitaetsstrasse 30, 95447 Bayreuth, Germany.

[2] Birkbeck, University of London, Malet Street, Bloomsburry, London WC1E 7HX, United Kingdom.

† Present address: MRC Laboratory of Molecular Biology, Francis Crick Avenue, Cambridge Biomedical Campus, Cambridge CB2 0QH, United Kingdom

‡Present address: The Institute of Cancer Research, 237 Fulham Road, London SW3 6JB, United Kingdom.

* For correspondence: stefan.knauer@uni-bayreuth.de

Abstract

The two-domain protein RfaH, a paralog of the universally conserved NusG/Spt5 transcription factors, is regulated by autoinhibition coupled to the reversible conformational switch of its 60-residue C-terminal KOW domain between an α-hairpin and a β-barrel. In contrast, NusG/Spt5-KOW domains only occur in the β-barrel state. To understand the principles underlying the drastic fold switch in RfaH, we elucidated the thermodynamic stability and the structural dynamics of two RfaH- and four NusG/Spt5-KOW domains by combining biophysical and structural biology methods. We find that the RfaH-KOW β-barrel is thermodynamically less stable than that of most NusG/Spt5-KOWs and we show that it is in equilibrium with a globally unfolded species, which, strikingly, contains two helical regions that prime the transition towards the α-hairpin. Our results suggest that transiently structured elements in the unfolded form might drive the global folding transition in metamorphic proteins in general.

Introduction

Fundamental understanding of how proteins fold has ever been one of the most important questions in structural biology and it is still not answered, despite recent progress in protein structure prediction (Jumper et al., 2021; Tunyasuvunakool et al., 2021). Since the formulation of the "thermodynamic hypothesis of protein folding" by Anfinsen (Epstein et al., 1963) it has been generally accepted that the amino acid sequence of a protein determines its three-dimensional structure and that a protein adopts only a single folded conformation, which is referred to as physiological state and which corresponds to its global energy minimum. This conformation, in turn, fulfills one distinct function. While this "one sequence – one structure – one function" dogma holds true for most well-folded (globular) proteins, it has been challenged by several discoveries over the past decades. Among those are, for instance, (i) moonlighting proteins, which fulfill two completely unrelated functions (Jeffery, 2014, 1999), (ii) intrinsically disordered proteins (IDPs), which do not adopt a defined secondary or tertiary structure at all, but sample an ensemble of sterically allowed conformations instead (van der Lee et al., 2014), and (iii), most strikingly, metamorphic proteins (also referred to as fold-switching proteins), which can reversibly interconvert between at least two well-defined conformations, sometimes in response to a molecular signal (Murzin, 2008).

The free energy landscape of globular, well-folded proteins is often portrayed as a rugged funnel, with the "rim" corresponding to the multitude of random-coil structures of the "unfolded state" (U state) and the deepest point (global minimum in Gibb's free energy, *G*), representing the "native" or "physiological" state (N state). IDPs, in contrast, exhibit a rather flat energy landscape and no specific conformation is favored, i.e. significantly populated. Fold-switching proteins are thought to reside in-between these two scenarios, that is their energy landscape may

be funnel-like, but it shows at least two major minima, each representing a distinct, well-folded conformation. The various conformations of a fold-switching protein may differ in the following aspects: (i) the type of secondary structure (α-helices, β-strands, …), (ii) the extent of secondary structure elements, and (iii) the tertiary structure, usually in combination with (i) and/or (ii) (Dishman and Volkman, 2018; Kim and Porter, 2021). Additionally, these states often exhibit different quaternary structures, e.g. monomeric in one state *vs*. multimeric in another state.

A particularly intriguing example of fold-switching proteins is the transcription factor RfaH from *E. coli* (*Ec*RfaH), a member of the universally conserved family of NusG (bacteria) / Spt5 (archaea and eukaryotes) proteins (Werner, 2012). NusG/Spt5 proteins exhibit a modular structure with several domains. Bacterial NusG consists of at least an N-terminal domain and a C-terminal Kyrpides, Ouzounis, Woese (KOW) domain connected by a flexible linker (Werner, 2012). Spt5 proteins contain a NusG-like N-terminal (NGN) domain and one (archaea) or several (eukaryotes) KOW domains (Werner, 2012). All structurally characterized NusG/Spt5-KOW domains adopt a five-stranded β-barrel structure (**Figure 1A**; see e.g. (Klein et al., 2011; Meyer et al., 2015; Mooney et al., 2009; Zuber et al., 2018)).

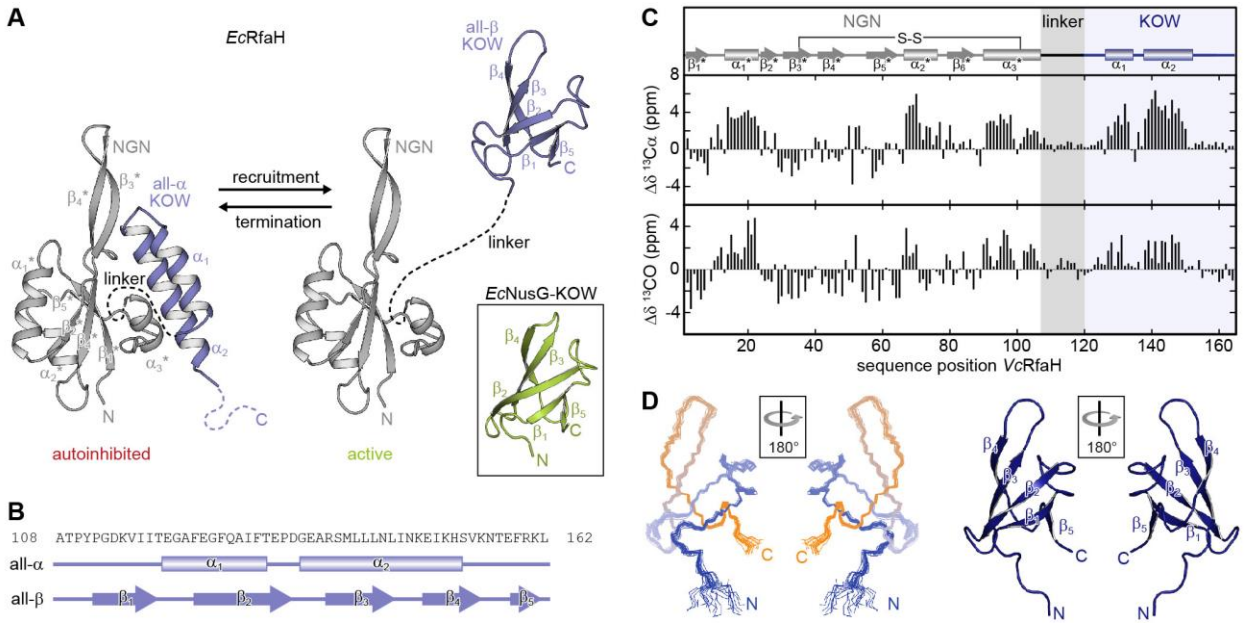

Figure 1. Fold-switching within the NusG/RfaH family. (**A**) Cartoon representation of *Ec*RfaH in the closed, autoinhibited state (left; protein data bank identifier (PDB-ID): 5OND) and in the open, active conformation (right; PDB-ID all-β *Ec*RfaH-KOW: 2LCL) and of *Ec*NusG-KOW (boxed; PDB-ID: 2JVV). Unstructured regions are shown as dashed lines, termini are labeled. (**B**) Secondary structures of *Ec*RfaH-KOW in the all-α and the all-β state. Tubes indicate α-helical elements, arrows represent β-strands. The amino acid sequence is shown above. (**C**) Secondary chemical shift of *Vc*RfaH. The plots show the difference between the observed chemical shift and the corresponding predicted random coil value of ^{13}Cα (top) and ^{13}CO (bottom). Positive values indicate helical, negative values elongated (β-sheet) structures, and values close to zero are observed for random coil-like structures. The secondary structure elements inferred from the analysis are shown above the graphs (code for secondary structure elements as in (B)). The position of the identified disulfide bridge (see also **Figure 1 – Figure supplement 1A, B)** is indicated. (**D**) Left: Ribbon representation of the 20 lowest energy structures of *Vc*RfaH-KOW (PDB-ID: 6TF4). Right: Cartoon representation of the lowest energy structure. β-strands and termini are labeled.

Figure supplement 1. Disulfide bridge formation in *Vc*RfaH.

Figure supplement 2. Solution structure statistics for *Vc*RfaH-KOW.

Figure supplement 3. Structure comparison of KOW domains used in this study.

*Ec*RfaH is an operon-specific paralog of *E. coli* NusG (*Ec*NusG) and – just like *Ec*NusG – consists of an NGN domain that is loosely connected with a KOW domain *via* a flexible 15 amino acid long linker. However, in free *Ec*RfaH *Ec*RfaH-KOW folds as an α-helical hairpin (all-α state) that interacts with the *Ec*RfaH-NGN domain. Thus, the binding site for RNA

polymerase (RNAP) at the domain interface on *Ec*RfaH-NGN is masked and *Ec*RfaH is locked in an autoinhibited state (Belogurov et al., 2007). Upon recruitment to a transcription elongation complex pausing at an *operon polarity suppressor* (*ops*) site, *Ec*RfaH is activated (Artsimovitch and Landick, 2002; Zuber et al., 2019): the domains dissociate and the liberated *Ec*RfaH-KOW refolds into a NusG-KOW-like β-barrel (all-β state; **Figure 1A, B**) (Burmann et al., 2012; Zuber et al., 2019).

The refolding occurs spontaneously as soon as the domains are separated and *Ec*RfaH-KOW, when produced as an isolated domain, also adopts the all-β state, implying that the all-α fold is only stable in the presence of *Ec*RfaH-NGN (Burmann et al., 2012; Tomar et al., 2013). Each of the *Ec*RfaH-KOW states has a specific function: the all-α state prevents off-target recruitment of *Ec*RfaH and competition with the general transcription factor NusG (Belogurov et al., 2007), whereas the all-β *Ec*RfaH-KOW serves as recruitment platform for ribosomes to activate translation (Burmann et al., 2012; Zuber et al., 2019). Upon release from RNAP *Ec*RfaH is transformed back into its autoinhibited state, i.e. the structural switch of *Ec*RfaH-KOW is fully reversible (Zuber et al., 2019). *Ec*RfaH was not only considered a fold-switching protein, but termed a “transformer protein” to emphasize, that a complete domain cycles reversibly between two states with radically different stable secondary/tertiary structure and with each state performing a distinct function (Knauer et al., 2012).

The fine-tuned mechanism used by *Ec*RfaH to control its functions may be widespread in nature (Porter and Looger, 2018). However, the molecular principles underlying the fold-switching process are only poorly understood. Here, we present a comprehensive thermodynamic and structural analysis of six KOW domains from NusG/Spt5/RfaH proteins from all domains of life. We combine circular dichroism (CD) spectroscopy, differential scanning calorimetry (DSC), and

117 solution-state nuclear magnetic resonance (NMR) spectroscopy to gain insight into the
118 mechanism and the dynamics of fold-switching within the RfaH family on a molecular level and
119 provide a rationale for the mechanism of fold-switching proteins in general.

120

Results

Evolutionary conservation of fold-switching within the RfaH family

To date, fold-switching within the RfaH family has only been shown for *Ec*RfaH, although RfaH orthologs seem to employ a similar mechanism to affect RNAP (Carter et al., 2004). Thus, we first asked whether this ability might be a general feature of RfaH proteins. We chose RfaH from *Vibrio cholerae* (*Vc*RfaH) for a structural analysis by solution-state NMR spectroscopy as it is evolutionarily remote from *Ec*RfaH (sequence identity *Ec*/*Vc*RfaH: 43.6 % (full-length) or 35.8 % (KOW domain), respectively). We first identified the secondary structure elements of the full-length protein by performing an NMR backbone assignment and calculating the secondary chemical shift for each $^{13}C\alpha$ and ^{13}CO atom, which depends on the main chain geometry (**Figure 1C**). In full-length *Vc*RfaH, the KOW domain exhibits two stretches with helical structure that are separated by about four residues and the overall pattern of secondary structure elements perfectly matches the one of autoinhibited *Ec*RfaH (Burmann et al., 2012), suggesting similar tertiary structures for *Ec*RfaH and *Vc*RfaH (compare to **Figure 1A**), but with helix α_3* being 1.5 turns longer in *Vc*RfaH. Interestingly, the Cα and Cβ atoms of C34 and C102 exhibit chemical shifts typical for cystines ((Sharma and Rajarathnam, 2000), **Figure 1 – figure supplement 1A**). These residues are located at the end of helix α_3* and in strand β_3*, respectively, and are, most probably, in close proximity, as indicated by the structure of *Ec*RfaH. The addition of a reducing agent to [^{2}H, ^{15}N, ^{13}C]-*Vc*RfaH led to drastic changes of the chemical shifts of C34 and C102 as well as residues in spatial proximity in a [^{1}H, ^{15}N]-heteronuclear single quantum coherence (HSQC) spectrum (**Figure 1 – Figure supplement 1B**). From this we conclude that C34 and C102 form a disulfide bridge, that covalently tethers the α_3*-helix to the core of *Vc*RfaH-NGN, a feature absent in *Ec*RfaH. However, upon refolding from a solution

144 containing 8 M urea and reducing agent, ^{15}N-*Vc*RfaH adopted the same conformation as before
145 denaturation (**Figure 1 – Figure supplement 1C**), suggesting that the disulfide bridge is not
146 required for *Vc*RfaH to fold into the autoinhibited state.

147 Next, we determined the solution structure of the isolated *Vc*RfaH-KOW domain by NMR
148 spectroscopy. *Vc*RfaH-KOW also shows the 5-stranded β-barrel topology typical for NusG/Spt5-
149 KOW domains (**Figure 1D and Figure 1 – Figure supplement 2**), with a Cα root mean square
150 deviation (rmsd) of 1.4 Å as compared to isolated *Ec*RfaH-KOW.

151 Although we do not present functional data on *Vc*RfaH here, these results strongly suggest that
152 *Vc*RfaH-KOW can also switch between an all-α and an all-β state and that *Vc*RfaH is thus, most
153 probably, also a transformer protein.

154

155 **The model systems**

156 The sequence of NusG/Spt5-KOW domains has been evolutionarily optimized to fold in only
157 one defined conformation. Consequently, in the case of RfaH-KOW, the ability to switch
158 between the all-α and the all-β state must be encoded within the primary structure, whereas the
159 "decision" which state to adopt solely depends on the availability of RfaH-NGN (Tomar et al.,
160 2013). Sequence alignments and bioinformatical approaches (Balasco et al., 2015; Bernhardt and
161 Hansmann, 2018; Gc et al., 2014; Joseph et al., 2019; Li et al., 2014; Shi et al., 2017; Xiong and
162 Liu, 2015) gave first hints why RfaH, in contrast to NusG, is a metamorphic protein and how the
163 structural switch might proceed. Yet, experimental evidence is still scarce. Thus, we analyzed
164 isolated KOW domains of six NusG/Spt5 or RfaH proteins to identify characteristic properties of
165 fold-switching proteins and to understand the molecular mechanisms underlying the refolding
166 mechanism of RfaH-KOW. Due to the fact that NusG proteins are universally conserved, we

chose NusG-KOWs from *E. coli* and *Mycobacterium tuberculosis* (*Ec*/*Mt*NusG-KOW), the Spt5-KOW from the hyperthermophilic archaeon *Methanocaldococcus jannaschii* (*Mj*Spt5-KOW) and the fifth KOW domain from human Spt5 (hSpt5-KOW5) as representative NusG-/Spt5-KOWs and the *Ec*/*Vc*RfaH-KOWs as representatives for RfaH proteins. The constructs used are about 65 residues in length and contain the structured region and parts of the neighboring linker(s) (**Figure 1 – Figure supplement 3A**). All six domains exhibit the typical β-barrel topology (**Figure 1 – Figure supplement 3B**) with major differences only in the loops or turns connecting the β-strands (**Figure 1 – Figure supplement 3C**).

Thermal and chemical stability of the KOW domains

Metamorphic proteins that switch between two stable conformations are expected to show two main minima in their energy landscape, each corresponding to one of these states (Dishman and Volkman, 2018). This implicates that (i) in order to control the structural interconversion, one of the conformations has to be (de)stabilized according to a molecular signal, and (ii) the energy minima cannot be as deep as the global minimum of a protein with a single, stable conformation to avoid permanent trapping of one state. Consequently, the all-β RfaH-KOW should show a limited thermodynamic stability to allow facile refolding to the all-α state when RfaH-NGN is available after transcription termination. To test this hypothesis, we analyzed the thermal stability of the six KOW domains by CD-based thermal denaturation experiments (**Figure 2A**) and by DSC (**Figure 2B**) at pH 4 and pH 7. At pH 7 unfolding was reversible for all KOW domains except for hSpt5-KOW5, which showed aggregation; the opposite effect was observed at pH 4 (**Figure 2 – Figure supplement 1**). All observed unfolding transitions were analyzed with a two-state model to determine the melting temperature, T_m, the enthalpy of unfolding at T_m, $\Delta H_u(T_m)$,

and, in case of the DSC thermograms, the temperature-dependent difference in heat capacity between the N and U states, $\Delta C_p(T)$ (**Figure 2C,D and Figure 2 – Figure supplement 2**).

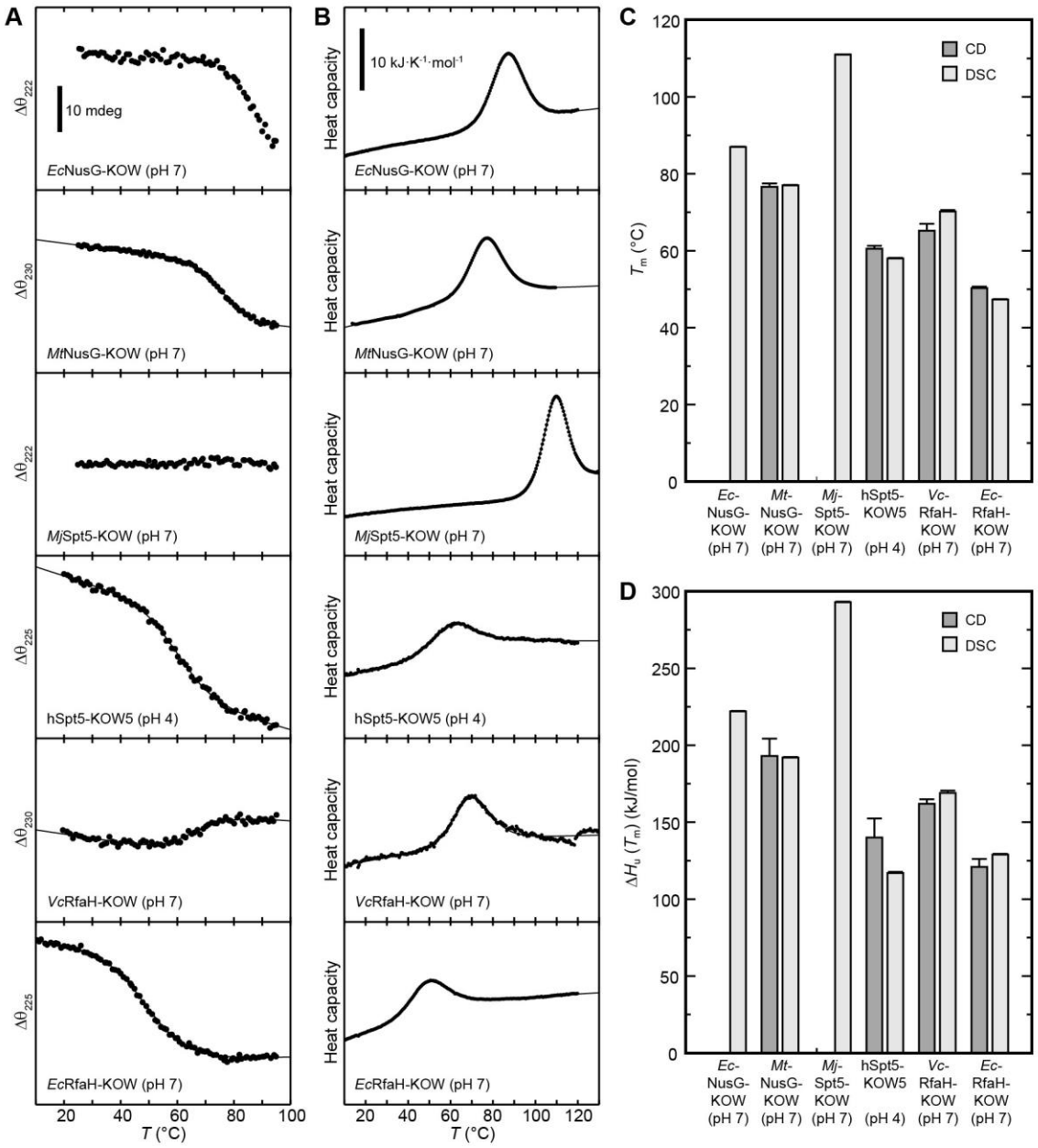

Figure 2. Thermal unfolding experiments of the six KOW domains. (**A**) Thermal unfolding monitored *via* change in the CD signal with a temperature gradient from 20 to 95 °C. The line corresponds to the best fit to a two state-unfolding model. Measurements were carried out with proteins in 10 mM K-acetate (pH 4.0) buffer for hSpt5-KOW5 and in 10 mM K-phosphate (pH 7.0) buffer for all other domains. The wavelength for monitoring the transition was chosen based on the largest difference between the spectra of the folded and unfolded protein. Data for

*Ec*NusG-KOW was not fitted due to the lack of the baseline of the unfolded state. *Mj*Spt5-KOW could not be denatured at all. (**B**) Thermograms obtained from DSC measurements. All profiles are normalized to one molar of protein. The lines correspond to best fits to a two-state unfolding model that includes a *T*-dependent ΔC_p change. Buffers are as in (A). (**C,D**) T_m (**C**) and $\Delta H_u(T_m)$ (**D**) values derived from thermal unfolding experiments monitored by CD and DSC.
Source data 1. Data for thermal denaturation experiments for all KOW domains.
Figure supplement 1. Reversibility of thermal unfolding.
Figure supplement 2. Thermodynamic parameters of the six KOW domains as derived from thermal unfolding experiments using CD spectroscopy and DSC.

Due to the fact that the KOW domains are β-barrels the precision of the thermodynamic parameters determined by CD spectroscopy is not as high as for proteins with helical elements. Nevertheless, the results obtained by DSC and CD spectroscopy are in good agreement showing that *Ec*NusG-KOW, *Mt*NusG-KOW, and *Mj*Spt5-KOW have much higher T_m values (87 °C, 77 °C and 111 °C, respectively) than hSpt5-KOW5 (58-60 °C), *Ec*RfaH-KOW (47-50 °C), and *Vc*RfaH-KOW (65-70 °C). The same trend was observed for $\Delta H_u(T_m)$ values. Consequently, this data indicates that *Ec*NusG-KOW, *Mt*NusG-KOW, and *Mj*Spt5-KOW have a higher thermodynamic stability than Spt5-KOW5, *Ec*RfaH-KOW, and *Vc*RfaH-KOW.

To corroborate and complement the previous findings, we next performed far-UV CD-based chemical unfolding experiments at pH 4 and pH 7 using urea as denaturant (**Figure 3A – F, left**).

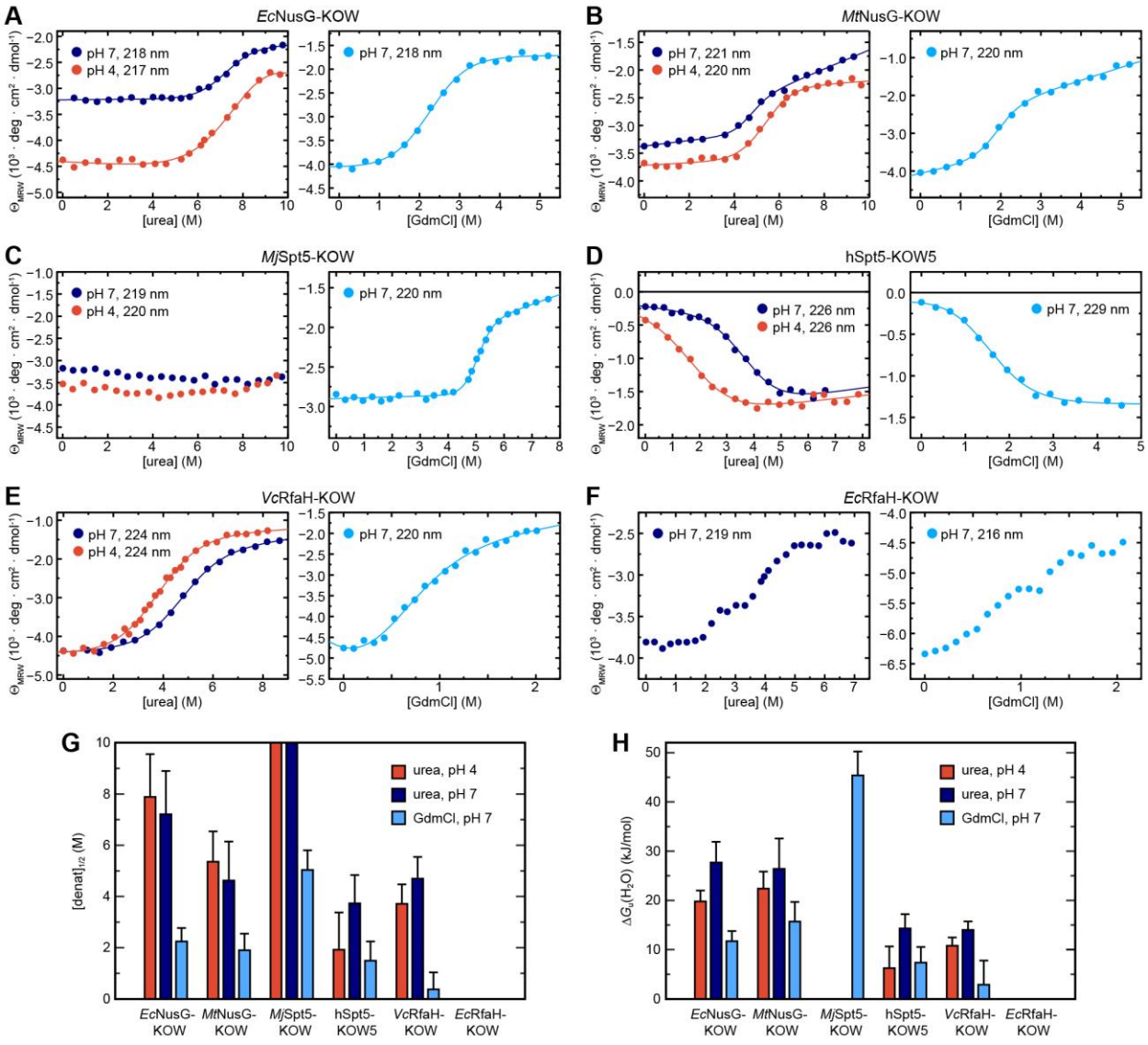

Figure 3. CD spectroscopy-based chemical equilibrium unfolding of the six KOW domains. (**A**) – (**F**): Change in Θ_{MRW} of the indicated protein domain upon over-night incubation with increasing concentrations of (left) urea in 10 mM K-acetate (pH 4.0; red circles) or 10 mM K-phosphate (pH 7.0; dark blue circles), respectively, and (right) GdmCl in 10 mM K-phosphate (pH 7.0; light blue circles). The detection wavelength is indicated and chosen based on the maximum difference between the spectra of the folded and unfolded state. The lines correspond to the best fits to a two-state unfolding model, except for *Ec*RfaH-KOW, which exhibits a three-state unfolding behavior. (**G, H**) Comparison of $[denat.]_{1/2}$ values **(G)** and $\Delta G_u(H_2O)$ values **(H)** of the KOW domains derived from the chemical denaturation experiments shown in (A)-(E).

Source data 1. Data for chemical denaturation experiments for all KOW domains.

Figure supplement 1. Thermodynamic parameters of the six KOW domains.

Figure supplement 2. Chemical unfolding of VcRfaH-KOW monitored by change in Trp fluorescence.

Figure supplement 3. Reversibility of chemical denaturations for all KOW domains.

237 *Ec*NusG-KOW, *Mt*NusG-KOW, hSpt5-KOW5, and *Vc*RfaH-KOW show a sigmoidal unfolding
238 curve at either pH, indicative of a two-state unfolding process. Analysis of this data by the linear
239 extrapolation model yields transition midpoints ($[urea]_{1/2}$ values) and $\Delta G_u(H_2O)$ values that
240 confirm the relative order of the stability as determined by thermal denaturation (**Figure 3G, H,**
241 **Figure 3 – Figure supplement 1, and Figure 2C)**. For *Mj*Spt5-KOW only the native state
242 baseline is observable at both pH values, demonstrating that no denaturation could be achieved
243 and that, consequently, this KOW domain exhibits the highest thermodynamic stability
244 (assuming an *m*-value comparable to that of the other KOW domains, MjSpt5-KOW likely has a
245 $\Delta G_u(H_2O)$ value > 30-40 kJ/mol). Notably, we obtained a $\Delta G_u(H_2O)$ value for hSpt5-KOW5 at
246 pH 7, showing that this domain has a stability comparable to that of *Vc*RfaH-KOW at
247 physiological pH (**Figure 3 – Figure supplement 1**). As *Vc*RfaH-KOW, in contrast to all other
248 KOW domains in this study, contains a Trp residue an additional fluorescence-based denaturation
249 experiment was performed, and the obtained parameters are in good agreement with the CD data
250 (**Figure 3 – Figure supplement 1 and Figure 3 – Figure supplement 2A**).

251 To complement the analysis, we repeated the unfolding experiments at pH 7 using guanidinium
252 chloride (GdmCl; **Figure 3A – F, right, Figure 3 – Figure supplement 1 and Figure 3 –**
253 **Figure supplement 2B**). As GdmCl is a more potent denaturant than urea, we were now able to
254 denature even *Mj*Spt5-KOW, giving a $[GdmCl]_{1/2}$ value of 5.03 M, which is more than twice the
255 value of the next stable protein. In accordance with the urea-based unfolding experiments at pH
256 7, *Mj*Spt5-KOW, *Ec*NusG-KOW and *Mt*NusG-KOW exhibit higher $\Delta G_u(H_2O)$ and $[denat.]_{1/2}$
257 values than *Vc*RfaH-KOW and hSpt5-KOW5, although the relative order of stability of *Mt*NusG-
258 KOW and *Ec*NusG-KOW is swapped. This difference as well as the difference between the
259 absolute $\Delta G_u(H_2O)$ values derived from the urea- and GdmCl-based denaturations is a well-

documented phenomenon and may be attributed to the limited applicability of the linear extrapolation model for the analysis of denaturations by GdmCl (see e.g. (Gupta et al., 1996; Makhatadze, 1999)). Thus, we base our conclusions on the relative comparison of the obtained values. We finally note that chemical unfolding was completely reversible in all cases (**Figure 3 – Figure supplement 3**).

Surprisingly, and in contrast to all other domains, *Ec*RfaH-KOW shows a more complex unfolding curve in both urea- and GdmCl-based denaturation experiments at pH 7, with an additional plateau at ≈3 M urea or ≈1 M GdmCl, respectively, between the N and U baselines (**Figure 3F**; no curve could be obtained at pH 4 due to native state aggregation). This suggests that the unfolding of *Ec*RfaH-KOW may be described *via* a three-step model including an observable equilibrium intermediate that might play an important role in the fold-switching mechanism of *Ec*RfaH-KOW.

In summary, the poor spectroscopic properties of the analyzed domains limit the precision of the absolute values of the thermodynamic parameters obtained from CD experiments. However, our findings reveal clear differences in the global stability of the six domains and allow a grouping into two classes: *Mj*Spt5-KOW and *Ec*/*Mt*NusG-KOW are considered as "stable domains", whereas the β-barrel *Ec*/*Vc*RfaH-KOW as well as hSpt5-KOW5 show a reduced thermodynamic stability.

Regions that are unfolded in all-α RfaH-KOW are destabilized in the all-β conformation

We next asked whether the less stable KOW domains also exhibit local differences in their stability as compared to the NusG-KOWs and *Mj*Spt5-KOW. Therefore, we identified the backbone H-bond pattern in the six domains and quantified the magnitude of the through H-bond

283 coupling constant, $^{h3}J_{NC'}$, by long-range HNCO NMR experiments (**Figure 4 – Figure**
284 **supplement 1**). This parameter is inversely proportional to the length of the H-bond and the
285 deviation from its optimum angle, thus reflecting the H-bond strength (Grzesiek et al., 2004). To
286 allow comparison between the six domains, we grouped H-bonds that are located at equivalent
287 positions of the β-barrels and ordered them according to their position in the individual β-sheets
288 (**Figure 4A, B**). Most $|^{h3}J_{NC'}|$-values are in the range of 0.5 – 0.9 Hz, which is typical for H-
289 bonds of β-sheets (Grzesiek et al., 2004). In line with having the highest T_m, *Mj*Spt5-KOW often
290 exhibits the highest coupling constants, which is indicative of a highly rigid packing of the β-
291 barrel. Strikingly, *Mj*Spt5-KOW has three additional H-bonds between strands β_5 and β_1 (# 22-
292 24), which provides an extra stabilization of the C-terminal β-strand that may contribute to the
293 high thermostability of this protein. The "stable" domains (i.e. *Ec*/*Mt*NusG-KOW and *Mj*Spt5-
294 KOW) show their strongest H-bonds in two regions, namely between strands β_1:β_2 and β_3:β_4. In
295 addition, most of these H-bonds are more stable than corresponding H-bonds in *Ec*/*Vc*RfaH-
296 KOW and hSpt5-KOW5, implying that the H-bonds in the domains with reduced stability are
297 more dynamic and on average longer or involve a less optimal bonding angle. From this we
298 conclude that in *Ec*/*Vc*RfaH-KOW and hSpt5-KOW5 strands β_1 and parts of β_4 are less stably
299 bound to the rest of the β-barrel than in the stable domains. Moreover, together with the fact that
300 β_1, the C-terminal half of β_4, and β_5 are disordered in the all-α state of the *Ec*/*Vc*RfaH-KOW
301 (**Figure 4C**), this also reflects the chameleonic folding behavior of these regions in the all-β
302 state.

303

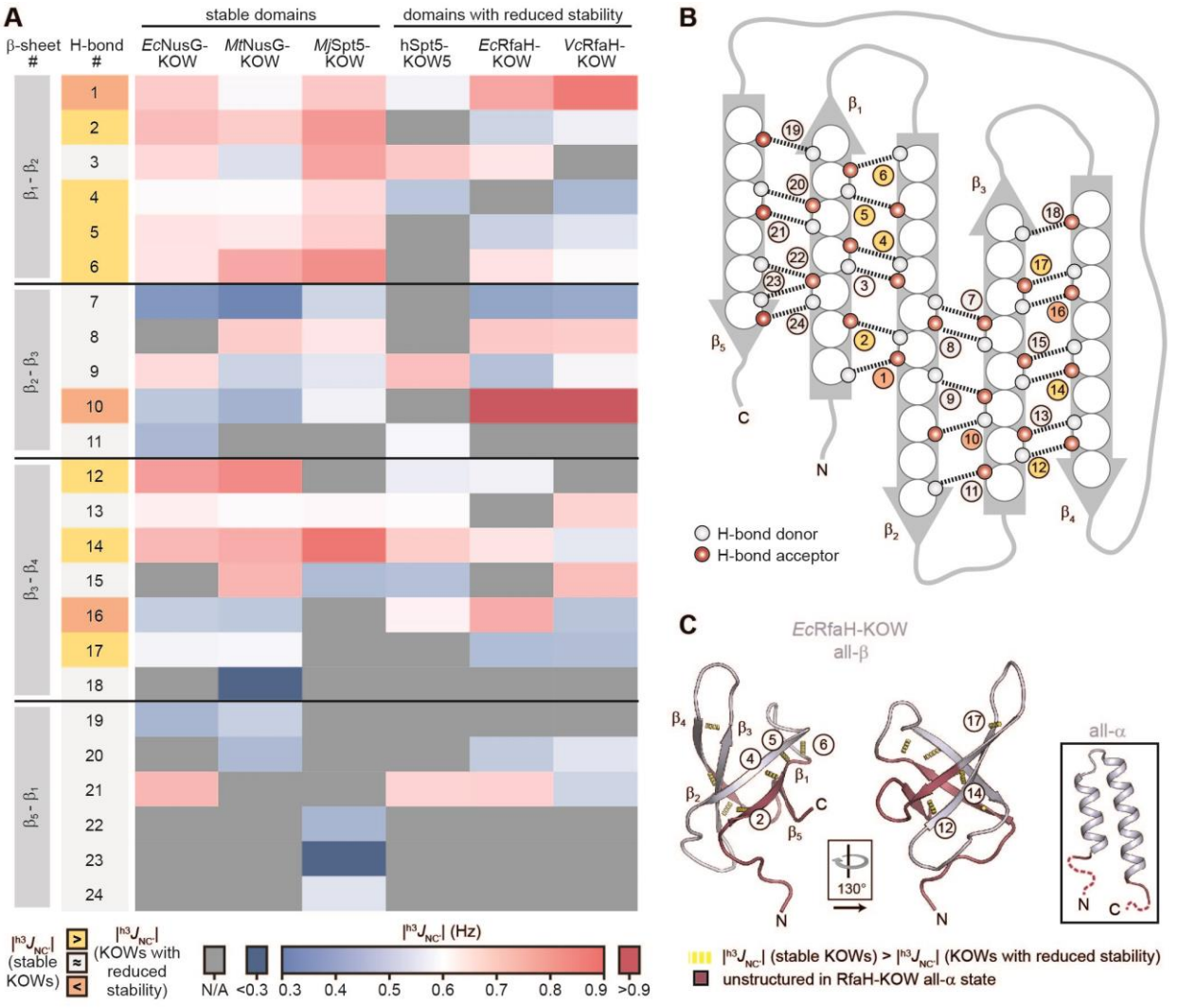

Figure 4. H-bond pattern and stability in the six KOW domains. (**A**) Heat map of the magnitude of the $^{h3}J_{NC'}$ coupling constants of the H-bonds determined by long-range HNCO NMR experiments. H-bonds that are located at equivalent positions are grouped and ordered according to their location in the respective β-sheet (position within the β-barrel as indicated in (B)), and colored according to their $|^{h3}J_{NC'}|$ value as indicated at the bottom. H-bond numbers highlighted in yellow: H-bonds that have lower $|^{h3}J_{NC'}|$ values for at least two of the domains with reduced thermodynamic stability compared to the stable domains; H-bond numbers highlighted in orange: H-bonds that have higher $|^{h3}J_{NC'}|$ values for at least two of the domains with reduced thermodynamic stability compared to the stable domains. (**B**) Scheme of the positions of the H-bonds (dashed lines) within the β-barrel. Amino acids are depicted as spheres. White and red circles represent H-bond donors and acceptors, respectively. H-bonds are color-coded as in (A). (**C**) Cartoon representation of all-β *Ec*RfaH-KOW (PDB-ID: 2LCL, gray). Regions that are unstructured in the all-α conformation are colored in dark red. H-bonds that have lower $|^{h3}J_{NC'}|$ values for at least two of the domains with reduced thermodynamic stability compared to the stable domains are shown as yellow dashed tubes and labeled. The relative orientation of the structures is indicated. The inset shows the all-α *Ec*RfaH-KOW (PDB-ID: 5OND; gray;

unstructured regions at the termini are colored in dark red and correspond to the dark red regions in the all-β *Ec*RfaH-KOW).

Figure supplement 1. Quantification of H-bond strengths for all KOW domains.

hSpt5-KOW5, *Ec*- and *Vc*RfaH-KOW exchange with a globally unfolded conformer on the ms-time scale

To assess the folding mechanism of the KOW domains at the amino acid level, we performed an NMR-based analysis of the structural dynamics of the six β-barrel proteins. As larger structural rearrangements, such as folding events, mostly occur at the µs-ms time scale for small proteins or are even slower (Maxwell et al., 2005), we focused on the analysis of the slow chemical exchange regime. Therefore, we performed amide ^{15}N-based chemical exchange saturation transfer (CEST) experiments (Vallurupalli et al., 2012). This method allows the sensitive detection and characterization of sparsely populated states (= minor species; relative population p_B) that exchange with a major species (relative population $p_A = 1 - p_B$) with a rate k_{ex} of 10 – 200 s^{-1}. The detection is achieved by frequency-selective saturation along the ^{15}N dimension that is "transferred" from the minor to the major species. This decreases the signal intensity of the major species and then leads to an additional dip in the CEST profile (major species signal intensity versus saturation frequency) next to the large major species minimum if there is a difference in the resonance frequencies of the two species.

None of the CEST profiles of *Ec*NusG-KOW, *Mt*NusG-KOW, and *Mj*Spt5-KOW exhibits an exchange peak (**Figure 5A – C**), demonstrating that these domains are stable on the ms time scale, in agreement with their high thermodynamic stabilities (see above).

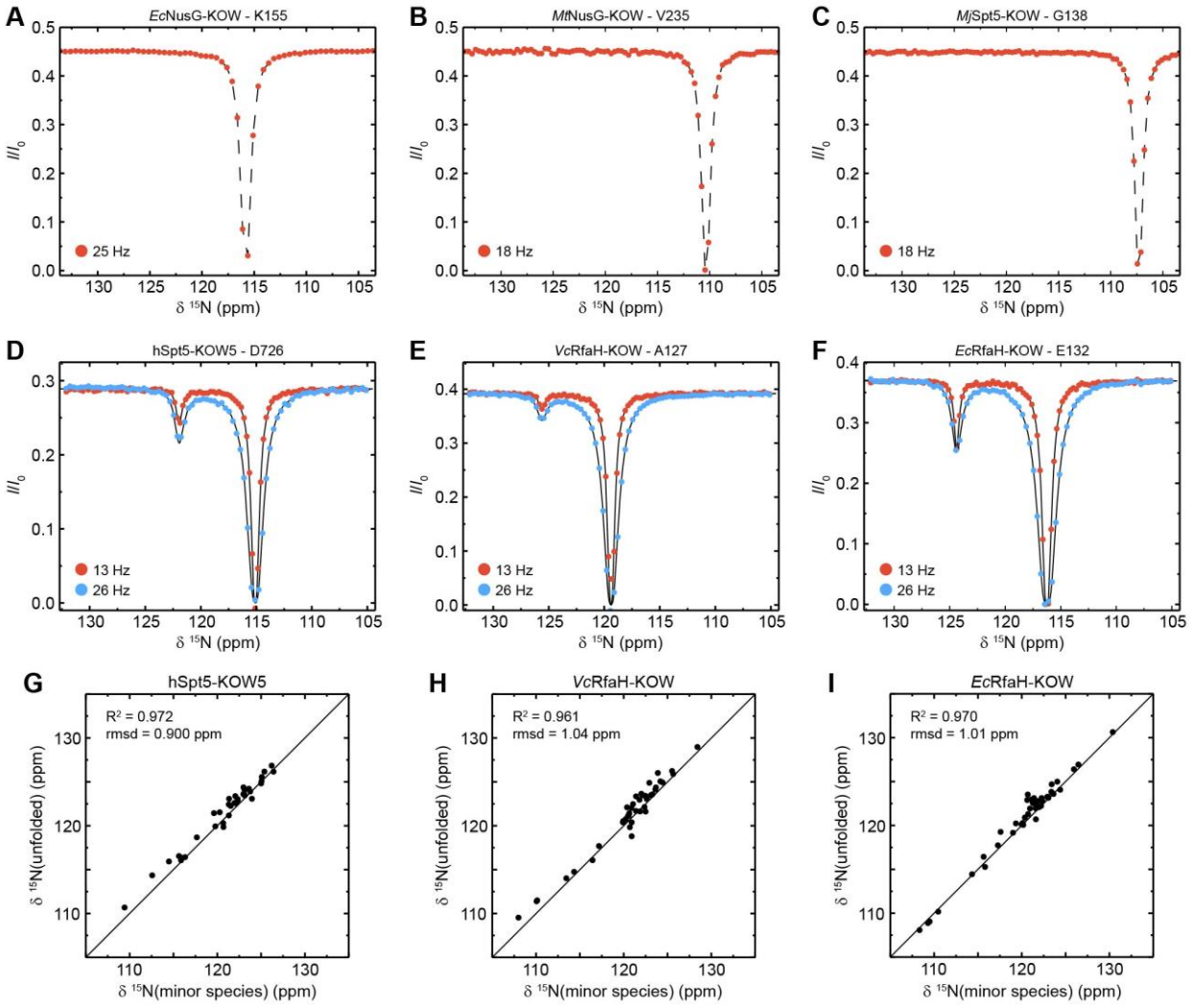

Figure 5. CEST analysis of the KOW domains. (**A**) – (**F**): Representative backbone ^{15}N-CEST profiles of the indicated KOW domain measured with one ((A) – (C)) or two ((D) – (F)) B_1 field strengths and an exchange time of 0.5 s. B_0 field for ((A)-(C)): 21.15 T; B_0 field for ((A)-(C)): 16.45 T. The lines in (D) – (F) are fits to a two-state exchange model. (**G**) – (**I**): Correlation plots showing the high similarity of the chemical shift of the minor CEST species and that of the corresponding random coil value. The latter were obtained by backbone assignment in 8 M urea (*Ec*RfaH-KOW) or are theoretical values (*Vc*RfaH-KOW, hSpt5-KOW5). The squared correlation coefficient and the rmsd between the two corresponding sets of chemical shifts are listed.

Source data 1. CEST fits for *Ec*RfaH-KOW, *Vc*RfaH-KOW and hSpt5-KOW5.

Source data 2. Experimentally determined chemical shift values of urea-denatured *Ec*RfaH-KOW and predicted random coil chemical shift values of *Vc*RfaH-KOW and hSpt5-KOW5.

Figure supplement 1. Extended CEST analysis of hSpt5-KOW5, *Vc*RfaH-KOW, and *Ec*RfaH-KOW.

Figure supplement 2. Exchange parameters derived from CEST experiments.

Figure supplement 3. Secondary structure prediction for the six KOW domains used in this study by Net-CSSP.

In contrast, most CEST traces of hSpt5-KOW5, *Ec*RfaH-KOW, and *Vc*RfaH-KOW have a second dip, indicating exchange with a second, low populated state (exemplary traces are shown in **Figure 5D - F**). Using a two-state exchange model we fitted all CEST traces that showed an exchange signal individually to determine the residue-specific k_{ex} and p_B values. In all three cases, the k_{ex}/p_B values appear to cluster in one region, suggesting a global, cooperative process (**Figure 5 – Figure supplement 1A**). Thus, we next performed a global fit of all CEST traces for each of the three proteins resulting in global rate constants and populations as well as lifetimes of the two states (**Figure 5 – Figure supplement 2**). This analysis yields a relatively high p_B value (5.50 %) but low k_{ex} (15.0 s^{-1}) for *Ec*RfaH-KOW, a much lower p_B value (0.44 %) but higher k_{ex} (75.0 s^{-1}) for *Vc*RfaH-KOW, and p_B/k_{ex} values of 0.85 % and 89.0 s^{-1} for hSpt5-KOW5.

To characterize the exchanging species structurally, we analyzed the chemical shifts of the minor species. In all three cases, the minor species shifts show a very good correlation with those of a completely unfolded conformation (**Figure 5G – I**; R^2 > 96 %, rmsd < 1.04 ppm). Note that the chemical shifts for the unfolded state of *Ec*RfaH-KOW were obtained experimentally by backbone assignment of the protein in 8 M urea, whereas those of *Vc*RfaH-KOW and hSpt5-KOW5 are predicted values (see Materials and Methods for details). Determination of the relative populations finally results in the equilibrium constant and the difference in Gibbs free energy, ΔG, separating the energy levels of the two species (**Figure 5 – Figure supplement 2**). As expected, these ΔG values are similar to those obtained from the urea-based unfolding experiments at pH 7 (**Figure 3 – Figure supplement 1**).

Taken together, the CEST experiments show that the folded all-β state of the isolated RfaH-KOWs and also hSpt5-KOW5 is in equilibrium with a species that resembles the completely unfolded conformation. As this state is easily accessible from the β-barrel, we conclude that the

385 folding barrier separating the two states cannot be too high as this would prohibit an exchange on
386 the ms time scale.

387

388 **The unfolded conformer of *Ec*RfaH-KOW transiently forms helical structures**

389 Although chemical shifts of the minor species of *Ec*RfaH-KOW nicely correlate with the
390 chemical shifts of the urea-unfolded protein (**Figure 5I**), there are some noticeable differences in
391 the ^{15}N chemical shifts ($\Delta\delta$ ^{15}N) of the two data sets (red bars in **Figure 6A, top panel**). In
392 particular, two regions (region 1: Q127 – T131, region 2: E136 – I150) show significant
393 deviations of -1 to -3 ppm, indicating local residual structures in these regions. This finding is
394 supported by the transverse relaxation rates (R_2 values) (**Figure 6A, mid panel**) as R_2 values of
395 regions 1 and 2 in the minor species are higher than corresponding rates in the β-barrel state,
396 suggesting the presence of additional exchange processes on the fast chemical exchange (i.e. μs
397 – ms) time scale. Thus, the minor species itself is an ensemble of fast interconverting structures
398 that differ in their conformations in regions 1 and 2. As the type of present (secondary) structure
399 cannot be derived from ^{15}N data, we recorded a CEST experiment on the ^{13}Cα carbons of ^{13}C-
400 *Ec*RfaH-KOW and calculated $\Delta\delta$ ^{13}Cα between the observed minor species values and the
401 random coil values obtained from the urea-unfolded protein (red bars in **Figure 6A, bottom**
402 **panel**). The deviations are positive in regions 1 and 2, indicating the presence of helical
403 structures at these sites in one of the minor species' fast exchanging sub-states. This is in
404 agreement with secondary structure predictions, which show that the Leu-rich motif (LLLNL) in
405 region 2, where the deviations of δ ^{15}N and δ ^{13}Cα are most pronounced, has high α-helical

propensity (Balasco et al., 2015). Moreover, the two helical elements are located at the positions of the two α-helices in the all-α form of *Ec*RfaH-KOW (compare **Figure 1B**).

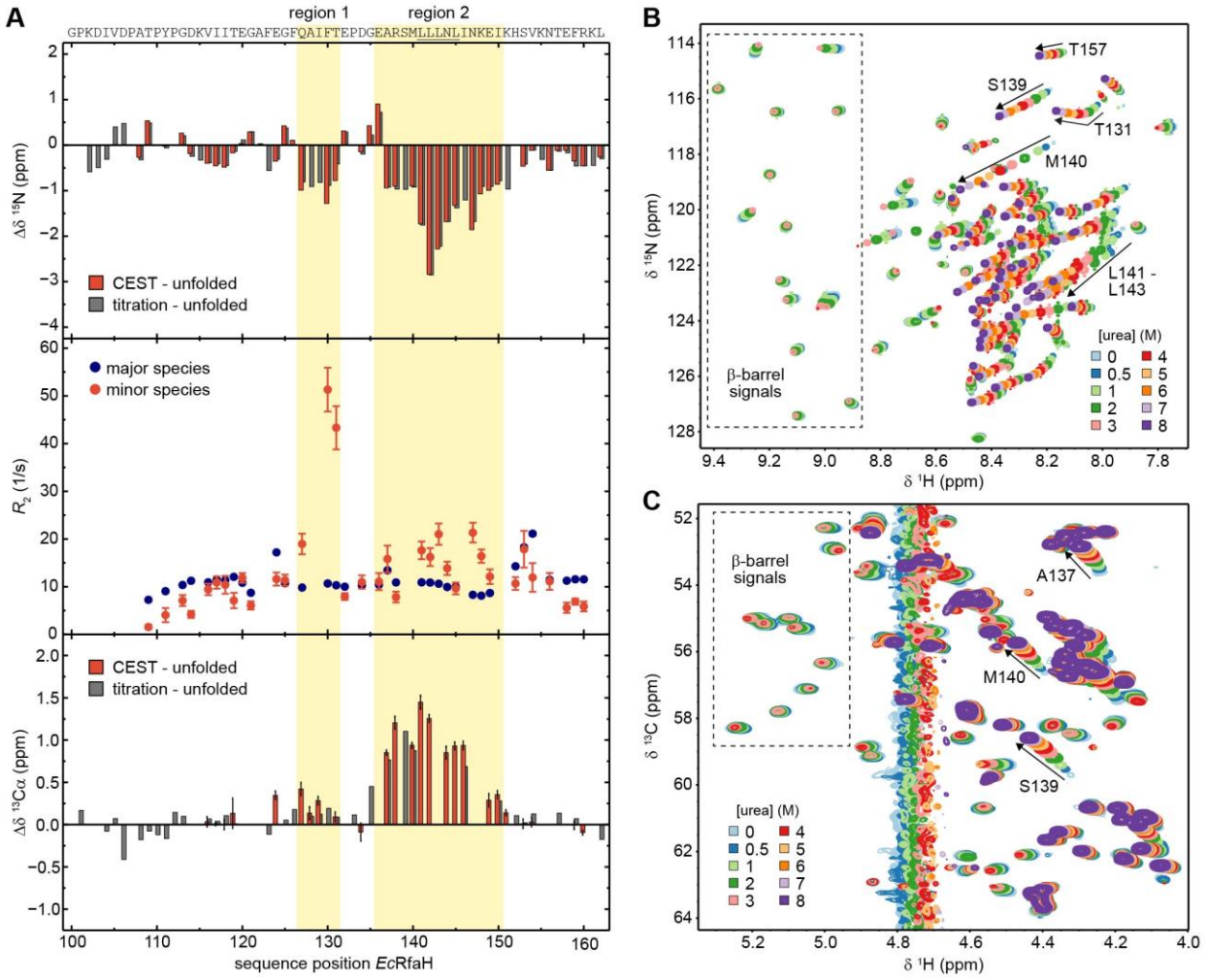

Figure 6. The minor species of *Ec*RfaH-KOW comprises two sub-states, one with residual structure. (**A**) Deviations of the minor species of *Ec*RfaH-KOW from the urea-unfolded state. **Top row:** Sequence-dependent difference between the ^{15}N backbone amide chemical shifts of the minor species and of the value obtained by assignment in 8 M urea. The values for the minor species were either obtained from the CEST experiment (red bars, individual fits), or by tracing back the chemical shift changes from 8 M to 0 M urea in the [^{1}H, ^{15}N]-HSQC-based urea titration (grey bars; see panel (B)). Regions 1 and 2 show deviations of 1-3 ppm whereas the termini have lower deviations with a maximum difference of -0.5 ppm. **Middle row:** R_2 values of the major species (*Ec*RfaH-KOW β-barrel; blue) and minor species (red), obtained from fitting the CEST profiles (global fit). Regions 1 and 2 have R_2 values significantly higher than those of their corresponding β-barrel conformation indicating additional exchange processes, whereas N- and C-terminal regions have R_2 values lower than those of their corresponding β-barrel conformation, which is typical for random coil structures**. Bottom row:** Sequence dependent difference between the ^{13}Cα chemical shifts of the minor species and of the value

obtained by assignment in 8 M urea. The values for the minor species were either obtained from the CEST experiment (red bars, individual fits), or by tracing back the chemical shift changes from 8 M to 0 M urea in the [^{1}H, ^{13}C]-ctHSQC-based urea titration (grey bars; see panel (C)). The sequence of *Ec*RfaH is given above the diagram, the Leu-rich motif is underlined. Regions 1 and 2 are highlighted. (**B, C**) NMR-based chemical equilibrium unfolding experiments of *Ec*RfaH-KOW using urea as denaturant. The plots show an overlay of (B) [^{1}H, ^{15}N]-HSQC, and (C) [^{1}H, ^{13}C]-ctHSQC spectra of [^{15}N, ^{13}C]-*Ec*RfaH-KOW, acquired in the presence of varying urea concentrations. The system was buffered by 20 mM Na-phosphate (pH 6.5), 100 mM NaCl, 1 mM EDTA, 10 % (v/v) D_2O. Arrows and labels indicate signals of residues that exhibit strong chemical shift changes in the indirect dimension (^{15}N in (B), ^{13}C in (C)). The spectra are colored as indicated.

Source data 1. ANS binding by *Ec*RfaH-KOW during urea-based denaturation.

Figure supplement 1. The intermediate state of *Ec*RfaH-KOW is no equilibrium MG.

Figure supplement 2. Extended analysis of the urea-induced denaturation of *Ec*RfaH-KOW with a three-state model.

Like *Ec*RfaH-KOW, the minor species of *Vc*RfaH-KOW also seems to contain residual structure (**Figure 5 – Figure supplement 1B**). As the unfolded state of this domain was not assigned experimentally, predicted chemical shift values for the random coil structure were used for the correlation plot (**Figure 5H**). However, when plotting the $\Delta\delta$ ^{15}N values versus the sequence position (**Figure 5 – Figure supplement 1B**), the resulting pattern resembles the one obtained for *Ec*RfaH-KOW (compare **Figure 6A, top panel**). The regions around residues 103 - 125 (linker) and 155 - 165 (C-terminus) show relatively low values ($\Delta\delta$ ^{15}N $\approx$ -1.5 ppm), indicating a random coil structure, whereas the region around residues 140 - 150 exhibits $\Delta\delta$ ^{15}N values of > 2 ppm, suggesting residual structure. Based on this similarity to *Ec*RfaH-KOW we propose that the *Vc*RfaH-KOW minor species also contains residual α-helical structures, although the population of this species is much lower than that in the case of *Ec*RfaH-KOW (0.4 % vs. 5.5 %). This results in rather small minor species dips in the CEST profiles so that fitting of R_2 rates of the minor species was not possible with high precision (data not shown) and no

conclusion could be drawn regarding the presence of potential subspecies within the minor species.

The hSpt5-KOW5 domain is part of an "RNA clamp" during transcription elongation in eukaryotes (Bernecky et al., 2017) and exhibits the typical β-barrel fold in all available structures. Strikingly, hSpt5-KOW5 also exchanges with an unfolded species under non-denaturing conditions (**Figure 5 – Figure supplement 1C and Figure 5G**), just as *Ec*RfaH-KOW and *Vc*RfaH-KOW. However, in contrast to all other KOW domains in this study, hSpt5-KOW5 is not located at the very C-terminus of full-length hSpt5, but it is just one out of seven KOW domains being flanked by several hundreds of residues at either terminus. Thus, the stability of this domain may be different in its physiological environment. In line with this, the difference between the minor species chemical shifts and the predicted random coil values (**Figure 5 – Figure supplement 1C**) never exceeds ±2 ppm and the R_2 values of the minor species are lower than those of the β-barrel (data not shown), indicating that the minor species does not contain substantial residual structure. Finally, secondary structure predictions suggest that all NusG/Spt5-KOW domains adopt 4-5 β-strands (**Figure 5 – Figure supplement 3**). In contrast, the RfaH-KOWs exhibit propensity for both β-strands and α-helices, especially the regions with residual structure in the CEST minor species, in agreement with their chameleonic behavior. Taken together, this data suggests that hSpt5-KOW5 is a typical monomorphic β-barrel and that its decreased stability, accompanied by the existence of a minor, unfolded species, may be attributed to the absence of the neighboring domains, although we cannot completely rule out that these features are real, intrinsic properties of hSpt5-KOW5 in the full-length protein with (yet unknown) functional relevance.

As the completely unfolded state was only experimentally assigned for *Ec*RfaH-KOW we will focus on this domain in the following analysis. Owing to its population of 5.5 % (**Figure 5 – Figure supplement 2**), *Ec*RfaH-KOW's minor species should be detectable in a standard HSQC spectrum, given a sufficiently high signal-to-noise ratio. We therefore aimed at analyzing the role of the minor species during the chemical denaturation of *Ec*RfaH-KOW by recording [^{1}H, ^{15}N]- and [^{1}H, ^{13}C]-correlation spectra of [^{15}N, ^{13}C]-labeled *Ec*RfaH-KOW in the presence of various urea concentrations (0 – 8 M) (**Figure 6B,C**). In both spectra series, we observed a decrease in peak intensity/volume of the β-barrel signals with increasing urea concentration (boxed regions in **Figure 6B,C**), which is completed at ≈ 4 M urea, indicating that the first transition in the far-UV-based chemical denaturation of *Ec*RfaH-KOW (**Figure 3F**) corresponds to the unfolding of its β-barrel (tertiary) structure. This is also corroborated by near-UV CD spectroscopy-based chemical denaturation experiments using urea or GdmCl, respectively, (**Figure 6 – Figure supplement 1A, B**), which clearly show that the transition during the titration from 0 to 3 M urea/1 M GdmCl is accompanied by a loss in tertiary structure. The possibility that the resulting conformation corresponds an equilibrium molten globule is, however, excluded due to its inability to bind 8-anilino-1-naphthalenesulfonic acid (ANS, **Figure 6 – Figure supplement 1C**).

In order to identify signals corresponding to the minor species in the [^{1}H, ^{15}N]- and [^{1}H, ^{13}C]-correlation spectra of *Ec*RfaH-KOW we started with the spectra of the urea-unfolded protein (8 M urea). We observed that most of the corresponding signals shifted linearly with decreasing urea concentration and also lost intensity when entering the transition region (< 3 M urea). At 0 M urea, finally, only a set of weak signals remained, which we identified as signals of the minor species based on their chemical shifts (compare red and grey bars in **Figure 6A,**

498 **top/bottom panels**). The linear transition between the positions of the (urea) unfolded state
499 towards the positions of the minor species signals suggests that the minor species can be
500 described as an ensemble of exchanging sub-states, some corresponding to the completely
501 unfolded state and some exhibiting residual helical structure.

502 The urea-induced chemical shift perturbations experienced by the minor species signals in the
503 [^{1}H, ^{15}N]-HSQCs are then likely explained by a combination of two effects: (i) change of the
504 chemical environment due to the presence of urea, which particularly affects δ ^{1}H (see e.g. signal
505 of L162 in **Figure 6B**) and (ii) change in the relative populations of the minor species' sub-states
506 towards the unfolded state, which mainly affects $\Delta\delta$ ^{15}N. Since the Hα/Cα chemical shifts are
507 relatively independent of the solvent conditions, their perturbations in the urea denaturation
508 series (**Figure 6C**) even better reflect the change in the ratio of the minor species' sub-states.
509 Thus, we conclude that some of the exchanging states of the minor species correspond to a
510 completely unfolded state, whereas the other sub-species contain (α-) helical structures in
511 regions 1 and 2, hereby referred to as α-helical unfolding intermediate Uα. The shifting of the
512 minor species' peaks in **Figure 6C** is completed at ≈7 M urea, implying that the second transition
513 in the CD-based unfolding experiment (**Figure 4F**) corresponds to the denaturation of Uα.
514 Interestingly, the R_2 values of residues in region 1 are more than twice as high as those of
515 residues in region 2 and, in the [^{1}H, ^{15}N]-HSQC-based denaturation experiment (**Figure 6B**), the
516 minor species' signals of residues in region 1 do not shift in a linear manner as it is typical for
517 two exchanging states. Instead they show a curved transition that is "kinked" at ≈ 2 M urea (see
518 e.g. T131), implying fast chemical exchange between at least three states. Although our
519 experiments do not allow a precise structural characterization of all states of the minor species, it
520 may be described as a structural ensemble of a completely unfolded state and a species that

contains α-helical elements in regions 1 and 2 (i.e. Uα), with region 1 exhibiting some structural heterogeneity.

Due to the fast chemical exchange between the two exchanging subspecies of *Ec*RfaH-KOW's U and Uα states, their relative population in a certain titration step is encoded in the chemical shift of the minor species signal, whereas the volume of the minor species peak is proportional to the sum of the populations of both states (assuming similar transverse relaxation rates for the species). To first quantify the decay of the all-β conformation and the increase of the minor species during the urea denaturation we analyzed the intensity and peak position of both species exemplarily for residue S139 in the [^{1}H, ^{13}C]-ctHSQC-based titration (**Figure 6C and Figure 6 – Figure supplement 2A**). The resulting ΔG value of ≈ 7 kJ/mol between the energy levels of major and minor species agrees well with the results from the CEST (7 kJ/mol). Additionally, the *m* value of 3.4 kJ/(mol M) is very similar to the *m* values obtained for the other KOW domains (**Figure 3 – Figure supplement 1**), indicating that the minor species is indeed close to a completely unfolded state with a small buried surface area and that the stability of the minor species' Uα state is low.

The complete denaturation of the minor species, i. e. the transition of Uα to a fully unfolded state, can be followed in the [^{1}H, ^{13}C]-ctHSQC-based denaturation experiment by analyzing the change of the minor state's chemical shift from the position of the more α-helical conformation towards that of the completely unfolded state. For example, the Hα/Cα correlation peaks of residues A137, S139, or M140 clearly shift from regions typical for α-helical structures (upfield ^{1}H, downfield ^{13}C) to positions corresponding to an unstructured conformation (downfield ^{1}H, upfield ^{13}C), and finally they localize next to the signals of the Ala, Ser or Met residues that do

not reside in regions with residual helical structure (**Figure 6C**). The chemical shifts of Cα/Hα groups depend to a much lower extent on the urea concentration in the sample than the chemical shifts of amide groups and therefore they provide better measures for the exchange between U and Uα. Plotting the changes of the chemical shifts of the Cα/Hα groups of residues A137, S139 and M140 versus the urea concentration (**Figure 6 – Figure supplement 2B**) results in curves that resemble the second half of an unfolding transition (Uα ⇌ U) and approach the baseline of the unfolded state at ≈ 6 M urea. The absence of a baseline for Uα precludes a quantitative analysis, but it shows that the transition mid-point of the curve is probably close to or below 0 M urea, implying that Uα is unstable (i.e. higher in energy) relative to the fully unfolded state, and that Uα buries a small amount of surface area (**Figure 3 – Figure supplement 1**).

Discussion

Fold-switching is conserved among RfaH proteins

Genes coding for RfaH orthologs can be found in many bacterial pathogens, including *Salmonella*, *Klebsiella*, *Vibrio*, and *Yersinia* spp (Carter et al., 2004). Despite their divergent evolution, RfaH proteins seem to have a conserved mechanism of action (Carter et al., 2004). To date only *Ec*RfaH was structurally characterized, revealing that this protein has unique structural features classifying it as transformer protein (Belogurov et al., 2007; Burmann et al., 2012; Zuber et al., 2019). Here, we show that *Vc*RfaH, an evolutionary quite divergent representative sharing 35.8 % sequence identity with *Ec*RfaH, exhibits very similar structural properties, i.e. *Vc*RfaH-KOW, like *Ec*RfaH-KOW, folds as α-hairpin in the full-length protein, but adopts a NusG-type β-barrel conformation in its isolated form (**Figure 1**). Interestingly, in *Vc*RfaH helix α_3* is 1.5 turns longer as compared to *Ec*RfaH and *Vc*RfaH has a disulfide bridge connecting strand β_3* and helix α_3*, stabilizing this helix. These two features imply a stabilization of the domain interface and thus an increased affinity between the domains as compared to *Ec*RfaH. This might also explain the increased stability of the isolated *Vc*RfaH-KOW domain (≈ 14 kJ/mol), which compensates the higher energy gain of the domain interaction. Further, the increased stability of the *Vc*RfaH-KOW domain may be the cause for the sigmoid-shaped CD-based chemical denaturation curves, in agreement with a two-state unfolding process: global unfolding of the folded state occurs at higher denaturant concentrations, where potential partly structured folding intermediates are already largely destabilized and therefore escape detection. This conclusion is supported by the Trp fluorescence-based denaturation data (**Figure 3 – Figure supplement 2**), suggesting that the change in the CD signal is almost exclusively caused by the decay of the β-barrel conformation and that the putative contribution of the intermediate state to the change of

576 the CD-signal is negligible. Nevertheless, we conclude that *Vc*RfaH may be regulated by fold-
577 switching just like *Ec*RfaH, and that this metamorphic behavior is conserved in the class of RfaH
578 proteins and may even be found in other NusG paralogs.

579

580 **Model for the structural plasticity of RfaH**

581 *Ec*RfaH switches the conformation and function of its KOW domain in a reversible manner to
582 achieve a tight control of gene expression (Zuber et al., 2019). In free *Ec*RfaH, the α-helical
583 hairpin conformation is the preferred state of *Ec*RfaH-KOW, whereas domain separation or
584 isolation of *Ec*RfaH-KOW foster population of the all-β state in solution (Burmann et al., 2012),
585 suggesting that the all-α conformation is intrinsically unstable, but becomes the thermodynamic
586 minimum in free *Ec*RfaH due to interaction with *Ec*RfaH-NGN.

587 Interestingly, our thermodynamic analysis (**Figures 2 and 3**) of the isolated *Ec*RfaH-KOW
588 domain reveals that, although the all-β conformation is the preferred state in isolation, it is only
589 marginally stable, and it is in rapid equilibrium with an "unfolded" state, which is populated to a
590 significant extent, even under physiological conditions. The "unfolded" state is a mixture of
591 random-coil-type unfolded species and a species containing two helical regions (Uα).

592 Based on our results, we suggest a model for the structural transitions of *Ec*RfaH-KOW (**Figure**
593 **7**).

594

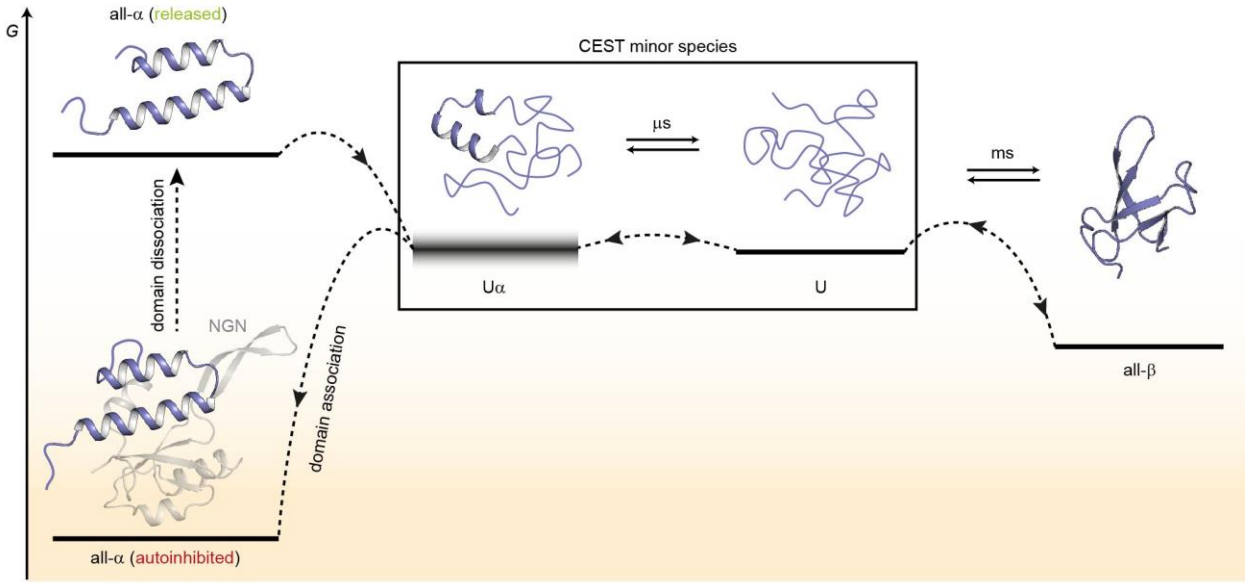

Figure 7. Model for the conformational plasticity of *Ec*RfaH-KOW. Qualitative Gibbs free energy level diagram and associated structures for the all-α to all-β transition of *Ec*RfaH-KOW and *vice versa*. In its ground state, i.e. the autoinhibited conformation, the energy of the all-α conformation of *Ec*RfaH-KOW is strongly lowered by the extensive inter-domain contacts with the *Ec*RfaH-NGN domain. Upon recruitment, the domains dissociate, the helical structure of the released KOW domain becomes destabilized in isolation, and rapidly decays towards an ensemble of mainly unfolded sub-states that interconvert on the μs time scale. Some of the sub-states correspond to the completely unfolded state (U) whereas others retain some residual (α-) helical elements (Uα). The scheme displays exemplary structures of these sub-states. Due to their fast structural interconversion, U and Uα may be grouped into a single macro-state/ensemble (as is the case during the CEST experiments) that exhibits helical structures for a limited amount of time and is otherwise unfolded. Uα is either marginally stable or even unstable (therefore, its energy level is blurred). The disordered conformation then allows for easy and rapid refolding to the all-β conformation. Due to their low thermodynamic stability, or even instability of all-β and Uα, respectively, the last two steps are reversible, that is the all-α state can be rapidly regained when the *Ec*RfaH-NGN domain becomes available for re-association after transcription termination.

In the autoinhibited state the all-α conformation of *Ec*RfaH-KOW corresponds to the minimum of the Gibbs free energy as it is stabilized by contacts to the *Ec*RfaH-NGN. During recruitment of *Ec*RfaH to an *ops*-paused elongation complex, the *Ec*RfaH-NGN:KOW interface is destabilized (most probably *via* an encounter complex), the domains dissociate and *Ec*RfaH-NGN is sequestered to RNAP (Zuber et al., 2019). The freed all-α *Ec*RfaH-KOW is not stable as

619 *G* increases due to the loss of *Ec*RfaH-NGN contacts. Consequently, *Ec*RfaH-KOW unfolds,
620 resulting in an ensemble of rapidly interconverting sub-states. Some of these sub-states still
621 contain two residual α-helical regions (intermediate Uα) that correspond to the tip of the α-
622 hairpin in the all-α state, in agreement with hydrogen/deuterium exchange data, which indicate
623 that the hairpin-tip is the most stable part of the all-α conformation (Galaz-Davison et al., 2020).
624 Other sub-states represent the completely unfolded protein, which then rapidly refolds into the
625 all-β form. Upon transcription termination *Ec*RfaH is released, and the process is reversed with
626 unfolding of the β-barrel starting, most probably, by detaching β_1 and β_4/β_5 from the central
627 strands as the corresponding H-bonds are the least stable ones (**Figure 4**). The U state is in
628 equilibrium with Uα, where two α-helical regions that will later constitute the α-hairpin tip are
629 formed transiently and may thus serve both as the nucleation point for the completion of the all-
630 α structure and as starting point for recognition of its cognate binding site on the NGN. This
631 mechanism ensures rapid re-autoinhibition and prevents aggregation of *Ec*RfaH. Although we
632 did not analyze *Vc*RfaH as extensively as *Ec*RfaH, our results suggest that the *Vc*RfaH-KOW
633 domain most likely employs a similar mechanism for its structural transformation, indicating that
634 the presented model is a general scheme for RfaH proteins.

635 In support of our model, all computational studies on *Ec*RfaH found that the all-α conformation
636 is stable only when in contact with the NGN. Modification of the strength of the *Ec*RfaH-
637 NGN:KOW interface (Ramírez-Sarmiento et al., 2015) or deletion of the linker (Xun et al.,
638 2016) destabilize the all-α fold and ultimately drive *Ec*RfaH-KOW into the β-barrel state.
639 Moreover, the β-barrel fold is stable and corresponds to or is close to the energy minimum of the
640 energy landscape of *Ec*RfaH-KOW, whereas the all-α fold rapidly unfolds and has a higher *G*-
641 value than the all-β state (Balasco et al., 2015; Bernhardt and Hansmann, 2018; Gc et al., 2014;

642 Joseph et al., 2019; Li et al., 2014; Xiong and Liu, 2015). Apart from these general concepts,
643 most studies differ in several key points, such as the extent to which the all-α state is populated
644 in the isolated *Ec*RfaH-KOW, or the precise folding pathway from all-α to all-β. Strikingly, a
645 recent bioinformatical study very nicely mirrors our data as the authors also observed a
646 significant portion of transiently formed helical structure within the unfolded state ensemble in
647 their simulations (Seifi and Wallin, 2021).

648

649 **Requirements for fold-switching proteins**

650 Previous work on designed and naturally occurring fold-switching proteins has identified several
651 specific properties that make fold-switching proteins distinct from others (Bryan and Orban,
652 2010; Porter and Looger, 2018). In this study, we show that RfaH also meets all these
653 requirements:

654 (i) Reduced thermodynamic stability (Bryan and Orban, 2010). A diminished stability is both the
655 result of and key to the function of fold-switching proteins. As the fold-switching sequence must
656 be compatible with both adopted topologies, it can only be optimized to a certain extent to
657 stabilize one specific fold, ensuring that both conformations can be interconverted and that the
658 structure is not "trapped" in one state. This is reflected by a dual-funneled energy landscape with
659 two main minima, which are, however, not as deep as the global minimum of a stable protein.
660 Our comprehensive thermodynamic analysis (**Figures 2 and 3**) reveals that the all-β fold of both
661 RfaH-KOWs is indeed less stable than the bacterial and archaeal NusG/Spt5-KOW domains. As
662 general transcription factors, NusG/Spt5 proteins do not require an as-sophisticated regulation as
663 RfaH (Artsimovitch and Knauer, 2019) (for hSpt5-KOW5 see below) and thus benefit from a
664 stable structure to carry out their function.

(ii) Generation of new binding surfaces (Bryan and Orban, 2010). The regulation of conformational transitions in fold-switching proteins is achieved by energetically stabilizing one of the two conformations in response to a molecular trigger, resulting in a far more dynamic energy landscape than that of well-folded proteins as the energy level of a particular conformation strongly depends on the environment. This context-dependent stabilization of one state is possible because the two different folds exhibit different surface topologies, each allowing distinct interactions. The ability to selectively hide/expose "latent" binding sites within different folds is also the most important function of fold-switching in general, as it enables a level of control that cannot be achieved by other mechanisms. In RfaH, for instance, autoinhibition is coupled to a conformational switch, preventing off-target recruitment and interference with NusG (Belogurov et al., 2009).

(iii) Unfolded regions in one of the two states (Bryan and Orban, 2010). In RfaH, the all-α KOW domain contains unstructured N- and C-termini, whereas the corresponding regions form β-strands β_1 and β_4/β_5 in the all-β conformation (**Figure 1B and Figure 4C**). These disordered parts provide an entropic stabilization of the respective state as they do not adopt a defined structure. A bioinformatic study indicated that these regions of the CTD additionally stabilize the NGN:KOW interface by forming transient, IDP-like interactions (Xun et al., 2016). We show that the structural interconversion between the two RfaH states proceeds *via* a chiefly unfolded intermediate and we propose that the disordered segments may help to facilitate and/or initiate this transition, similar to the mechanism suggested for the human chemokine XCL1 (lymphotactin) (Tyler et al., 2011). Finally, disordered regions in one state have the advantage that they can be evolutionary optimized to selectively stabilize one of the two states of a fold-

687 switch pair, whereas there is no need to fit a defined three-dimensional structure in the other
688 state.

689 (iv) Divergence in predicted and observed secondary structure (Porter and Looger, 2018).
690 Secondary structure predictions show that both *Vc*RfaH-KOW and *Ec*RfaH-KOW contain
691 stretches with high propensity for both β-strands and α-helical structures (**Figure 5 – Figure**
692 **supplement 3**), in agreement with other bioinformatical analyses (Balasco et al., 2015).
693 Interestingly, this tendency is also visible in the isolated KOW domain as the disordered regions
694 in the all-α fold correspond to the β-strands that are less stable in the RfaH-KOWs as compared
695 to NusG-KOWs, whereas the helical propensity is reflected in the structure of Uα.

696 (v) Cooperatively folding units (Porter and Looger, 2018). The folding cooperativity of *Ec*RfaH-
697 KOW depends on the presence of the *Ec*RfaH-NGN, i.e. in the absence of *Ec*RfaH-NGN
698 *Ec*RfaH-KOW folds cooperatively on its own. However, the cooperativity is generally rather low
699 and the activation barrier separating the "unfolded" and the folded states is small, allowing fast
700 transitions.

701

702 Fold-switching is a highly efficient principle of regulation with a steadily increasing importance.
703 To date about six fold-switching proteins have been studied in detail (summarized in refs.
704 (Dishman and Volkman, 2018; Lella and Mahalakshmi, 2017; Zamora-Carreras et al., 2020)),
705 but estimates suggest that up to 4 % of the proteins in the PDB may have the ability to switch
706 folds (Porter and Looger, 2018). Our study demonstrates which molecular mechanisms confer
707 RfaH its structural plasticity that allows operon-specific regulation without competing with its
708 monomorphic paralog NusG/Spt5. In line with our findings, a recent study on XCL1, another

model system for fold-switching proteins, identified very similar principles for the evolution and design of fold-switching proteins (Dishman et al., 2021).

Importance of a chiefly unfolded state in protein fold-switching

In summary, our results highlight two key features in protein fold-switching: decreased thermodynamic stability and defined local structures in "unfolded" intermediates. Diminished stability is often thought to be detrimental for proteins as it favors non-native contacts and promotes aggregation. However, it is essential to confer fold-switching proteins their conformational plasticity, and, as all transitions from and to the unfolded states are very fast, and the population of these states is rather low, fold-switchers can evade aggregation. Further, the capability of the "unfolded" state to harbor residual defined structures, e.g. α-helices, allows to pre-encode a second conformation that could be readily adopted upon a molecular signal.

721 ## Materials and Methods

722

723 ### Cloning

724 The *Vc*RfaH expression vector pVS13 (*V. cholerae rfaH* from pHC301 (Carter et al., 2004) in
725 plasmid pTYB1 (NEB)) was a gift from I. Artsimovitch, The Ohio State University, Columbus,
726 OH. The C-terminal *Vc*RfaH residue, Thr165, is substituted by an Ala to ensure efficient
727 cleavage of the resulting chitin binding domain (CBD) intein fusion protein (see below).
728 Expression plasmids for *Vc*RfaH-KOW (residues E103-T165), hSpt5-KOW5 (residues G699-
729 G754), and *Mj*Spt5-KOW (residues K83-D147) were created by cloning of the corresponding
730 gene regions into vector pETGb1a (G. Stier, EMBL, Heidelberg, Germany) *via Nco*I and *BamH*I
731 (*Vc*RfaH-KOW), or *Nco*I and *EcoR*I (hSpt5-KOW5 and *Mj*Spt5-KOW) restriction sites,
732 respectively. Templates for PCR amplification were plasmids pHC301 (Carter et al., 2004) for
733 *Vc*RfaH-KOW, pOTB7_huSUPT5H (Zuber et al., 2018) for hSpt5-KOW5, and pGEX-
734 2TK_*Mj*Spt5-KOW ((Hirtreiter et al., 2010); kindly provided by F. Werner, University College
735 London, UK) for *Mj*Spt5-KOW. The primers used for cloning are listed in **Table 1**. All plasmids
736 used in this study are listed in **Table 2**.

737 **Table 1.** Primers used for cloning.

Primer	Sequence (5' → 3')
Fw-*Vc*RfaH-KOW	CAT GCC ATG GGA GAG CAA TTG AAG CAT GCC AC
Rv-*Vc*RfaH-KOW	CGC GGA TCC TTA GGT GAC TTC CCA ATC GG
Fw-hSpt5-KOW5	CAT GCC ATG GGC CGG AGG GAC AAC GAA CTC ATC GG
Rv-hSpt5-KOW5	TAG AAT TCT CAG CCC ACC GTG GTG AGC CGC TG
Fw-*Mj*Spt5-KOW	AT GCC ATG GGT AAG AAA ATC ATT GAA AAT ATT GAG AAA GG
Rv-*Mj*Spt5-KOW	CGG AAT TCT TAA TCT TTA TGC TTT GAA ACT ATT TTA AC

738
739
740

741 **Table 2.** Plasmids.

Plasmid	description	Source
pVS13	*rfaH* from *V. cholera* in pTYB1	I. Artsimovitch
pHC301	*rfaH* from *V. cholera* in pIA238 (a pET28 derivative) (Artsimovitch and Landick, 2002)	(Carter et al., 2004)
pETGb1a-*Vc*RfaH-KOW	$rfaH^{103-165}$ from *V. cholera* in pETGb1a	This work
pETGb1a-hSpt5-KOW5	human $spt5^{699-754}$ in pETGb1a	This work
pETGb1a-*Mj*Spt5-KOW	$spt5^{583-147}$ from *M. janaschii* in pETGb1a	This work
pOTB7_huSUPT5H	cDNA plasmid containing human *spt5*	(Zuber et al., 2018)
pGEX-2TK_*Mj*Spt5-KOW	$spt5^{583-147}$ from *M. janaschii* in pGEX-2TK	(Hirtreiter et al., 2010)
pETGb1a-*Ec*NusG-KOW	$nusG^{123-181}$ from *E. coli* in pETGb1a	(Burmann et al., 2010)
pET101d-*Mt*NusG-KOW	$nusG^{178-238}$ from *M. tuberculosis* in pET101d	(Strauß et al., 2016)
pETGb1a-*Ec*RfaH-KOW	$rfaH^{101-162}$ from *E. coli* in pETGb1a	(Burmann et al., 2012)

742

743 **Production of recombinant proteins**

744 *Vc*RfaH was obtained from a CBD intein fusion protein encoded in plasmid pVS13, with
745 expression conditions and purification strategy as described for *E. coli* RfaH (Vassylyeva et al.,
746 2006). *Ec*NusG-KOW and *Mt*NusG-KOW were produced as previously described (Burmann et
747 al., 2010; Strauß et al., 2016). *Mj*Spt5-KOW, hSpt5-KOW5, *Ec*RfaH-KOW, and *Vc*RfaH-KOW
748 were obtained from Gb1 fusions with expression and purification conditions similar to that of
749 *Ec*RfaH-KOW (Burmann et al., 2012).

750 The quality of all recombinantly produced proteins was ensured according to the guidelines
751 established by ARBRE-MOBIEU and P4EU (https://arbre-mobieu.eu/guidelines-on-protein-
752 quality-control/) (de Marco et al., 2021). In brief, purity was checked by sodium dodecyl sulfate
753 polyacrylamide gel electrophoresis, the absence of nucleic acids by UV spectroscopy, the
754 identity by mass spectrometry and/or NMR spectroscopy, the folding state by CD and/or NMR
755 spectroscopy, and the absence of aggregation by analytical gel filtration or dynamic light
756 scattering.

Isotopic labeling of proteins

For the production of ^{15}N- and ^{15}N, ^{13}C-labelled proteins, *E. coli* cells were grown in M9 medium (Green et al., 2012; Meyer and Schlegel, 1983) containing $(^{15}NH_4)_2SO_4$ (Sigma/Merck KGaA, Darmstadt, Germany) or $(^{15}NH_4)_2SO_4$ and ^{13}C-D-glucose (Euriso-Top GmbH, Saarbrücken, Germany), respectively, as sole nitrogen or carbon sources. Deuteration was achieved by accustoming cells to M9 medium prepared with increasing concentrations of D_2O (0 %, 50 %, 100 % (v/v); Euriso-Top GmbH, Saarbrücken, Germany). Expression and purification protocols were identical to those of the unlabeled proteins.

NMR spectroscopy

NMR experiments were conducted at Bruker Avance 600, Avance 700, Ascend Aeon 900, and Ascend Aeon 1000 spectrometers, each equipped with room temperature (Avance 600) or cryogenically cooled, inverse ^{1}H, ^{13}C, ^{15}N triple resonance probes (all other spectrometers). All measurements were conducted in 5 mm tubes with a sample volume of 550 µl at 25 °C, if not stated otherwise. NMR data was processed using in-house software and analyzed using NMRViewJ (OneMoon Scientific).

Backbone resonance assignments for *Vc*RfaH, *Vc*RfaH-KOW, hSpt5-KOW5, *Mj*Spt5-KOW, and urea-unfolded *Ec*RfaH-KOW were obtained using standard band-selective excitation short transient (BEST) (Lescop et al., 2007; Schanda et al., 2006) Transverse Relaxation Optimized Spectroscopy (TROSY)-based triple resonance experiments (Pervushin et al., 1997; Salzmann et al., 1998). Additionally, carbon-detected CACO, CAN, and NCO experiments (Bermel et al., 2005) were recorded for *Vc*RfaH-KOW. Side chain assignments for *Vc*RfaH-KOW were obtained from CCH- and H(C)CH-TOCSY, HBHA(CO)NH, C(CO)NH, aromatic [^{1}H, ^{13}C]-

780 HSQC and ^{13}C-edited aromatic Nuclear Overhauser Enhancement Spectroscopy (NOESY)
781 experiments (Sattler et al., 1999). Three-dimensional assignment and NOESY experiments were
782 acquired using a Non-Uniform Sampling scheme with a sparsity of 25 - 50 %. Spectra were
783 subsequently reconstructed with in-house written software using the iterative soft thresholding
784 algorithm (Hyberts et al., 2012). The *Ec*RfaH-KOW, *Vc*RfaH-KOW, hSpt5-KOW5 and *Mj*Spt5-
785 KOW samples contained 0.5 – 1 mM [^{15}N, ^{13}C]-labeled protein in 20 mM Na-phosphate
786 (pH 6.5), 100 mM NaCl, 1 mM Ethylenediaminetetraacetic acid (EDTA), 10 % (v/v) D_2O. The
787 *Ec*RfaH-KOW sample further contained 6 M urea. Due to limited sample stability and poor
788 quality of the initial spectra, *Vc*RfaH (0.3 mM) was [^{2}H, ^{15}N, ^{13}C]-labeled and in an optimized
789 buffer (25 mM Bis-Tris-Propane (pH 6.5), 25 mM Na-Tartrate, 50 mM NaCl, 10 % (v/v) D_2O)
790 and the measurements were conducted at 20 °C. The Cα and CO secondary chemical shift for
791 *Vc*RfaH was calculated as difference between the observed chemical shift and the predicted
792 random coil value (Wishart and Sykes, 1994) using a deuterium correction as given in (Venters
793 et al., 1996). Chemical shift assignments for *Ec*NusG-KOW, *Mt*NusG-KOW and native *Ec*RfaH-
794 KOW were taken from previous studies (Burmann et al., 2012; Mooney et al., 2009; Strauß et
795 al., 2016). The random coil chemical shifts for characterization of the minor species in case of
796 *Vc*RfaH-KOW and hSpt5-KOW were calculated using the Poulsen IDP/IUP random coil
797 chemical shifts calculator tool (https://spin.niddk.nih.gov/bax/nmrserver/Poulsen_rc_CS/).
798
799 Distance restraints for the structure calculation of *Vc*RfaH-KOW were obtained from standard
800 ^{13}C- , and ^{15}N-edited 3D NOESY experiments (Sattler et al., 1999) with mixing times of 120 ms.
801 NOESY cross signals were classified according to their intensities and converted to distance
802 restraints with upper limits of 3 Å (strong), 4 Å (medium), 5 Å (weak) and 6 Å (very weak),

respectively. Hydrogen bonds were identified from corresponding experiments (see below). Psi/Phi angle restraints were obtained from the geometry dependence of the backbone chemical shifts using TALOS (Cornilescu et al., 1999). The structure calculation was performed with XPLOR-NIH version 2.1.2 using a three-stage simulated annealing protocol with floating assignment of prochiral groups including a conformational database potential (Schwieters et al., 2003). Structures were analyzed with XPLOR-NIH and PROCHECK-NMR (Laskowski et al., 1996).

^{15}N-based CEST experiments were conducted according to (Vallurupalli et al., 2012). All samples contained ≈ 0.7 – 1 mM ^{15}N-labeled protein. For initial CEST experiments, the domains were in 20 mM HEPES (pH 7.5), 100 mM NaCl, 10 % (v/v) D_2O and a single CEST B_1 field (ν_1 = 18 - 25 Hz) during an exchange period of 500 ms was employed. Proteins showing an exchange peak in their CEST profiles were further studied in 20 mM Na-phosphate (pH 6.5), 100 mM NaCl, 1 mM EDTA, 10 % (v/v) D_2O to decrease amide proton-H_2O exchange. CEST experiments were then recorded using two different B_1 fields (ν_1 = 13 Hz/26 Hz) and an exchange period of 500 ms. The B_1 frequencies were calibrated using a 1D approach on an isolated signal (Guenneugues et al., 1999). The CEST traces obtained at 13/26 Hz were fitted simultaneously according to a two-state exchange model using ChemEx (version 0.6.1, (Vallurupalli et al., 2012)). Due to the monodisperse distribution of the resulting k_{ex}/p_B values (**Figure 5 – Figure supplement 1**), the CEST traces were then fitted globally, yielding a global k_{ex} and p_B value. Only those CEST profiles were included in the global fit that showed a $\Delta\omega$ > 1 ppm. ^{13}Cα-CEST experiments for *Ec*RfaH-KOW were recorded on a [^{15}N, ^{13}C]-labeled protein sample using a [^{1}H, ^{13}C] constant-time (ct) HSQC based approach (Bouvignies et al., 2014). To maximize the number of analyzable signals, the protein was in 20 mM Na-phosphate (pH 6.5),

826 100 mM NaCl, 1 mM EDTA, 99.9 % (v/v) D_2O (pH uncorrected for D_2O). In this case, the
827 chemical shift was referenced *via* 0.5 mM internal DSS. The experiment was performed at a
828 single B_1 field strength (25 Hz) at an exchange period of 500 ms. The obtained CEST traces were
829 fitted with ChemEx keeping p_B constant at 5.5 %.
830 NMR-based chemical denaturation experiments of the KOW domains were done by recording
831 [^{1}H, ^{15}N]-HSQC and [^{1}H, ^{13}C]-ctHSQC spectra of 80 µM [^{15}N, ^{13}C]-*Ec*RfaH-KOW in 20 mM
832 Na-phosphate (pH 6.5), 100 mM NaCl, 1 mM EDTA, 10 % (v/v) D_2O buffer containing 0 – 8 M
833 urea. The chemical shifts were referenced to 0.5 mM internal DSS.
834 For the NMR-based refolding experiment of *Vc*RfaH under reducing conditions a [^{1}H, ^{15}N]-
835 HSQC spectrum of ^{15}N-*Vc*RfaH in refolding buffer (50 mM Na-phosphate (pH 6.5), 50 mM
836 NaCl, 2 mM DTT) was recorded before the protein was incubated in refolding buffer containing
837 8 M urea for 24 hours. Having recorded another [^{1}H, ^{15}N]-HSQC spectrum urea was removed by
838 stepwise dialysis against 4 l of refolding buffer containing 4 M, 2 M, 1 M, 0.5 M, and 0 M urea,
839 respectively (2-4 hours for the first four steps and overnight for the last step). Finally, a
840 [^{1}H, ^{15}N]-HSQC spectrum of the refolded protein was recorded.
841 Hydrogen bonds were identified from 2D or 3D long range (LR) TROSY based HNCO
842 experiments as previously described (Cordier et al., 2008). All samples contained [^{15}N, ^{13}C]-
843 labeled proteins at 0.7 – 1 mM in 20 mM Na-phosphate (pH 6.5), 100 mM NaCl, 1 mM EDTA,
844 10 % (v/v) D_2O.
845
846
847
848

849 **CD spectroscopy**

850 CD data were collected at a Jasco J-1100 spectrometer (Jasco Deutschland GmbH, Pfungstadt,
851 Germany), using quartz cuvettes (Hellma GmbH & Co. KG, Müllheim, Germany). CD spectra
852 were normalized (**Equation 1**) to obtain the mean residue-weighted ellipticity (Θ_{MRW}):

$$\Theta_{MRW} = \frac{100 \cdot \theta}{N \cdot c \cdot d} \qquad (1)$$

853 θ is the ellipticity in mdeg, *N* the number of amino acids, *c* the protein concentration in mM, and
854 *d* the pathlength of the cuvette in cm.
855 Thermal unfolding and refolding curves were obtained by measuring the CD signal of 15 μM
856 (≈ 0.1 mg/ml) protein buffered by either 10 mM K-phosphate (pH 7.0) or 10 mM K-acetate
857 (pH 4.0), respectively, in a 1 cm quartz cuvette upon heating to 95 °C and subsequently re-
858 cooling to the initial temperature. The scan speed was 1 °C/min, the dwell time 1 min, and the
859 integration time 4 s. Checking the reversibility of thermal unfolding and determination of the
860 wavelength used for temperature transition curves was done by recording far-UV CD spectra at
861 25 °C, then 95 °C, and after subsequent re-cooling to 25 °C in a 2 mm pathlength cuvette using
862 25 μM protein solutions in either 10 mM K-phosphate (pH 7.0) or 10 mM K-acetate (pH 4.0).
863
864 Changes in ellipticity (θ) upon thermal unfolding were analyzed with a two-state model using
865 Fit-o-Mat version 0.752 (Möglich, 2018) to obtain the melting temperature (T_m) and enthalpy
866 change at T_m ($\Delta H_u(T_m)$) of the transition (both fit parameters) (**Equation 2**):
867

$$\theta = f_N \cdot (y_N + m_N \cdot (T - T_m)) + (1 - f_N) \cdot (y_U + m_U \cdot (T - T_m)) \qquad (2)$$

868

with T being the absolute temperature in K, y_N and y_U the y-intercepts, and m_N and m_U the slopes of the N- and U-state baselines, respectively. f_N is the fraction of folded molecules, which is related to the equilibrium constant K_u according to **Equation 3**:

$$f_N = \frac{1}{1 + K_u} \tag{3}$$

Finally, K_u is related to the change in Gibb's free energy of the unfolding reaction (ΔG_u) and $\Delta H_u(T_m)$ by **Equation 4**:

$$K_u = e^{-\Delta G_u/(RT)} \quad \text{with} \quad \Delta G_u = \Delta H_u(T_m) - \frac{T}{T_m} \cdot \Delta H_u(T_m) \tag{4}$$

R is the ideal gas constant.

CD-based chemical equilibrium unfolding experiments were performed at 25 °C. Urea (BioScience Grade; ≈ 10 M) and GdmCl (≈ 8 M; both from Carl Roth GmbH & Co. KG, Karlsruhe, Germany) stock solutions were prepared according to (Pace et al., 1990). Far-UV CD unfolding experiments were conducted using a 1 mm cuvette. All points of the unfolding curves were obtained from individual samples, each containing 40 - 60 µM (≈ 0.25 – 0.4 mg/ml) protein in either 10 mM K-phosphate (pH 7.0) or 10 mM K-acetate (pH 4.0), respectively. All samples were equilibrated over-night. The denaturant concentration of each sample was determined refractrometrically after CD data acquisition. Unfolding curves that indicate a two-state

transition were analyzed using the linear extrapolation method (Santoro and Bolen, 1988) with Fit-o-Mat version 0.752 (Möglich, 2018) to obtain $\Delta G_u(H_2O)$ and the *m*-value (**Equation 5**):

$$S = f_N \cdot (y_N + m_N \cdot [denat]) + (1 - f_N) \cdot (y_U + m_U \cdot [denat]) \quad (5)$$

S is the signal derived from far-UV CD spectroscopy (i.e. the Θ_{MRW}-value), intrinsic Trp fluorescence (for *Vc*RfaH-CTD), or the normalized peak volumes of the [^{1}H, ^{13}C]-ctHSQC major/minor species signals for *Ec*RfaH-KOW residue S139, respectively. [denat] is the denaturant (i.e. urea or GdmCl) concentration in M, y_N and y_U are the y-intercepts, and m_N and $m_{U,}$ the slopes of the N- and U-state baselines, respectively. f_N is given by **Equation 3**. In this case, K_u is defined as (**Equation 6**):

$$K_u = e^{-\Delta G/(RT)} \quad \text{with} \quad \Delta G = \Delta G(H_2O) - m \cdot [\text{denat}] \quad (6)$$

Finally, the $[\text{denat}]_{1/2}$ value is obtained by (**Equation 7**):

$$[\text{denat}]_{1/2} = \frac{\Delta G(H_2O)}{m} \quad (7)$$

Near-UV CD unfolding experiments of *Ec*RfaH-KOW were conducted using a 1 cm quartz cuvette and 0.5 mM protein in 10 mM K-phosphate (pH 7.0). As the exchange between folded and unfolded state is reasonably fast ($k_{ex} \approx 15\ s^{-1}$ at 0 M urea/GdmCl), all points were obtained from a titration of the initial denaturant-free protein sample with a 10 M urea or 8 M GdmCl

907 solution in 10 mM K-phosphate (pH 7.0). The sample was then incubated for 5 min at 25 °C to
908 reach equilibrium. Curves were smoothed mathematically using a Savitzky-Golay filter.
909 To probe reversibility of chemical unfolding and validate incubation times used to reach
910 equilibrium, proteins were dialyzed against 20 mM NH_4HCO_3 (pH 7.0) buffer, shock-frozen,
911 lyophilized and subsequently solved in 10 mM K-phosphate (pH 7.0) or 10 mM K-acetate
912 (pH 4.0) with or without 10 M urea/8 M GdmCl, respectively. CD samples containing the
913 identical denaturant concentration (1–2 samples in pre-transition region, 1 at $[denaturant]_{1/2}$, 1 in
914 post-transition region) were then prepared from the native or unfolded proteins. All samples were
915 equilibrated over-night; far-UV CD spectra were then recorded using a 1 mm quartz cuvette.
916
917 **Fluorescence spectroscopy**
918 Fluorescence spectra were recorded at 25 °C using a Peltier-controlled Fluorolog-3 fluorimeter
919 (Horiba Europe GmbH, Oberursel, Germany) equipped with a 1 cm quartz cuvette (Hellma
920 GmbH & Co. KG, Müllheim, Germany). Samples for chemical denaturation of *Vc*RfaH-KOW
921 contained ≈ 11 µM protein and were prepared as described for the far-UV CD samples. The
922 *Vc*RfaH-KOW Trp residue was excited at 295 nm; emission spectra were then recorded from 300
923 to 400 nm with slit widths between 2.65/2.65 nm and 2.8/2.8 nm (excitation/emission) and an
924 integration time of 0.2 s. Analysis of the resulting denaturation curve was performed as described
925 for CD data.
926 ANS (Sigma/Merck KGaA, Darmstadt, Germany) interaction experiments were conducted by
927 preparing a urea denaturation series of *Ec*RfaH-KOW (final concentration: 5 µM) as described
928 for the CD-based unfolding experiments, equilibrating over-night and adding ANS at a
929 fluorophore:protein ratio of 100:1. Fluorescence spectra were then recorded from 410 to 650 nm

following excitation at 395 nm with slit widths of 2.6/2.6 nm (excitation/emission) and 0.1 s integration time. A control experiment was conducted with identical experiment and instrument setup, respectively, but samples lacking protein. The obtained fluorescence at a given wavelength was then plotted against the urea concentration of the respective sample.

DSC

The KOW domains were in either 10 mM K-acetate (pH 4.0; hSpt5-KOW5) or 10 mM K-phosphate (pH 7.0; all other domains), respectively. Given a lack of Trp residues in most domains, the protein concentration was determined *via* absorption at 205 nm using the molar extinction coefficient (ε_{205}) as calculated by the Protein Calculator tool (Anthis and Clore, 2013). Initial DSC experiments were carried out on a MicroCal VP-DSC instrument (MicroCal/Malvern Panalytical, Malvern, UK; active volume: 509 µl). The samples were vacuum degassed at room temperature just before the measurements. Prior to the protein-buffer scans, several buffer-buffer scans were performed. All thermograms were recorded at a scan rate of 1.5 K/min under an excess pressure of 30 psi in passive feed-back mode from ≈ 10 °C to 110 °C or 130 °C (*Mj*Spt5-KOW5), respectively. The unfolding was calometrically reversible for *Ec*NusG-KOW, *Mt*NusG-KOW, *Mj*Spt5-KOW and *Ec*RfaH-KOW (data not shown). hSpt5-KOW5 aggregated at pH 7.0 upon unfolding at all tested concentrations, whereas *Vc*RfaH-KOW aggregated at concentrations > 0.2 mg/ml.

We repeated the measurements for all proteins but *Mt*NusG-KOW using a MicroCal VP-Capillary DSC instrument (Malvern Panalytical, Malvern, UK; active volume 137 µl). The thermograms were obtained at a heating rate of 1.5 K/min with excess pressure (30 psi) and at mid gain feed-back mode. Buffer-buffer runs were done prior to the protein measurements.

Thermograms were recorded from ≈ 5 °C to 130 °C. The protein concentration was 0.2 – 1 mg/ml for *Ec*NusG-KOW, 0.25 – 1 mg/ml for *Mj*Spt5-KOW, 0.15 – 0.25 mg/ml for hSpt5-KOW5, 0.2 – 1 mg/ml for *Ec*RfaH-KOW and 0.1 – 0.15 mg/ml for *Vc*RfaH-KOW. The measurement for hSpt5-KOW5 was carried out with 10 mM K-acetate (pH 4.0), all other KOW domains were in 10 mM K-phosphate (pH 7.0).

The obtained raw DSC data (VP-DSC data for *Mt*NusG-KOW, VP-Capillary DSC data for all other KOW domains) was scan-rate normalized, the corresponding buffer-buffer baseline was subtracted, and the thermograms were then normalized to one mol of protein. To extract the thermodynamic parameters, the data was fitted to a two-state unfolding model including a temperature-dependent change in heat capacity from native to unfolded state (Viguera et al., 1994). The temperature dependence of the native state heat capacity ($C_{p,0}$) is assumed to be linear (**Equation 8**; note that $C_{p,0}$ contains an instrument-specific offset), whereas the difference in heat capacity to the unfolded state ($\Delta C_{p,u}(T)$) is approximated by a parabolic function (**Equation 9**):

$$C_{p,0} = a_0 + b_0 \cdot T \tag{8}$$

$$\Delta C_{p,u}(T) = a + b \cdot T + c \cdot T^2 \tag{9}$$

The value for the pre-factor of the quadratic term, *c*, was obtained by calculating the theoretical partial molar heat capacity, $C_p(T)$, of the unfolded state for each of the six protein domains at 5, 25, 50, 75, 100 and 125 °C, respectively, according to Makhatadze and Privalov (Makhatadze and Privalov, 1990). Then, the values for $C_p(T)$ were plotted over the temperature and a parabolic function was fitted, yielding *c*.

The concentration-normalized heat capacity (C_p) then is the sum of $C_{p,0}$, the change of the "internal" heat capacity that depends on the fraction of the protein in the folded and unfolded

974 state (i.e. the equilibrium constant K_u), δC_p^{int}, and the excess heat absorption of the unfolding

975 reaction δC_p^{exc} (**Equation 10**):

$$C_p = C_{p,0} + \delta C_p^{int} + \delta C_p^{exc} \quad (10)$$

976

977 With δC_p^{int} and δC_p^{exc} given in **Equation 11**:

978

$$\delta C_p^{int} = \Delta C_{p,u} \cdot \frac{K_u}{1+K_u} \quad \text{and} \quad \delta C_p^{exc} = \frac{(\Delta H_u(T))^2}{RT^2} \cdot \frac{K_u}{(1+K_u)^2} \quad (11)$$

979

980 K_u is related to the change in Gibbs energy of the unfolding reaction ($\Delta G_u(T)$) by (**Equation 12**):

981

$$K_u = e^{-\Delta G_u(T)/(RT)} \quad \text{with} \quad \Delta G_u(T) = \Delta H_u(T) - T \cdot \Delta S_u(T) \quad (12)$$

982

983 The temperature-dependent enthalpy and entropy change ($\Delta H_u(T)$, and $\Delta S_u(T)$, respectively) are

984 given by **Equations 13** and **14**:

985

$$\Delta H_u(T) = \Delta H_u(T_m) + a \cdot (T - T_m) + \frac{b}{2} \cdot (T^2 - T_m^2) + \frac{c}{3} \cdot (T^3 - T_m^3) \quad (13)$$

$$\Delta S_u(T) = \frac{\Delta H_u(T_m)}{T_m} + a \cdot ln\left(\frac{T}{T_m}\right) + b \cdot (T - T_m) + \frac{c}{2} \cdot (T^2 - T_m^2) \quad (14)$$

986

987 During fitting of C_p, parameters a_0, b_0, a, b, T_m and $\Delta H_u(T_m)$ were allowed to float, while c was

988 kept constant.

989

Acknowledgments

We thank I. Artsimovitch for providing pVS13 and F. Werner for providing pGEX-2TK_*Mj*Spt5-KOW. Our sincere thanks go to F.X. Schmid for detailed discussions and valuable comments on the manuscript. We also thank A. Matagne and Birgitta M Wöhrl for helpful discussions, C. M. Johnson for performing DSC measurements, A. Häussermann for carrying our the NMR-based refolding experiment of *Vc*RfaH, and A. Hager for technical support, as well as the Northern Bavarian NMR Centre (NBNC) for providing access to NMR spectrometers. The project was supported by the German Research Foundation grant Ro617/21-1 (to P. Rösch) and COST action CA 15126 ARBRE-MOBIEU (to PKZ, TD, SHK).

Author contributions: SHK and PKZ conceived the project and designed the experiments. SHK supervised the study. UP, RH and PKZ cloned, expressed and purified the constructs. KS, SHK, and PKZ performed and analyzed the NMR experiments. PKZ determined the structure of *Vc*RfaH-KOW. PKZ performed the CD and fluorescence experiments. DSC measurements were carried out by TD and PKZ. Analysis and interpretation of CD, fluorescence and DSC data was done by PKZ. The manuscript was prepared by PKZ and SHK with input of TD and KS.

Competing interests: The authors declare that they have no competing interests.

Data and materials availability: Coordinates for *Vc*RfaH-KOW have been deposited to the Protein Databank (ID: 6TF4). Chemical shifts have been deposited in the Biological Magnetic Resonance Databank under the following accession numbers: #28039 (hSpt5-KOW5), #28040

(*Mj*Spt5-KOW), #28041 (*Vc*RfaH) and #34450 (*Vc*RfaH-CTD). All other data needed to evaluate the conclusions in the paper are present in the paper, in the Supplemental Material, and/or as source data. Plasmids may be requested from the authors (a material transfer agreement is required).

References

Anthis NJ, Clore GM. 2013. Sequence-specific determination of protein and peptide concentrations by absorbance at 205 nm. *Protein Science* **22**:851–858. doi:10.1002/pro.2253

Artsimovitch I, Knauer SH. 2019. Ancient Transcription Factors in the News. *MBio* **10**. doi:10.1128/mBio.01547-18

Artsimovitch I, Landick R. 2002. The Transcriptional Regulator RfaH Stimulates RNA Chain Synthesis after Recruitment to Elongation Complexes by the Exposed Nontemplate DNA Strand. *Cell* **109**:193–203.

Balasco N, Barone D, Vitagliano L. 2015. Structural conversion of the transformer protein RfaH: new insights derived from protein structure prediction and molecular dynamics simulations. *J Biomol Struct Dyn* **33**:2173–2179. doi:10.1080/07391102.2014.994188

Belogurov GA, Mooney RA, Svetlov V, Landick R, Artsimovitch I. 2009. Functional specialization of transcription elongation factors. *EMBO J* **28**:112–122. doi:10.1038/emboj.2008.268

Belogurov GA, Vassylyeva MN, Svetlov V, Klyuyev S, Grishin NV, Vassylyev DG, Artsimovitch I. 2007. Structural Basis for Converting a General Transcription Factor into an Operon-Specific Virulence Regulator. *Mol Cell* **26**:117–129. doi:10.1016/j.molcel.2007.02.021

Bermel W, Bertini I, Duma L, Felli IC, Emsley L, Pierattelli R, Vasos PR. 2005. Complete Assignment of Heteronuclear Protein Resonances by Protonless NMR Spectroscopy. *Angew Chem Int Ed* **44**:3089–3092. doi:10.1002/anie.200461794

Bernecky C, Plitzko JM, Cramer P. 2017. Structure of a transcribing RNA polymerase II-DSIF complex reveals a multidentate DNA-RNA clamp. *Nat Struct Mol Biol* **24**:809–815. doi:10.1038/nsmb.3465

1046 Bernhardt NA, Hansmann UHE. 2018. Multifunnel Landscape of the Fold-Switching Protein
1047 RfaH-CTD. *J Phys Chem B* **122**:1600–1607. doi:10.1021/acs.jpcb.7b11352
1048 Bouvignies G, Vallurupalli P, Kay LE. 2014. Visualizing Side Chains of Invisible Protein
1049 Conformers by Solution NMR. *J Molr Biol* **426**:763–774. doi:10.1016/j.jmb.2013.10.041
1050 Bryan PN, Orban J. 2010. Proteins that switch folds. *Curr Opin Struct Biol* **20**:482–488.
1051 doi:10.1016/j.sbi.2010.06.002
1052 Burmann BM, Knauer SH, Sevostyanova A, Schweimer K, Mooney RA, Landick R,
1053 Artsimovitch I, Rösch P. 2012. An α Helix to β Barrel Domain Switch Transforms the
1054 Transcription Factor RfaH into a Translation Factor. *Cell* **150**:291–303.
1055 doi:10.1016/j.cell.2012.05.042
1056 Burmann BM, Schweimer K, Luo X, Wahl MC, Stitt BL, Gottesman ME, Rösch P. 2010. A
1057 NusE:NusG Complex Links Transcription and Translation. *Science* **328**:501–504.
1058 doi:10.1126/science.1184953
1059 Carter HD, Svetlov V, Artsimovitch I. 2004. Highly Divergent RfaH Orthologs from Pathogenic
1060 Proteobacteria Can Substitute for *Escherichia coli* RfaH both In Vivo and In Vitro. *J Bacteriol*
1061 **186**:2829–2840. doi:10.1128/JB.186.9.2829-2840.2004
1062 Cordier F, Nisius L, Dingley AJ, Grzesiek S. 2008. Direct detection of N−H···O=C hydrogen
1063 bonds in biomolecules by NMR spectroscopy. *Nat Protoc* **3**:235–241.
1064 doi:10.1038/nprot.2007.498
1065 Cornilescu G, Delaglio F, Bax A. 1999. Protein backbone angle restraints from searching a
1066 database for chemical shift and sequence homology. *J Biomol NMR* **13**:289–302.
1067 doi:10.1023/A:1008392405740
1068 de Marco A, Berrow N, Lebendiker M, Garcia-Alai M, Knauer SH, Lopez-Mendez B, Matagne

A, Parret A, Remans K, Uebel S, Raynal B. 2021. Quality control of protein reagents for the improvement of research data reproducibility. *Nat Commun* **12**:2795. doi:10.1038/s41467-021-23167-z

Dishman AF, Tyler RC, Fox JC, Kleist AB, Prehoda KE, Babu MM, Peterson FC, Volkman BF. 2021. Evolution of fold switching in a metamorphic protein. *Science* **371**:86–90. doi:10.1126/science.abd8700

Dishman AF, Volkman BF. 2018. Unfolding the Mysteries of Protein Metamorphosis. *ACS Chem Biol* **13**:1438–1446. doi:10.1021/acschembio.8b00276

Epstein CJ, Goldberger RF, Anfinsen CB. 1963. The Genetic Control of Tertiary Protein Structure: Studies With Model Systems. *Cold Spring Harbor Symposia on Quantitative Biology* **28**:439–449. doi:10.1101/SQB.1963.028.01.060

Galaz-Davison P, Molina JA, Silletti S, Komives EA, Knauer SH, Artsimovitch I, Ramírez-Sarmiento CA. 2020. Differential Local Stability Governs the Metamorphic Fold Switch of Bacterial Virulence Factor RfaH. *Biophys J* **118**:96–104. doi:10.1016/j.bpj.2019.11.014

Gc JB, Bhandari YR, Gerstman BS, Chapagain PP. 2014. Molecular Dynamics Investigations of the α-Helix to β-Barrel Conformational Transformation in the RfaH Transcription Factor. *J Phys Chem B* **118**:5101–5108. doi:10.1021/jp502193v

Green MR, Sambrook J, Sambrook J. 2012. Molecular cloning: a laboratory manual, 4th ed. ed. Cold Spring Harbor, N.Y: Cold Spring Harbor Laboratory Press.

Grzesiek S, Cordier F, Jaravine V, Barfield M. 2004. Insights into biomolecular hydrogen bonds from hydrogen bond scalar couplings. *Prog Nucl Magn Reson Spectrosc* **45**:275–300. doi:10.1016/j.pnmrs.2004.08.001

Guenneugues M, Berthault P, Desvaux H. 1999. A Method for Determining B_1 Field

1092 Inhomogeneity. Are the Biases Assumed in Heteronuclear Relaxation Experiments Usually
1093 Underestimated? *J Magn Reson* **136**:118–126. doi:10.1006/jmre.1998.1590
1094 Gupta R, Yadav S, Ahmad F. 1996. Protein Stability: Urea-Induced versus Guanidine-Induced
1095 Unfolding of Metmyoglobin. *Biochemistry* **35**:11925–11930. doi:10.1021/bi961079g
1096 Hirtreiter A, Damsma GE, Cheung ACM, Klose D, Grohmann D, Vojnic E, Martin ACR,
1097 Cramer P, Werner F. 2010. Spt4/5 stimulates transcription elongation through the RNA
1098 polymerase clamp coiled-coil motif. *Nucleic Acids Res* **38**:4040–4051. doi:10.1093/nar/gkq135
1099 Hyberts SG, Milbradt AG, Wagner AB, Arthanari H, Wagner G. 2012. Application of iterative
1100 soft thresholding for fast reconstruction of NMR data non-uniformly sampled with
1101 multidimensional Poisson Gap scheduling. *J Biomol NMR* **52**:315–327. doi:10.1007/s10858-012-
1102 9611-z
1103 Jeffery CJ. 2014. An introduction to protein moonlighting. *Biochem Soc Trans* **42**:1679–1683.
1104 doi:10.1042/BST20140226
1105 Jeffery CJ. 1999. Moonlighting proteins. *Trends Biochem Sci* **24**:8–11. doi:10.1016/s0968-
1106 0004(98)01335-8
1107 Joseph JA, Chakraborty D, Wales DJ. 2019. Energy Landscape for Fold-Switching in Regulatory
1108 Protein RfaH. *J Chem Theory Comput* **15**:731–742. doi:10.1021/acs.jctc.8b00912
1109 Jumper J, Evans R, Pritzel A, Green T, Figurnov M, Ronneberger O, Tunyasuvunakool K, Bates
1110 R, Žídek A, Potapenko A, Bridgland A, Meyer C, Kohl SAA, Ballard AJ, Cowie A, Romera-
1111 Paredes B, Nikolov S, Jain R, Adler J, Back T, Petersen S, Reiman D, Clancy E, Zielinski M,
1112 Steinegger M, Pacholska M, Berghammer T, Bodenstein S, Silver D, Vinyals O, Senior AW,
1113 Kavukcuoglu K, Kohli P, Hassabis D. 2021. Highly accurate protein structure prediction with
1114 AlphaFold. *Nature* **596**:583–589. doi:10.1038/s41586-021-03819-2

1115 Kim AK, Porter LL. 2021. Functional and Regulatory Roles of Fold-Switching Proteins.
1116 *Structure* **29**:6–14. doi:10.1016/j.str.2020.10.006
1117 Kim C, Choi J, Lee SJ, Welsh WJ, Yoon S. 2009. NetCSSP: web application for predicting
1118 chameleon sequences and amyloid fibril formation. *Nucleic Acids Res* **37**:W469–W473.
1119 doi:10.1093/nar/gkp351
1120 Klein BJ, Bose D, Baker KJ, Yusoff ZM, Zhang X, Murakami KS. 2011. RNA polymerase and
1121 transcription elongation factor Spt4/5 complex structure. *Proc Natl Acad Sci USA* **108**:546–550.
1122 doi:10.1073/pnas.1013828108
1123 Knauer SH, Artsimovitch I, Rösch P. 2012. Transformer proteins. *Cell Cycle* **11**:4289–4290.
1124 doi:10.4161/cc.22468
1125 Laskowski RA, Rullmannn JA, MacArthur MW, Kaptein R, Thornton JM. 1996. AQUA and
1126 PROCHECK-NMR: programs for checking the quality of protein structures solved by NMR. *J*
1127 *Biomol NMR* **8**:477–486.
1128 Lella M, Mahalakshmi R. 2017. Metamorphic Proteins: Emergence of Dual Protein Folds from
1129 One Primary Sequence. *Biochemistry* **56**:2971–2984. doi:10.1021/acs.biochem.7b00375
1130 Lescop E, Schanda P, Brutscher B. 2007. A set of BEST triple-resonance experiments for time-
1131 optimized protein resonance assignment. *Journal of Magnetic Resonance* **187**:163–169.
1132 doi:10.1016/j.jmr.2007.04.002
1133 Li S, Xiong B, Xu Y, Lu T, Luo X, Luo C, Shen J, Chen K, Zheng M, Jiang H. 2014.
1134 Mechanism of the All-α to All-β Conformational Transition of RfaH-CTD: Molecular Dynamics
1135 Simulation and Markov State Model. *J Chem Theory Comput* **10**:2255–2264.
1136 doi:10.1021/ct5002279
1137 Makhatadze GI. 1999. Thermodynamics of Protein Interactions with Urea and Guanidinium

Hydrochloride. *J Phys Chem B* **103**:4781–4785. doi:10.1021/jp990413q

Makhatadze GI, Privalov PL. 1990. Heat Capacity of Proteins I. Partial Molar Heat Capacity of Individual Amino Acid Residues in Aqueous Solution: Hydration Effect. *J Mol Biol* **213**:375–384. doi:10.1016/S0022-2836(05)80197-4

Maxwell KL, Wildes D, Zarrine-Afsar A, De Los Rios MA, Brown AG, Friel CT, Hedberg L, Horng J-C, Bona D, Miller EJ, Vallée-Bélisle A, Main ERG, Bemporad F, Qiu L, Teilum K, Vu N-D, Edwards AM, Ruczinski I, Poulsen FM, Kragelund BB, Michnick SW, Chiti F, Bai Y, Hagen SJ, Serrano L, Oliveberg M, Raleigh DP, Wittung-Stafshede P, Radford SE, Jackson SE, Sosnick TR, Marqusee S, Davidson AR, Plaxco KW. 2005. Protein folding: Defining a "standard" set of experimental conditions and a preliminary kinetic data set of two-state proteins. *Protein Sci* **14**:602–616. doi:10.1110/ps.041205405

Meyer O, Schlegel HG. 1983. Biology of Aerobic Carbon Monoxide-Oxidizing Bacteria. *Annu Rev Microbiol* **37**:277–310. doi:10.1146/annurev.mi.37.100183.001425

Meyer PA, Li S, Zhang M, Yamada K, Takagi Y, Hartzog GA, Fu J. 2015. Structures and Functions of the Multiple KOW Domains of Transcription Elongation Factor Spt5. *Mol Cell Biol* **35**:3354–3369. doi:10.1128/MCB.00520-15

Möglich A. 2018. An Open-Source, Cross-Platform Resource for Nonlinear Least-Squares Curve Fitting. *J Chem Educ* **95**:2273–2278. doi:10.1021/acs.jchemed.8b00649

Mooney RA, Schweimer K, Rösch P, Gottesman M, Landick R. 2009. Two Structurally Independent Domains of *E. coli* NusG Create Regulatory Plasticity *via* Distinct Interactions with RNA Polymerase and Regulators. *J Mol Biol* **391**:341–358. doi:10.1016/j.jmb.2009.05.078

Murzin AG. 2008. BIOCHEMISTRY: Metamorphic Proteins. *Science* **320**:1725–1726. doi:10.1126/science.1158868

Pace CN, Shirley BA, Thomson JA, Creighton TE. 1990. Measuring the conformational stability of a protein. *Protein Structure: A Practical Approach*. pp. 311–330.

Pervushin K, Riek R, Wider G, Wuthrich K. 1997. Attenuated T_2 relaxation by mutual cancellation of dipole-dipole coupling and chemical shift anisotropy indicates an avenue to NMR structures of very large biological macromolecules in solution. *Proc Natl Acad Sci USA s* **94**:12366–12371. doi:10.1073/pnas.94.23.12366

Porter LL, Looger LL. 2018. Extant fold-switching proteins are widespread. *Proc Natl Acad Sci USA* **115**:5968–5973. doi:10.1073/pnas.1800168115

Ramírez-Sarmiento CA, Noel JK, Valenzuela SL, Artsimovitch I. 2015. Interdomain Contacts Control Native State Switching of RfaH on a Dual-Funneled Landscape. *PLoS Comput Biol* **11**:e1004379. doi:10.1371/journal.pcbi.1004379

Salzmann M, Pervushin K, Wider G, Senn H, Wuthrich K. 1998. TROSY in triple-resonance experiments: New perspectives for sequential NMR assignment of large proteins. *Proc Natl Acad Sci USA* **95**:13585–13590. doi:10.1073/pnas.95.23.13585

Santoro MM, Bolen DW. 1988. Unfolding Free Energy Changes Determined by the Linear Extrapolation Method. 1. Unfolding of Phenylmethanesulfonyl α-Chymotrypsin Using Different Denaturants. *Biochemistry* **27**:8063–8068. doi:10.1021/bi00421a014

Sattler M, Schleucher J, Griesinger C. 1999. Heteronuclear multidimensional NMR experiments for the structure determination of proteins in solution employing pulsed field gradients. *Prog Nucl Magn Reson Spectrosc* **34**:93–158.

Schanda P, Van Melckebeke H, Brutscher B. 2006. Speeding Up Three-Dimensional Protein NMR Experiments to a Few Minutes. *J Am Chem Soc* **128**:9042–9043. doi:10.1021/ja062025p

Schwieters CD, Kuszewski JJ, Tjandra N, Clore GM. 2003. The Xplor-NIH NMR molecular

structure determination package. *J Magn Reson* **160**:65–73.

Seifi B, Wallin S. 2021. The C-terminal domain of transcription factor RfaH: Folding, fold switching and energy landscape. *Biopolymers* e23420. doi:10.1002/bip.23420

Sharma D, Rajarathnam K. 2000. ^{13}C NMR chemical shifts can predict disulfide bond formation. *J Biomol NMR* **18**:165–171. doi:10.1023/A:1008398416292

Shi D, Svetlov D, Abagyan R, Artsimovitch I. 2017. Flipping states: a few key residues decide the winning conformation of the only universally conserved transcription factor. *Nucleic Acids Res* **45**:8835–8843. doi:10.1093/nar/gkx523

Strauß M, Schweimer K, Burmann BM, Richter A, Güttler S, Wöhrl BM, Rösch P. 2016. The two domains of *Mycobacterium tuberculosis* NusG protein are dynamically independent. *J Biomol Struct Dyn* **34**:352–361. doi:10.1080/07391102.2015.1031700

Tomar SK, Knauer SH, Nandymazumdar M, Rösch P, Artsimovitch I. 2013. Interdomain contacts control folding of transcription factor RfaH. *Nucleic Acids Res* **41**:10077–10085. doi:10.1093/nar/gkt779

Tunyasuvunakool K, Adler J, Wu Z, Green T, Zielinski M, Žídek A, Bridgland A, Cowie A, Meyer C, Laydon A, Velankar S, Kleywegt GJ, Bateman A, Evans R, Pritzel A, Figurnov M, Ronneberger O, Bates R, Kohl SAA, Potapenko A, Ballard AJ, Romera-Paredes B, Nikolov S, Jain R, Clancy E, Reiman D, Petersen S, Senior AW, Kavukcuoglu K, Birney E, Kohli P, Jumper J, Hassabis D. 2021. Highly accurate protein structure prediction for the human proteome. *Nature* **596**:590–596. doi:10.1038/s41586-021-03828-1

Tyler RC, Murray NJ, Peterson FC, Volkman BF. 2011. Native-state interconversion of a metamorphic protein requires global unfolding. *Biochemistry* **50**:7077–7079. doi:10.1021/bi200750k

Vallurupalli P, Bouvignies G, Kay LE. 2012. Studying "Invisible" Excited Protein States in Slow Exchange with a Major State Conformation. *J Am Chem Soc* **134**:8148–8161. doi:10.1021/ja3001419

van der Lee R, Buljan M, Lang B, Weatheritt RJ, Daughdrill GW, Dunker AK, Fuxreiter M, Gough J, Gsponer J, Jones DT, Kim PM, Kriwacki RW, Oldfield CJ, Pappu RV, Tompa P, Uversky VN, Wright PE, Babu MM. 2014. Classification of intrinsically disordered regions and proteins. *Chem Rev* **114**:6589–6631. doi:10.1021/cr400525m

Vassylyeva MN, Svetlov V, Klyuyev S, Devedjiev YD, Artsimovitch I, Vassylyev DG. 2006. Crystallization and preliminary crystallographic analysis of the transcriptional regulator RfaH from *Escherichia coli* and its complex with ops DNA. *Acta Crystallogr F Struct Biol Cryst Commun* **62**:1027–1030. doi:10.1107/S174430910603658X

Venters RA, Farmer II BT, Fierke CA, Spicer LD. 1996. Characterizing the Use of Perdeuteration in NMR Studies of Large Proteins: ^{13}C, ^{15}N and ^{1}H Assignments of Human Carbonic Anhydrase II. *J Mol Biol* **264**:1101–1116. doi:10.1006/jmbi.1996.0699

Viguera AR, Martinez JC, Filimonov VV, Mateo PL, Serrano L. 1994. Thermodynamic and Kinetic Analysis of the SH3 Domain of Spectrin Shows a Two-State Folding Transition. *Biochemistry* **33**:2142–2150. doi:10.1021/bi00174a022

Werner F. 2012. A Nexus for Gene Expression-Molecular Mechanisms of Spt5 and NusG in the Three Domains of Life. *J Mol Biol* **417**:13–27. doi:10.1016/j.jmb.2012.01.031

Wishart DS, Sykes BD. 1994. [12] Chemical shifts as a tool for structure determinationMethods in Enzymology. Elsevier. pp. 363–392. doi:10.1016/S0076-6879(94)39014-2

Xiong L, Liu Z. 2015. Molecular dynamics study on folding and allostery in RfaH. *Proteins* **83**:1582–1592. doi:10.1002/prot.24839

1230 Xun S, Jiang F, Wu Y-D. 2016. Intrinsically disordered regions stabilize the helical form of the
1231 C-terminal domain of RfaH: A molecular dynamics study. *Bioorg Med Chem* **24**:4970–4977.
1232 doi:10.1016/j.bmc.2016.08.012
1233 Zamora- Carreras H, Maestro B, Sanz JM, Jiménez MA. 2020. Turncoat Polypeptides: We
1234 Adapt to Our Environment. *Chem Bio Chem* **21**:432–441. doi:10.1002/cbic.201900446
1235 Zuber PK, Hahn L, Reinl A, Schweimer K, Knauer SH, Gottesman ME, Rösch P, Wöhrl BM.
1236 2018. Structure and nucleic acid binding properties of KOW domains 4 and 6-7 of human
1237 transcription elongation factor DSIF. *Sci Rep* **8**:11660. doi:10.1038/s41598-018-30042-3
1238 Zuber PK, Schweimer K, Rösch P, Artsimovitch I, Knauer SH. 2019. Reversible fold-switching
1239 controls the functional cycle of the antitermination factor RfaH. *Nat Commun* **10**:702.
1240 doi:10.1038/s41467-019-08567-6
1241

Supplemental Material

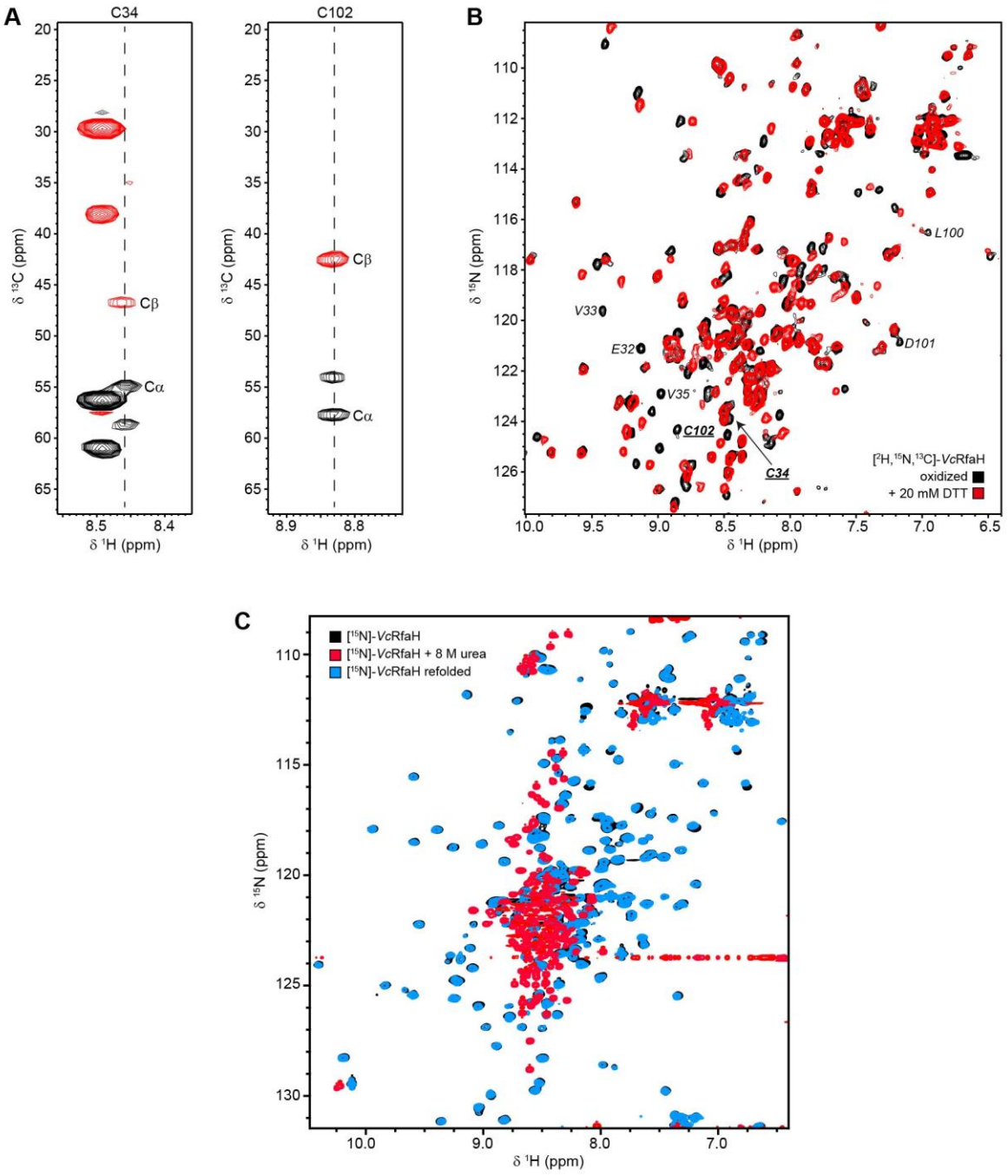

1244

1245 **Figure 1 – Figure supplement 1.** Disulfide bridge formation in *Vc*RfaH. (**A**) Strips of the
1246 HNCACB experiment corresponding to *Vc*RfaH residues C34 and C102, respectively. Signals
1247 arising from the cystein's Cα and Cβ carbons (indicative of a cysteine in a disulfide-bridge) are
1248 labeled. (**B**) [^{1}H, ^{15}N]-HSQC spectra of [^{2}H, ^{13}C, ^{15}N]-*Vc*RfaH in the absence (black) or presence

(red) of 20 mM DTT. Signals of the two disulfide bridge forming residues, C34 and C102, and their sequential neighbors are labeled. (**C**) Refolding of *Vc*RfaH under reducing conditions. [^{1}H, ^{15}N]-HSQC spectra of 150 µM ^{15}N-*Vc*RfaH (black), 39 µM ^{15}N-*Vc*RfaH after incubation in the presence of 8 M urea for 24 hours (red), and 40 µM ^{15}N-*Vc*RfaH upon refolding (cyan).

Figure 1 – Figure supplement 2. Solution structure statistics for *Vc*RfaH-KOW.

Experimental derived restraints		
Distance restraints		
	NOEs unique (total)	630 (734)
	intraresidual	59
	sequential	187
	medium range	89
	long range	295
	hydrogen bonds	2 · 18
Dihedral restraints		76
Restraint violation		
Average distance restraint violation (Å)		0.002584 ± 0.000700
Maximum distance restraint violation (Å)		0.12
Average dihedral restraint violation (°)		0.0654 ± 0.0265
Maximum dihedral restraint violation (°)		0.71
Deviation from ideal geometry		
Bond length (Å)		0.000544 ± 0.000039
Bond angle (Å)		0.1096 ± 0.0056
Coordinate precision *,†		
Backbone heavy atoms (Å)		0.32
All heavy atoms (Å)		0.90
Ramachandran plot statistics ‡ (%)		91.8 / 7.9 / 0.2 / 0.1

* The precision of the coordinates is defined as the average atomic root mean square difference between the accepted simulated annealing structures and the corresponding mean structure calculated for the given sequence region.

† calculated for residues 116 - 165

‡ Ramachandran plot statistics are determined by PROCHECK and noted by most favored/ additionally allowed/generously allowed/disallowed.

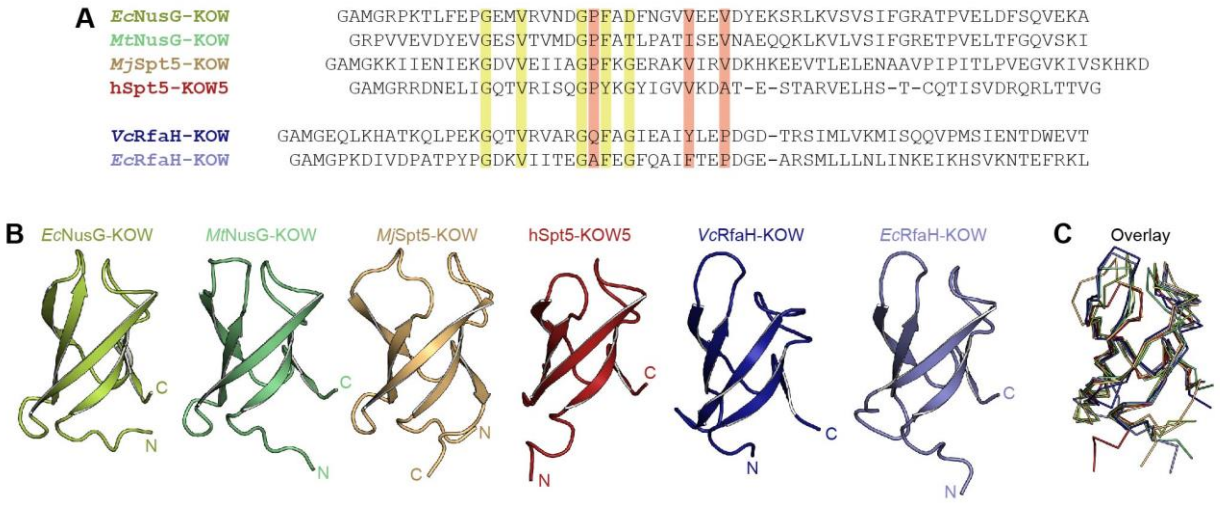

Figure 1 – Figure supplement 3. Structure comparison of KOW domains used in this study. (**A**) Structure-based sequence alignment of the KOW constructs used in this study. Highly conserved residues are highlighted in green, residues that differ among NusG-KOW/Spt5-KOW and RfaH-KOW domains are colored red. (**B**) Structures of the six KOW domains shown in cartoon representation. N- and C-termini are labeled. PDB-IDs: 2JVV (*Ec*NusG-KOW), 2MI6 (*Mt*NusG-KOW), 4ZN3 (*Mj*Spt5-KOW), 2E70 (hSpt5-KOW5), 2LCL (*Ec*RfaH-KOW), 6TF4 (*Vc*RfaH-KOW). (**C**) Structural alignment of the six KOW domains. The proteins are shown as ribbons. Orientation and colors as in (B).

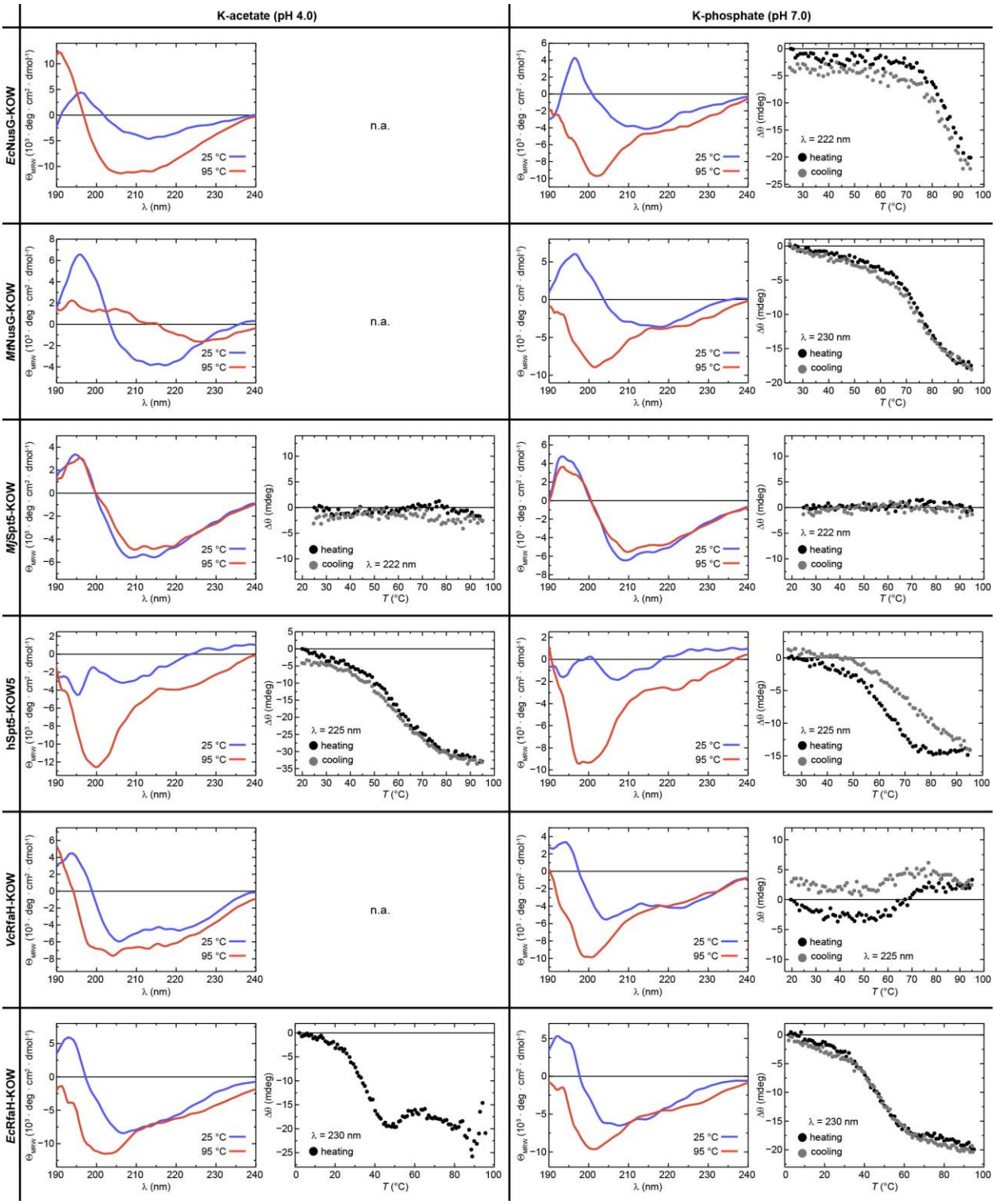

Figure 2 – Figure supplement 1. Reversibility of thermal unfolding. The graphs show CD spectra of the six KOW domains at 25 °C (blue) and at 95 °C (left) together with the change in

ellipticity, Δθ, during heating from 25 °C to 95 °C (filled black circles) and subsequent cooling to the initial temperature (filled grey circles), each at pH 4.0 (left) and pH 7.0 (right). When aggregation was already apparent from the CD spectra acquired at 95 °C (i.e. the shape of the spectrum did not correspond to that of an unfolded protein), no thermal unfolding/refolding curves were recorded (n.a.). Due to its hyperthermophilic source organism, *Mj*Spt5-KOW could not be denatured at either pH.

Figure 2 – Figure supplement 2. Selected thermodynamic parameters of the six KOW domains. The values were derived from thermal denaturations monitored by DSC and CD spectroscopy. Standard deviations result from data fitting.

Parameter	*Ec*NusG-KOW	*Mt*NusG-KOW	*Mj*Spt5-KOW	hSpt5-KOW5	*Ec*RfaH-KOW	*Vc*RfaH-KOW
T_m (°C) pH 7 / pH 4						
CD	- § / -	76.6 ± 0.874 / -	- †/ - †	- / 60.5 ± 0.771	50.3 ± 0.388 / -	65.2 ± 1.78 / -
DSC	87.0 ± 0.0485 /-	77.0 ± 0.0885 /-	111 ± 0.0326 / -	- / 58.0 ± 0.162	47.3 ± 0.143 / -	70.2 ± 0.379 / -
ΔH_u (T_m) (kJ/mol) pH 7 / pH 4						
CD	- § / -	193 ± 11.3 / -	- †/ - †	- / 140 ± 12.4	121 ± 5.15 / -	162 ± 2.91 / -
DSC	222 ± 0.339 / -	192 ± 0.417 / -	293 ± 0.345 / -	- / 117 ± 0.735	129 ± 0.432 / -	169 ± 1.56 / -
ΔC_p (T_m) (kJ/(K mol)) pH 7 / pH 4	0.800 / -	0.346 / -	- §/ -	- / 2.27	2.18 / -	0.148 / -

† No denaturation.

§ Data was not fitted due to the lack of the baseline of the unfolded state.

Figure 3 – Figure supplement 1. Thermodynamic parameters of the six KOW domains. The values were derived from chemical denaturations monitored by DSC and CD spectroscopy as well as fluorescence spectroscopy where indicated. Standard deviations result from data fitting.

Parameter	*Ec*NusG-KOW	*Mt*NusG-KOW	*Mj*Spt5-KOW	hSpt5-KOW5	*Ec*RfaH-KOW	*Vc*RfaH-KOW
$\Delta G_u(H_2O)$ (25 °C) (kJ/mol)						
urea, pH 4	19.8 ± 2.21	22.4 ± 3.46	- ‡	6.24 ± 4.42	- (native state aggregation)	10.8 ± 1.66 (10.8 ± 0.90)*
urea, pH 7	27.7 ± 4.21	26.4 ± 6.16	- ‡	14.3 ± 2.90	three-state	14.0 ± 1.74 (13.9 ± 0.61)*
GdmCl, pH 7	11.7 ± 2.07	15.7 ± 3.99	45.4 ± 4.83	7.37 ± 3.16	three-state	2.87 ± 4.92 (2.84 ± 6.55)*
m (25 °C) (kJ/ (mol M)) ‖						
urea, pH 4	2.51 ± 0.453	4.18 ± 0.660	- ‡	3.25 ± 0.857	- (native state aggregation)	2.91 ± 0.396 (2.98 ± 0.22)*
urea, pH 7	3.84 ± 0.681	5.71 ± 1.32	- ‡	3.83 ± 0.820	three-state	2.98 ± 0.388 (3.13 ± 0.14)*
GdmCl, pH 7	5.22 ± 0.809	8.26 ± 1.87	9.02 ± 0.984	4.95 ± 1.31	three-state	7.71 ± 3.68 (7.86 ± 4.29)*
$[Denat]_{1/2}$ (25 °C) (M)						
urea, pH 4	7.89	5.36	>10 ‡	1.92	- (native state aggregation)	3.71 (3.62)*
urea, pH 7	7.21	4.62	>10 ‡	3.73	~2.25 / ~ 4.25	4.70 (4.44)*
GdmCl, pH 7	2.24	1.90	5.03	1.49	~0.6 / ~1.3	0.37 (0.36)*

* Values were determined by fluorescence-based unfolding experiments

‡ No denaturation possible.

‖ The *m*-value is a measure of the broadness of the transition and correlates with the difference in the accessible surface area between N and U, and the transition midpoint.

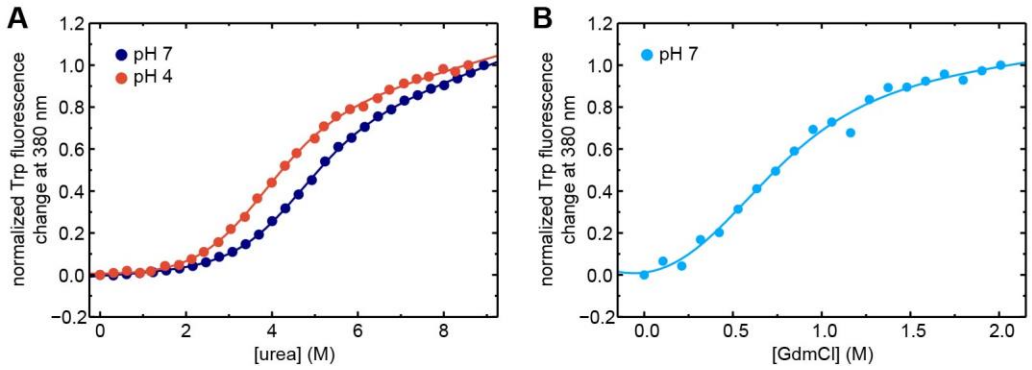

Figure 3 – Figure supplement 2. Chemical unfolding of *Vc*RfaH-KOW monitored by change in Trp fluorescence. (**A**), (**B**) The curves show the normalized Trp fluorescence change at 380 nm of *Vc*RfaH-KOW, obtained after over-night incubation of the protein in the presence of increasing concentrations of (A) urea at pH 4.0 (filled blue circles) or pH 7.0 (filled red circles) or (B) GdmCl at pH 7.0 (filled light blue circles). The lines represent fits to a two-state unfolding model.

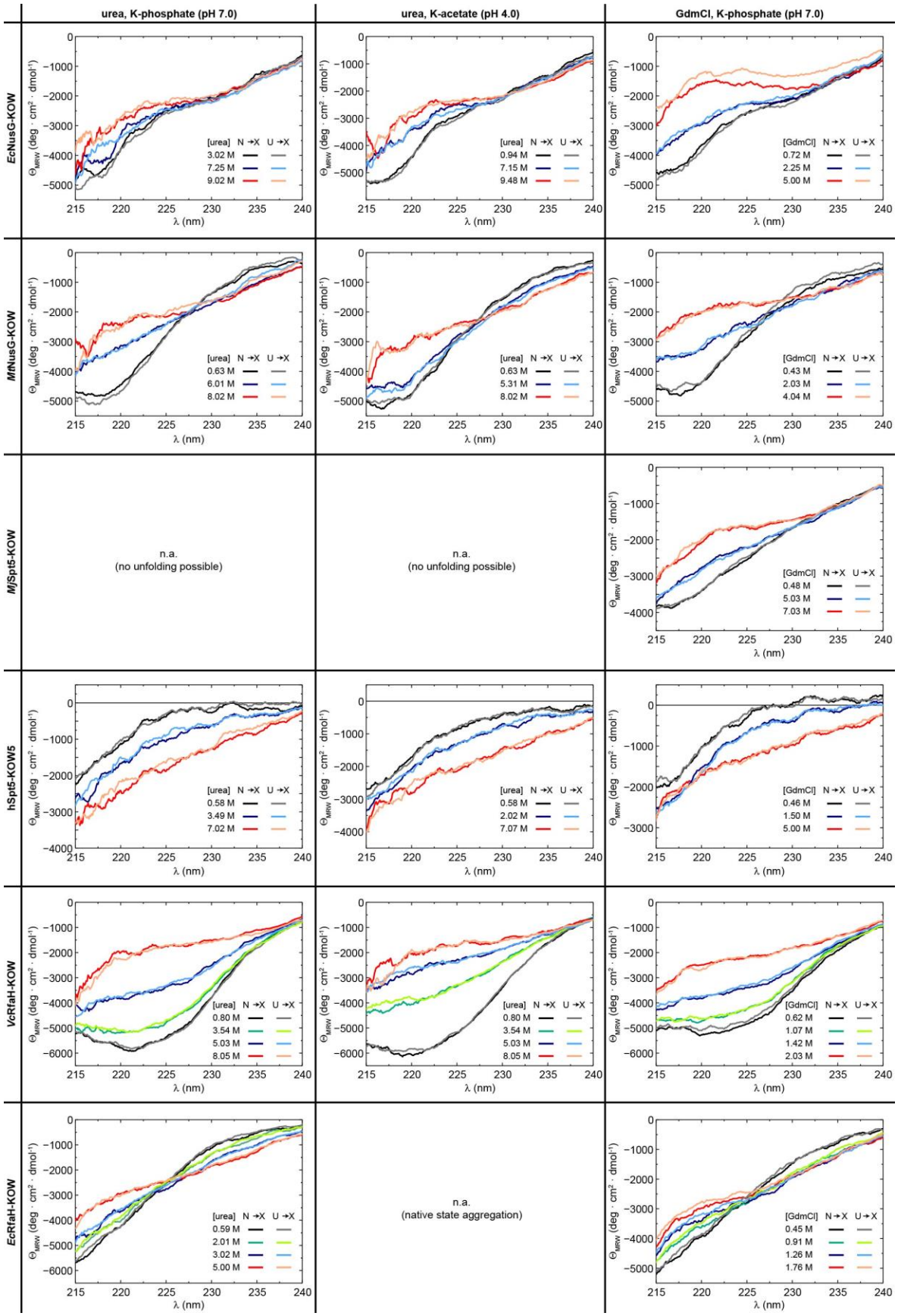

1307

Figure 3 – Figure supplement 3. Reversibility of chemical denaturation. CD spectra of the six protein domains acquired at the indicated denaturant concentration and buffer. In order to check the reversibility, two spectra at identical denaturant concentration were obtained by adding the native protein from a solution containing no denaturant to the desired denaturant concentration (N → X), or by adding the unfolded protein from a solution containing 10 M urea/8 M GdmCl to a solution containing the desired denaturant concentration (U → X). The color code is indicated.

Figure 4 – Figure supplement 1. Quantification of H-bond strengths from LR-HNCO NMR experiments for all KOW domains.

		*Ec*NusG-KOW				*Mt*NusG-KOW				*Mj*Spt5-KOW			
H-bond #	β-sheet	Donor	Acceptor	$\lvert^{h3}J_{NC'}\rvert$ (Hz)	σ $\lvert^{h3}J_{NC'}\rvert$ (Hz)	Donor	Acceptor	$\lvert^{h3}J_{NC'}\rvert$ (Hz)	σ $\lvert^{h3}J_{NC'}\rvert$ (Hz)	Donor	Acceptor	$\lvert^{h3}J_{NC'}\rvert$ (Hz)	σ $\lvert^{h3}J_{NC'}\rvert$ (Hz)
1	β1-β2	131	148	0.69	0.0077	188	205	0.61	0.0098	92	109	0.70	0.013
2	β1-β2	148	132	0.72	0.0083	205	189	0.69	0.0094	109	93	0.79	0.0088
3	β1-β2	134	146	0.67	0.0081	191	203	0.56	0.011	95	107	0.77	0.012
4	β1-β2	146	134	0.62	0.0096	203	191	0.62	0.0094	107	95	0.67	0.0095
5	β1-β2	136	144	0.65	0.0073	193	201	0.65	0.0080	97	105	0.68	0.048
6	β1-β2	143	136	0.65	0.0088	200	193	0.76	0.013	104	97	0.82	0.012
7	β2-β3	147	161	0.37	0.0105	204	218	0.31	0.015	108	122	0.54	0.010
8	β2-β3	161	147	Peak overlap		218	204	0.69	0.011	122	108	0.65	0.010
9	β2-β3	149	159	0.67	0.012	206	216	0.53	0.013	110	120	0.57	0.030
10	β2-β3	159	150	0.50	0.0086	216	207	0.45	0.012	120	111	0.60	0.010
11	β2-β3	152	157	0.46	0.019	209	214	Peak overlap		113	118	-	-
12	β3-β4	158	173	0.78	0.0077	215	230	0.83	0.0088	119	134	No HNCO peak	
13	β3-β4	173	158	0.64	0.010	230	215	0.62	0.011	134	119	0.62	0.010
14	β3-β4	160	171	0.73	0.0056	217	228	0.75	0.0089	121	132	0.88	0.012
15	β3-β4	171	161	Peak overlap		228	217	0.73	0.0062	132	121	0.47	0.014
16	β3-β4	162	169	0.51	0.0074	219	226	0.50	0.0090	123	130	No H-bond distance	
17	β3-β4	169	162	0.60	0.0066	226	219	0.61	0.0091	No equivalent		-	-
18	β3-β4	167	164	-	-	224	221	0.20	0.019	No equivalent		-	-
19	β5-β1	137	177	0.46	0.017	194	234	0.52	0.025	98	138	No HNCO peak	
20	β5-β1	179	135	Peak overlap		236	192	0.47	0.016	140	96	Peak overlap	
21	β5-β1	135	179	0.73	0.0060	192	236	Peak overlap		96	140	Peak overlap	
22	β5-β1	181	133	-	-	238	190	-	-	142	94	0.46	0.023
23	β5-β1	No equivalent		-	-	No equivalent		-	-	143	94	0.27	0.022
24	β5-β1	No equivalent		-	-	No equivalent		-	-	94	143	0.57	0.010

		hSpt5-KOW5				*Ec*RfaH-KOW				*Vc*RfaH-KOW			
H-bond #	β-sheet	Donor	Acceptor	$\lvert^{h3}J_{NC'}\rvert$ (Hz)	σ $\lvert^{h3}J_{NC'}\rvert$ (Hz)	Donor	Acceptor	$\lvert^{h3}J_{NC'}\rvert$ (Hz)	σ $\lvert^{h3}J_{NC'}\rvert$ (Hz)	Donor	Acceptor	$\lvert^{h3}J_{NC'}\rvert$ (Hz)	σ $\lvert^{h3}J_{NC'}\rvert$ (Hz)
1	β1-β2	707	724	0.60	0.0074	113	130	0.76	0.020	116	133	0.87	0.015
2	β1-β2	724	708	Peak overlap		130	114	0.53	0.051	133	117	0.59	0.024
3	β1-β2	710	722	0.70	0.0077	116	128	0.65	0.027	119	131	Peak overlap	
4	β1-β2	722	710	0.50	0.019	128	116	Peak overlap		131	119	0.46	0.020
5	β1-β2	712	720	No HNCO peak		118	126	0.53	0.056	121	129	0.57	0.014
6	β1-β2	719	713	Peak overlap		125	118	0.66	0.026	128	121	0.62	0.017
7	β2-β3	723	735	H-bond peak present. but too weak to quantify		129	142	0.41	0.029	132	145	0.42	0.019
8	β2-β3	735	723	Peak overlap		142	129	0.70	0.019	145	132	0.69	0.027
9	β2-β3	725	734	0.71	0.010	131	140	0.48	0.032	134	143	0.61	0.036
10	β2-β3	733	726	-	-	140	132	0.96	0.021	143	135	1.0	0.011
11	β2-β3	728	731	0.61	0.012	134	138	-	-	137	141	-	-
12	β3-β4	732	745	0.59	0.009	139	154	0.60	0.034	142	157	Peak overlap	
13	β3-β4	745	732	0.62	0.019	154	139	No HNCO peak		157	142	0.68	0.015
14	β3-β4	734	743	0.69	0.039	141	152	0.65	0.049	144	155	0.58	0.019
15	β3-β4	743	734	0.49	0.029	152	141	-	-	155	144	0.72	0.021
16	β3-β4	736	741	0.63	0.033	143	150	0.75	0.033	146	153	0.49	0.024
17	β3-β4	741	736	No H-Bond orientation		150	143	0.47	0.052	153	146	0.48	0.015
18	β3-β4	No equivalent		-	-	148	145	No H-bond orientation		151	148	No HNCO peak	
19	β5-β1	713	749	No HNCO peak		119	158	Peak overlap		122	161	-	-
20	β5-β1	751	711	-	-	160	117	0.51	0.036	163	120	0.57	0.037
21	β5-β1	711	751	0.68	0.023	117	160	0.68	0.015	120	163	0.53	0.016
22	β5-β1	753	709	-	-	162	115	-	-	165	118	-	-
23	β5-β1	No equivalent		-	-	No equivalent		-	-	No equivalent		-	-
24	β5-β1	No equivalent		-	-	No equivalent		-	-	No equivalent		-	-

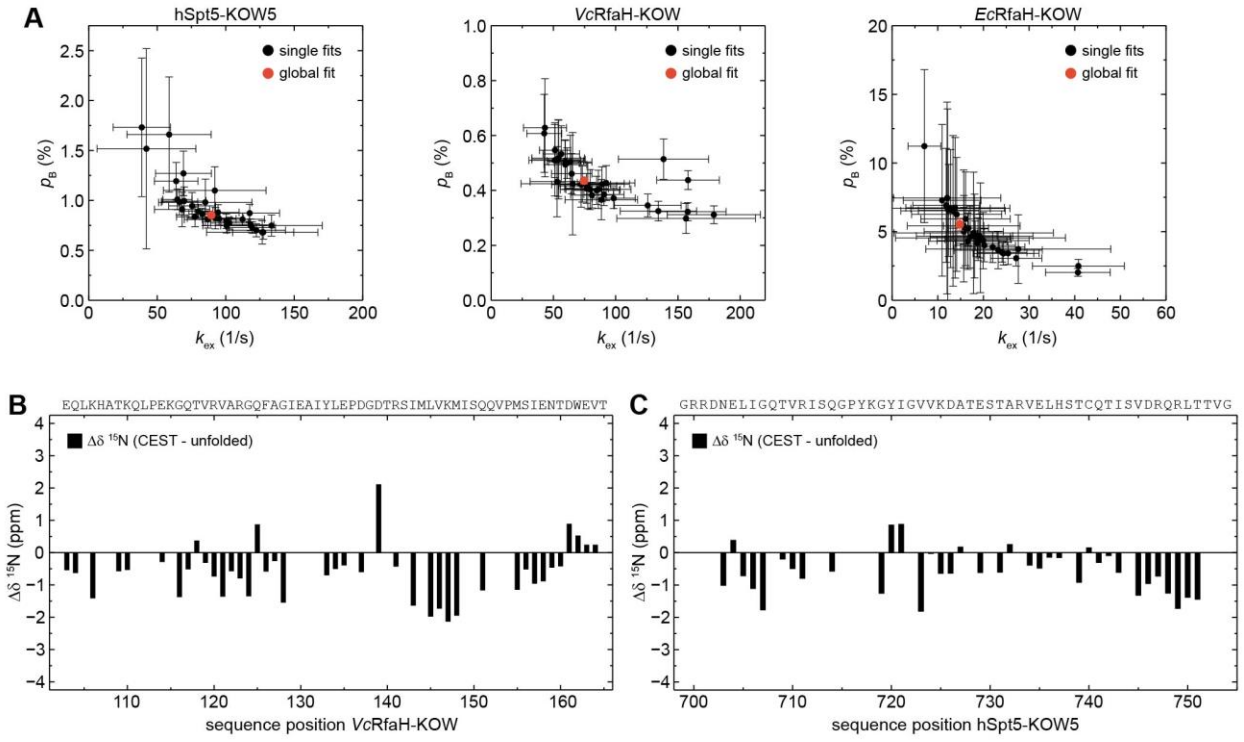

Figure 5 – Figure supplement 1. Extended CEST analysis of hSpt5-KOW5, *Vc*RfaH-KOW, or *Ec*RfaH-KOW. (**A**) Plots of k_{ex} vs. the population of the minor species (p_B) obtained from individual fits (black symbols) or a global fit (red symbol) of the CEST profiles of (left) hSpt5-KOW5, (middle) *Vc*RfaH-KOW, and (right) *Ec*RfaH-KOW. Error bars represent the standard deviation of the fits. (**B, C**) Sequence dependent difference between the ^{15}N backbone amide chemical shifts of the CEST minor species of (**B**) *Vc*RfaH-KOW and (**C**) hSpt5-KOW5 and the corresponding theoretical random coil value. The sequence of the two protein constructs is given above the diagrams.

Figure 5 – Figure supplement 2. Exchange parameters derived from global fitting of the CEST experiments to a two-state exchange model. Standard deviations result from data fitting.

Parameter	**hSpt5-KOW5**	***Vc*RfaH-KOW**	***Ec*RfaH-KOW**
p_A (%)	99.15 ± 0.02	99.57 ± 0.01	94.47 ± 0.46
p_B (%)	0.85 ± 0.02	0.43 ± 0.01	5.53 ± 0.46
k_{AB} (s^{-1})	0.76 ± 0.03	0.32 ± 0.02	0.82 ± 0.10
k_{BA} (s^{-1})	88.62 ± 3.12	74.24 ± 3.17	13.98 ± 1.24
k_{ex} (s^{-1})	89.38 ± 3.15	74.57 ± 3.18	14.80 ± 1.31
τ_A (s)	1.31 ± 0.05	3.08 ± 0.15	1.22 ± 0.15
τ_B (ms)	11.28 ± 0.40	13.47 ± 0.57	71.52 ± 6.33
ΔG (kJ/mol)	11.81 ± 0.05	13.48 ± 0.07	7.18 ± 0.21

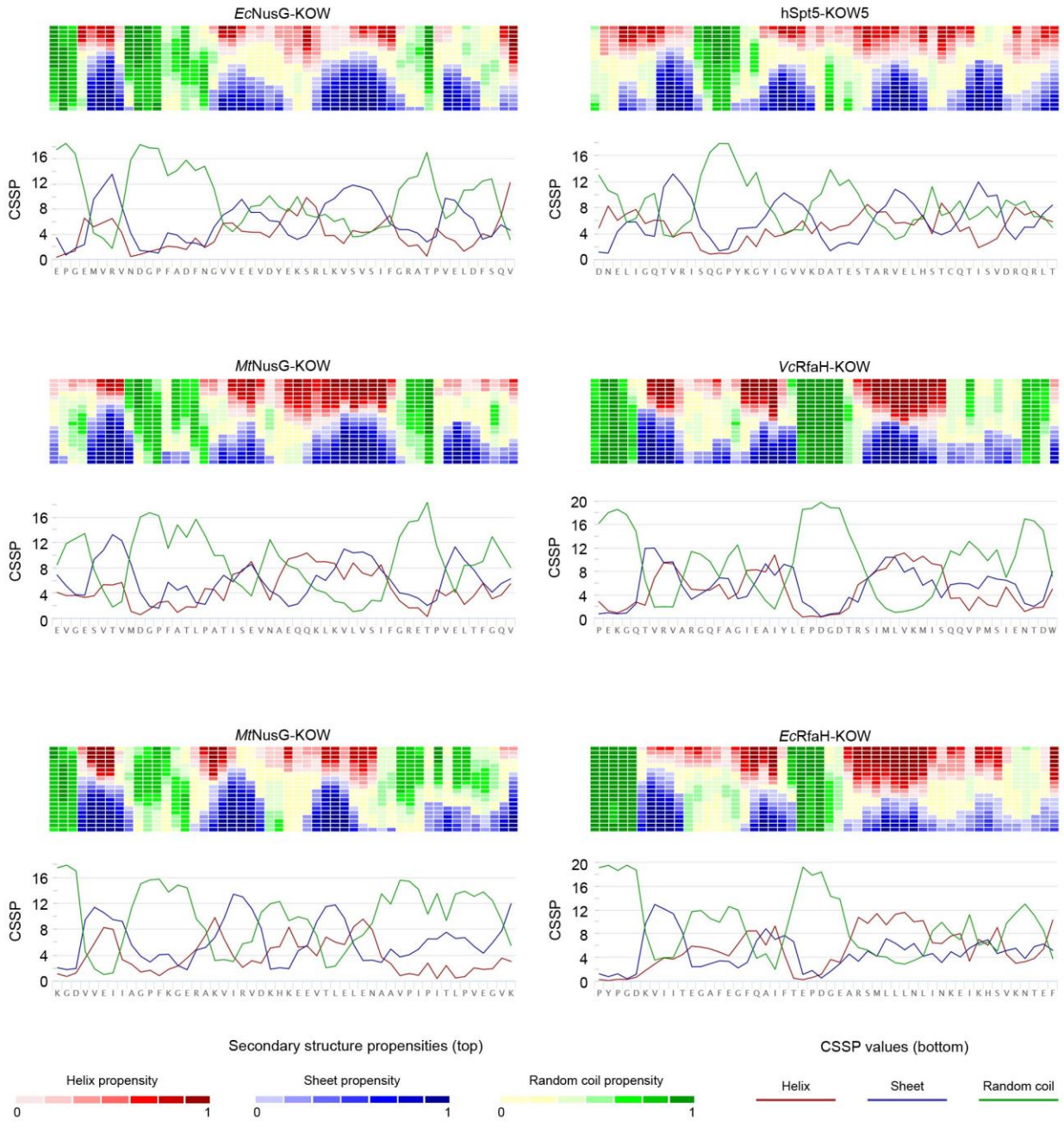

1332

1333 **Figure 5 – Figure supplement 3.** Secondary structure prediction for the six KOW domains used

1334 in this study by Net-CSSP (Kim et al., 2009). The contact-dependent secondary structure

1335 propensity (CSSP) of each domain is plotted against die amino acid sequence (red: helices; blue:

1336 beta structures; green: random coil). The heat map above each graph displays the propensity of

each amino acid to adopt helical (red), beta (blue), or random coil (green) structures using a gradient from dark (high propensity) to light (low propensity) colors.

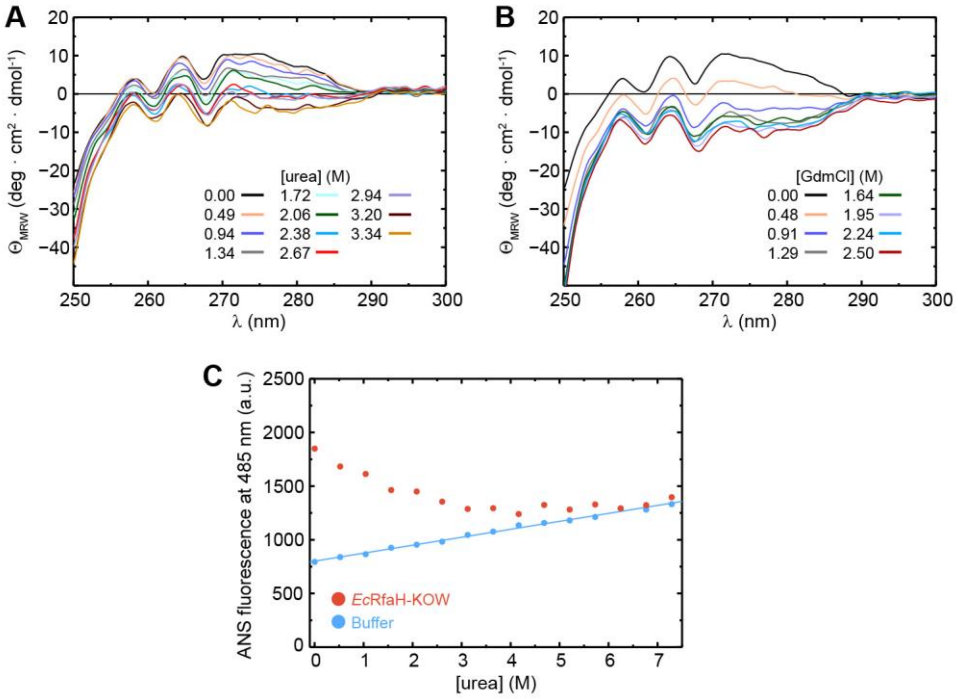

Figure 6 – Figure supplement 1. The intermediate state of *Ec*RfaH-KOW is no equilibrium MG. (**A, B**) Near-UV CD-spectra of *Ec*RfaH-KOW during a titration with (A) 10 M urea and (B) 8 M GdmCl. In both cases, the solution was buffered by 10 mM K-phosphate (pH 7.0). The denaturant concentrations at which the spectra were recorded are indicated. (**C**) ANS binding experiments. The graph shows the ANS fluorescence at 485 nm after over-night incubation of ANS in the presence (filled red circles) or absence (filled blue circles) of *Ec*RfaH-KOW at increasing urea concentrations. The system was buffered by 10 mM K-phosphate (pH 7.0).

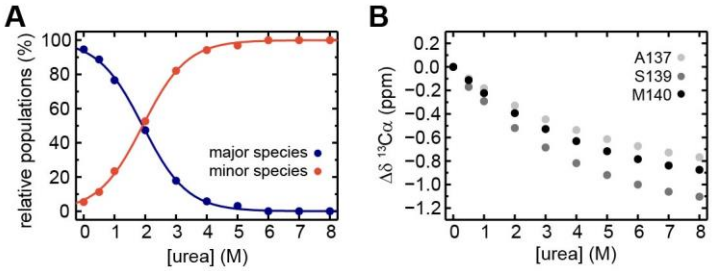

Figure 6 – Figure supplement 2. Extended analysis of the urea-induced denaturation of *Ec*RfaH-KOW with a three state-model. (**A**) Relative populations of the minor (filled red circles) and major (filled blue circles) species during the [^{1}H, ^{13}C]-ctHSQC-based urea denaturation of ^{1}H, ^{13}C-*Ec*RfaH-KOW. The populations at a certain urea concentration were calculated from the ratio of volumes of the Hα/Cα correlation peaks of S139 minor or major species signals, respectively, to the sum of both values. The curves were fitted to a two-state model to extract the parameters of the transition from the major species to the minor species. The minor species was treated as a single species neglecting the fact that it is actually an ensemble of at least two subspecies. Fitting to a three-state (or even higher-state) model with an increased number of fitting parameters would not be appropriate due to the limited number of data points. (**B)** Chemical shift changes of ^{13}Cα signals, $\Delta\delta^{13}$Cα, of A137, S139 and M140 in the [^{1}H, ^{13}C]-ctHSQC spectra during urea denaturation.

Source data

Figure 2 – Source data 1. Data for thermal denaturation experiments for all KOW domains.

Figure 3 – Source data 1. Data for chemical denaturation experiments for all KOW domains.

Figure 5 – Source data 1. CEST fits for *Ec*RfaH-KOW, *Vc*RfaH-KOW and hSpt5-KOW5.

Figure 5 – Source data 2. Experimentally determined chemical shift values of urea-denatured *Ec*RfaH-KOW and predicted random coil chemical shift values of *Vc*RfaH-KOW and hSpt5-KOW5.

Figure 6 – Source data 1. ANS binding by *Ec*RfaH-KOW during urea-based denaturation.

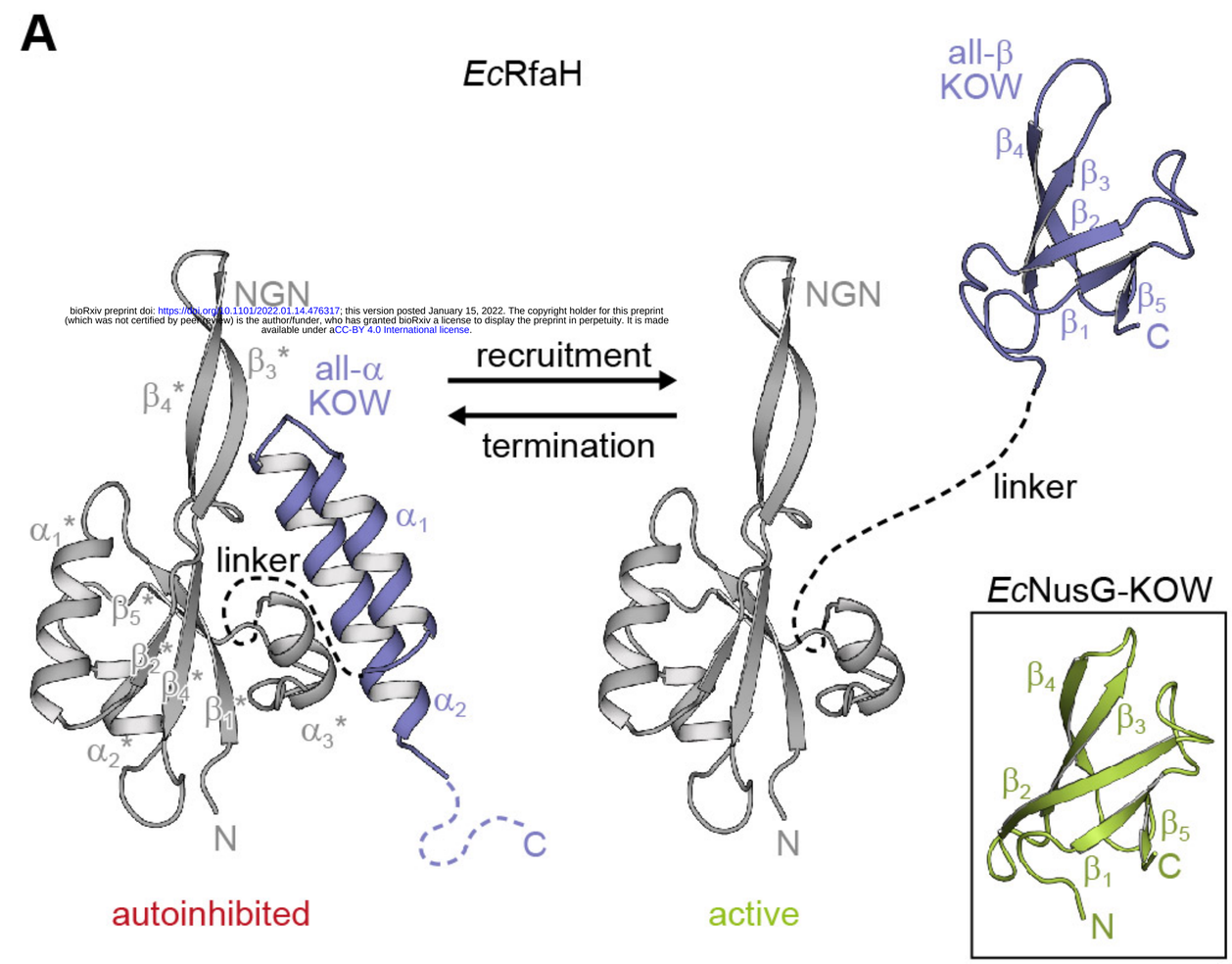

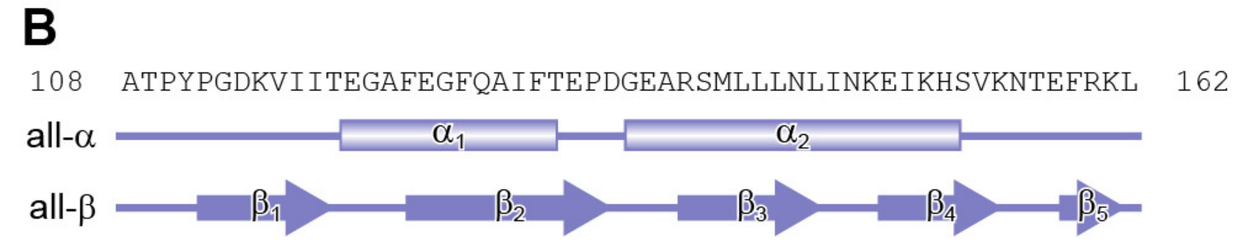

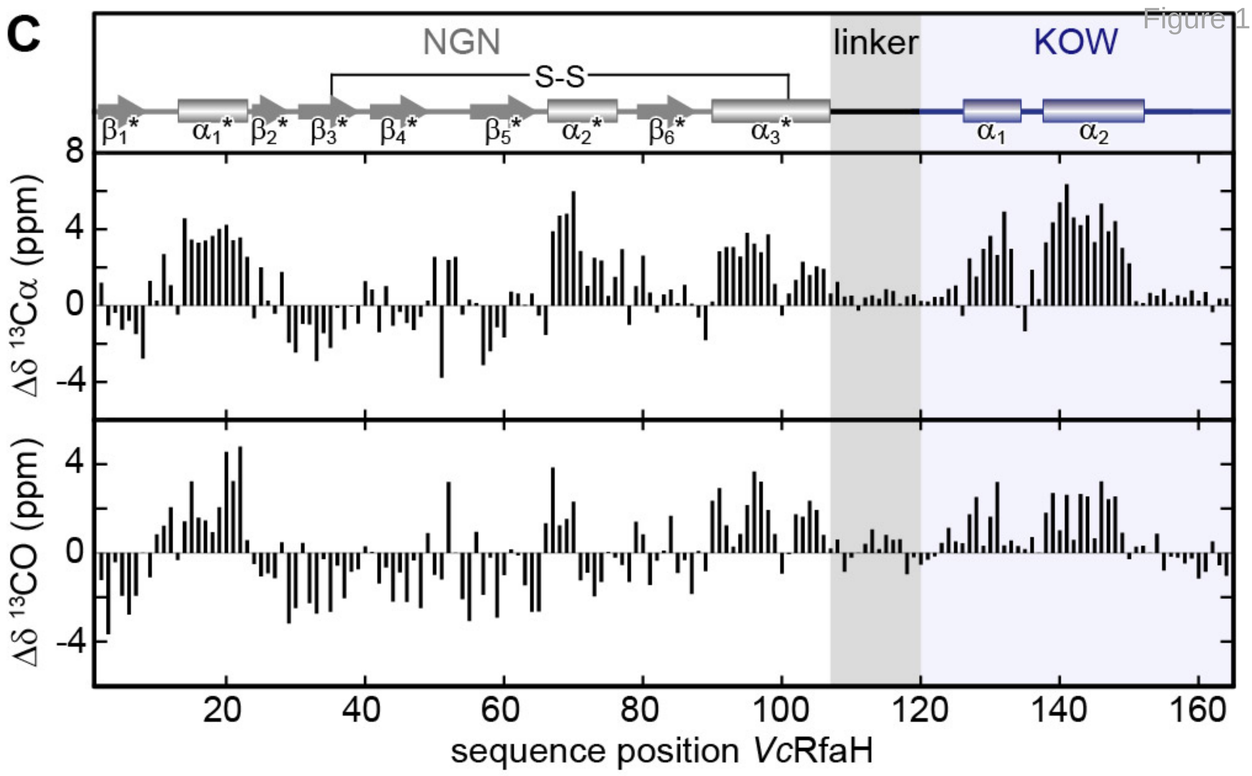

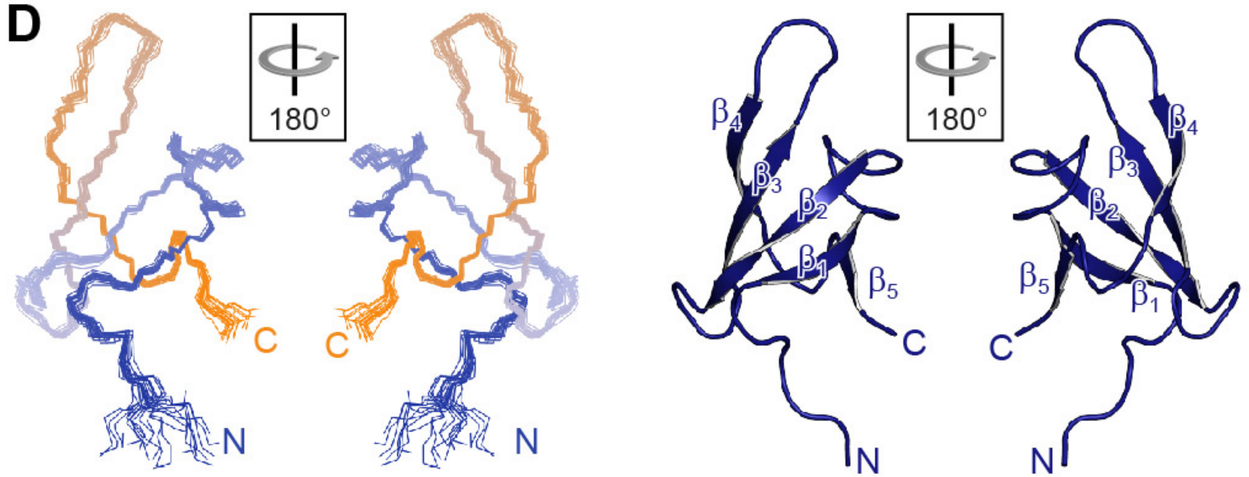

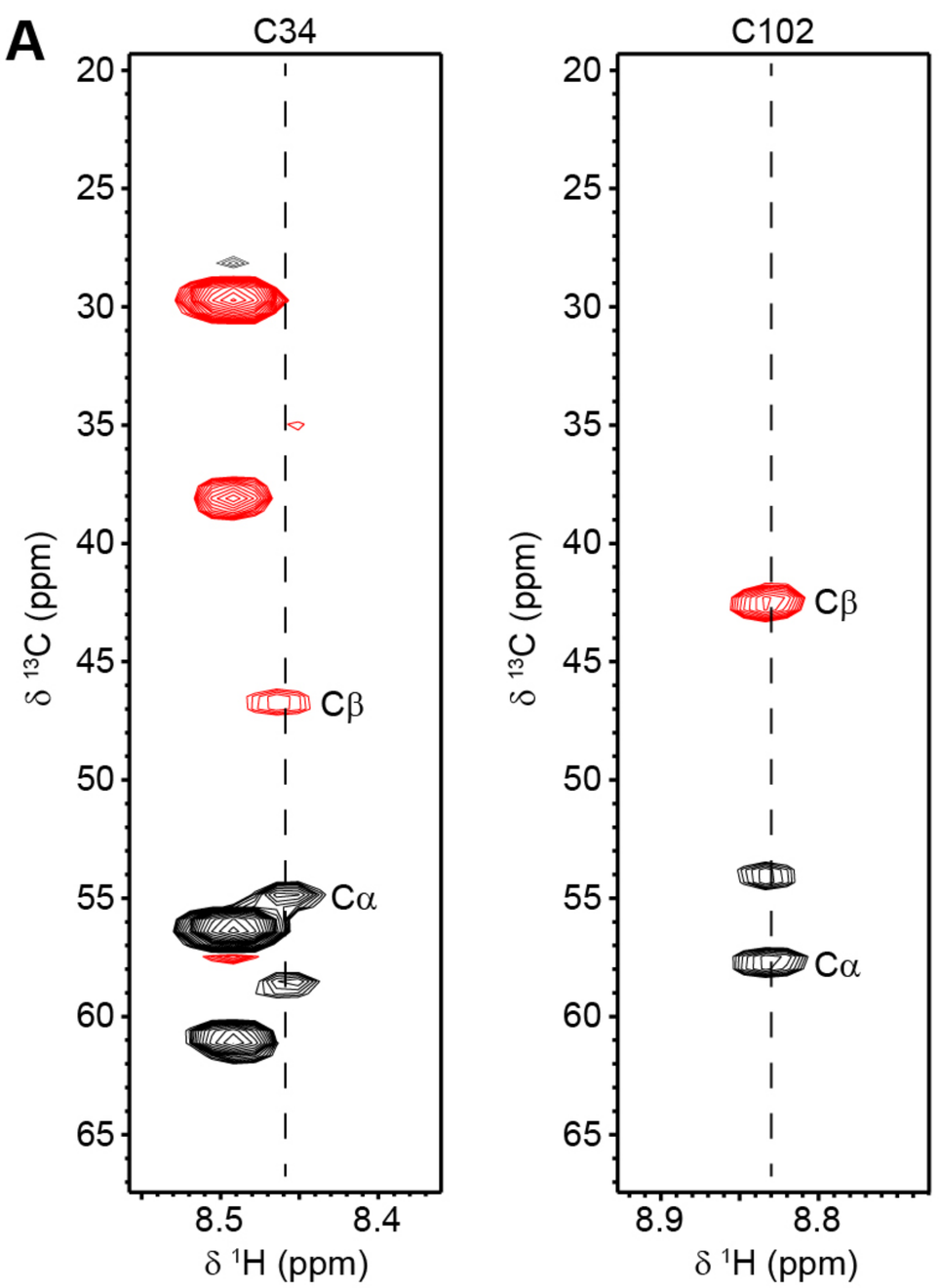

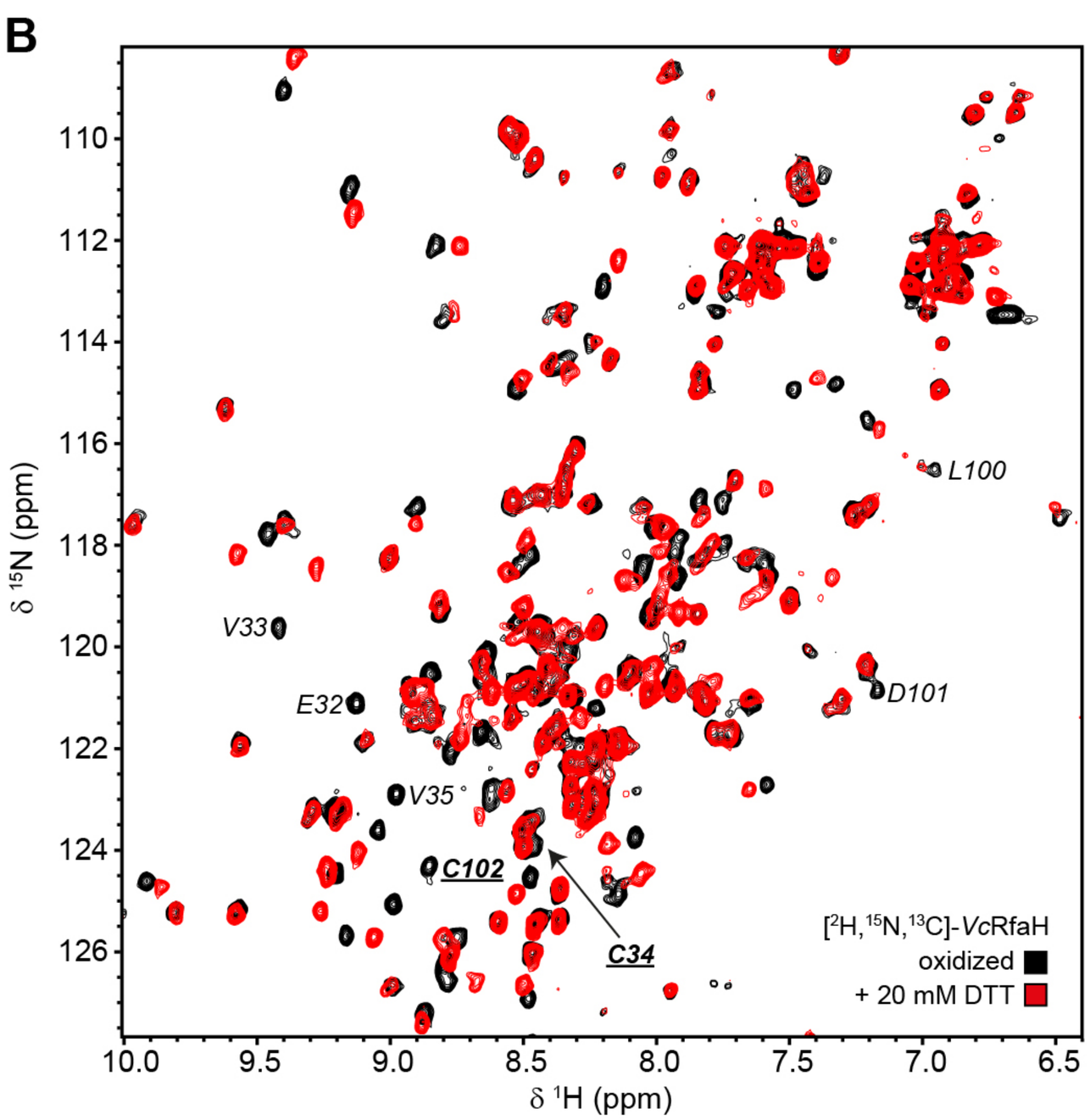

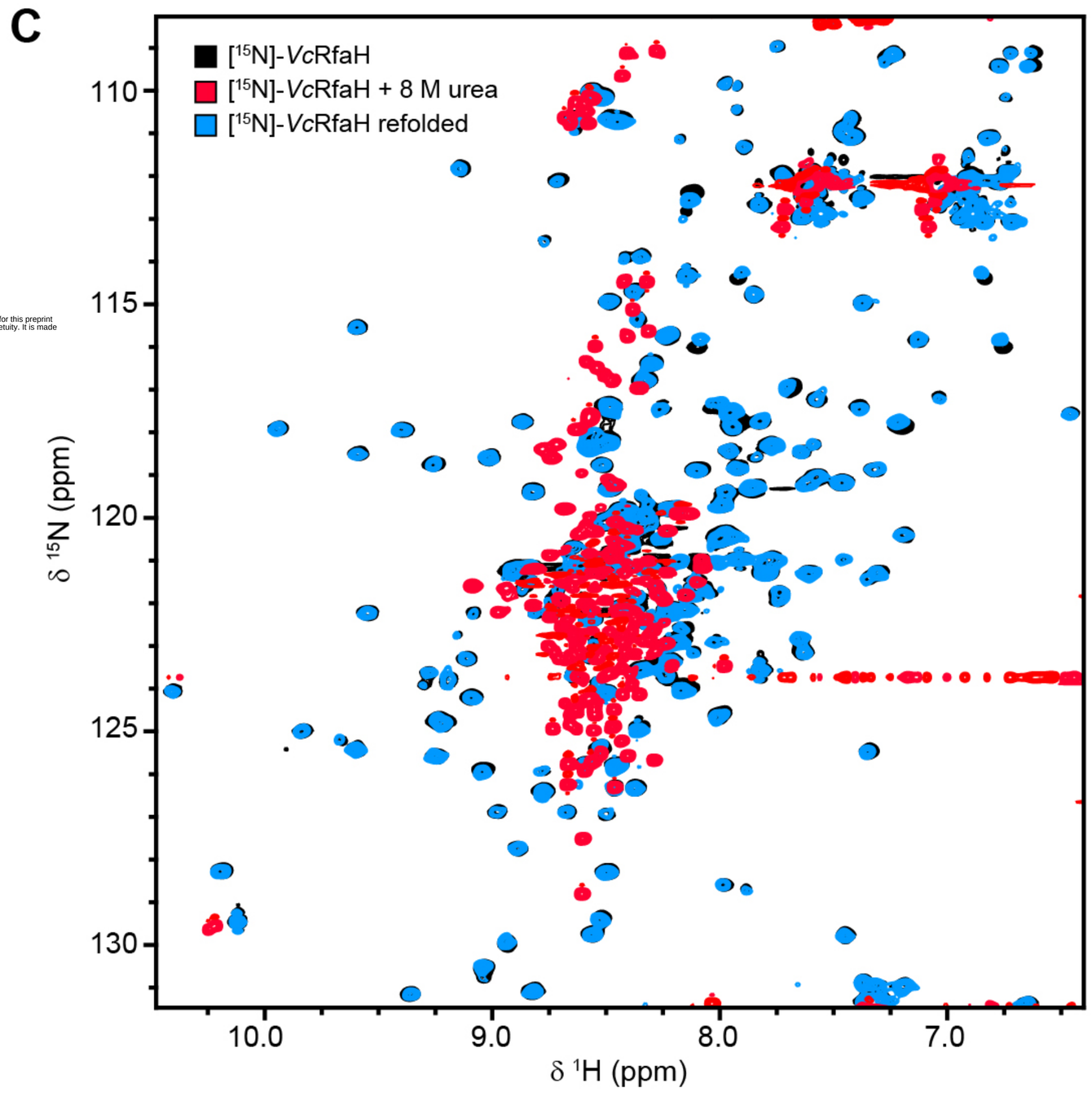

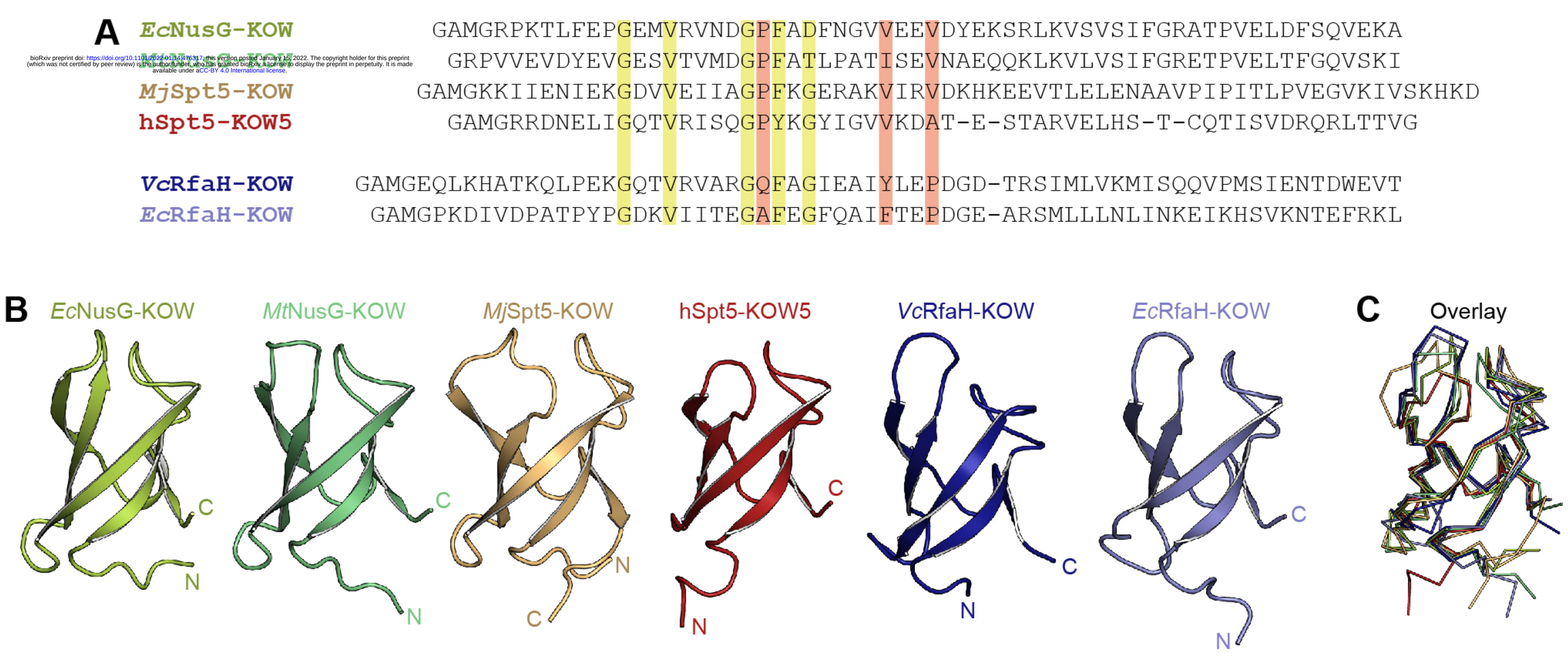

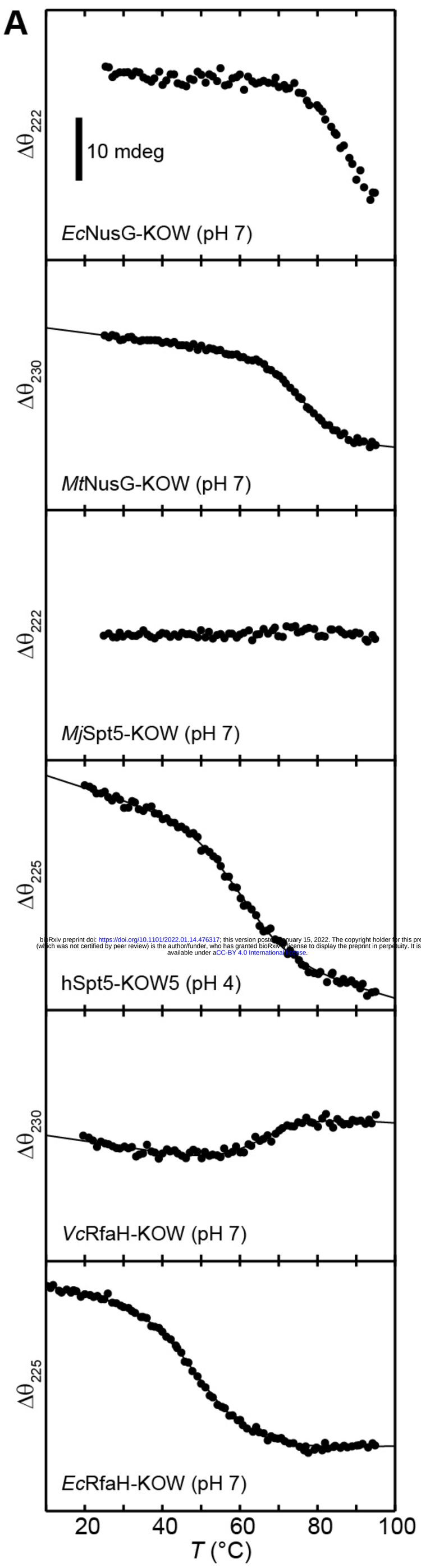

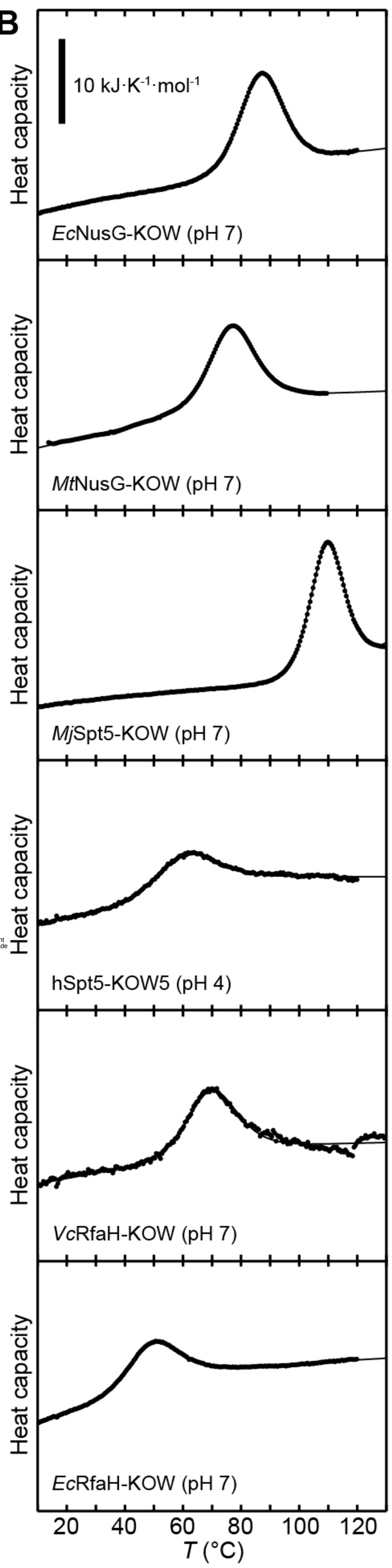

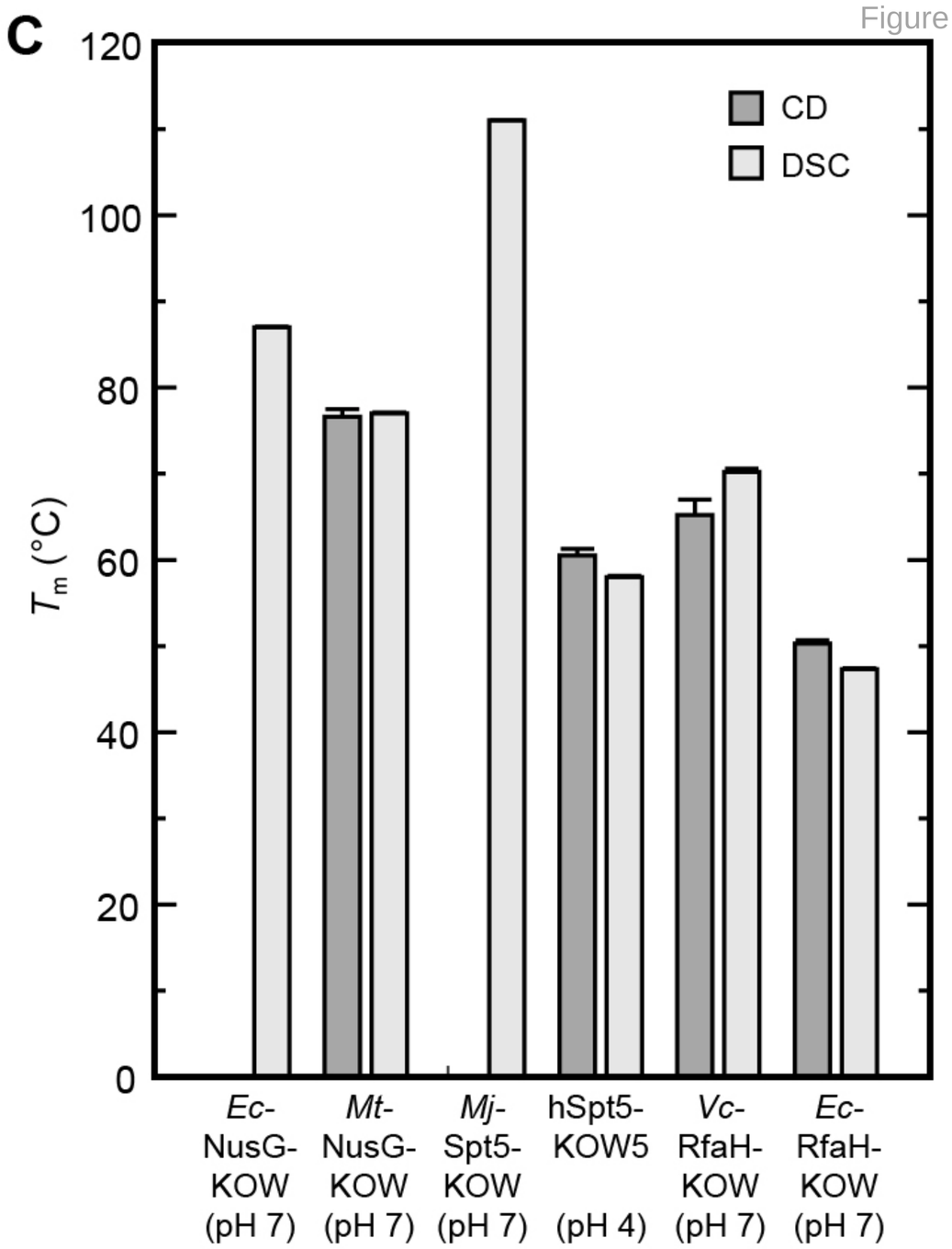

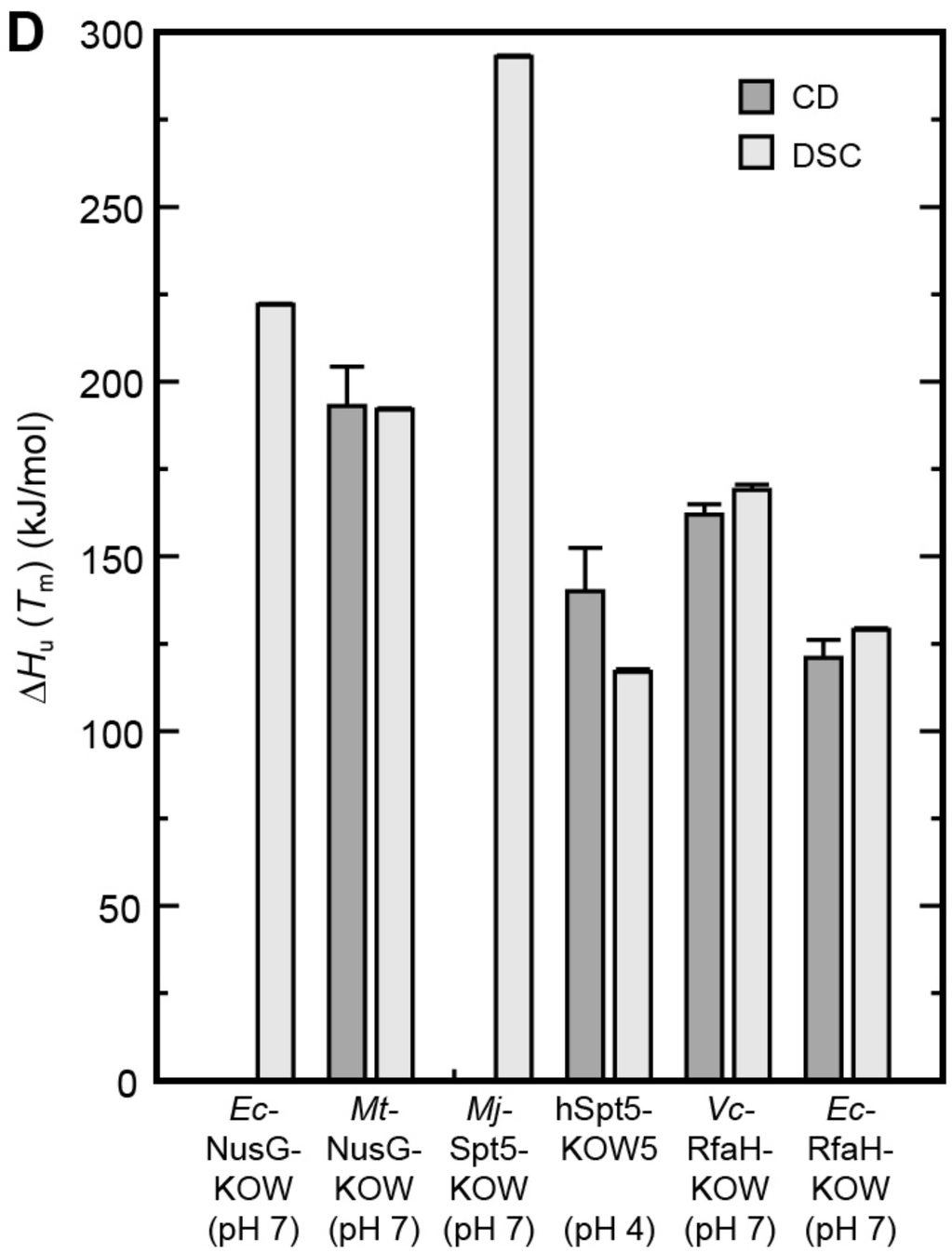

	K-acetate (pH 4.0)		K-phosphate (pH 7.0)	
***Ec*NusG-KOW**	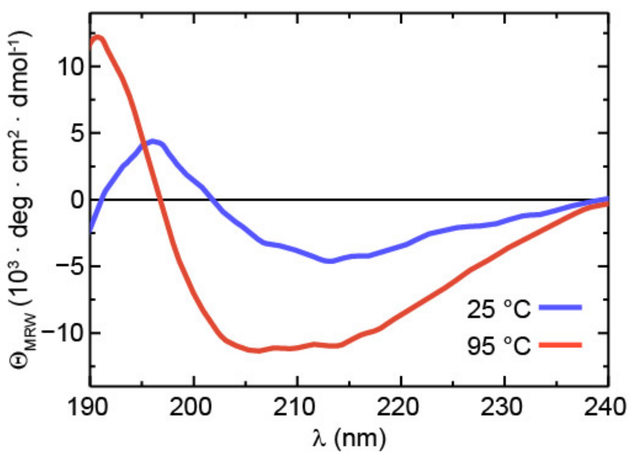	n.a.	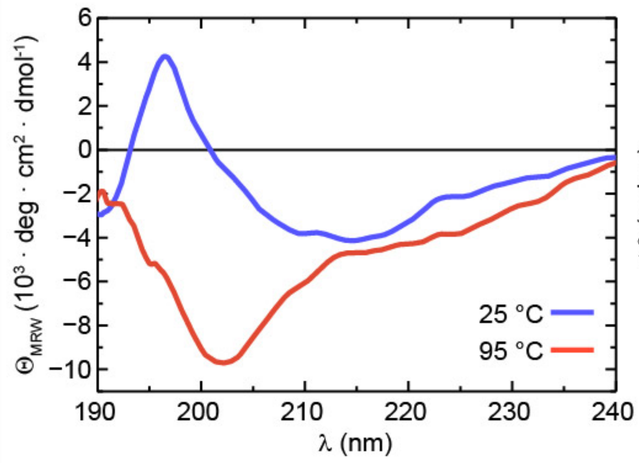	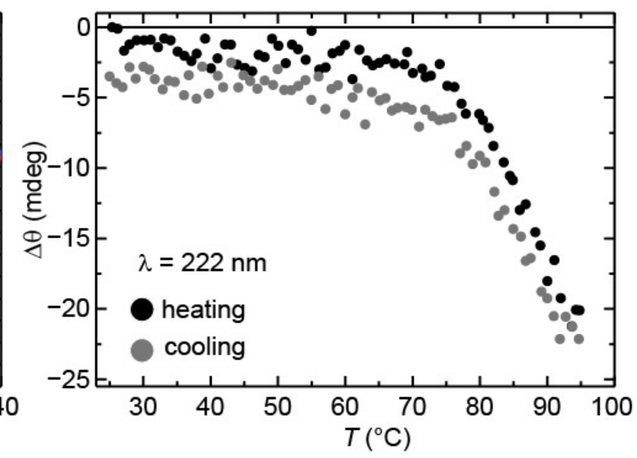
***Mf*NusG-KOW**	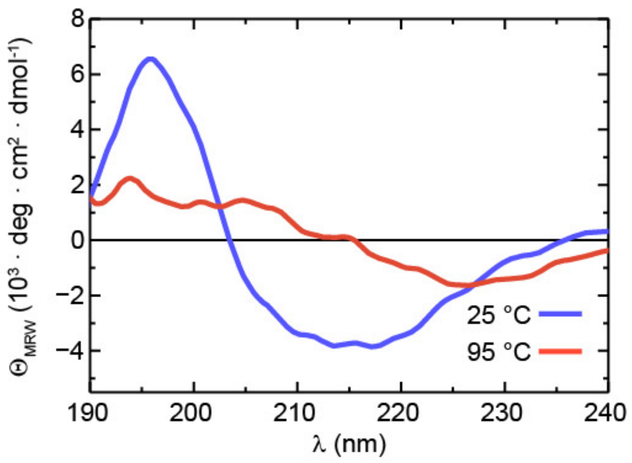	n.a.	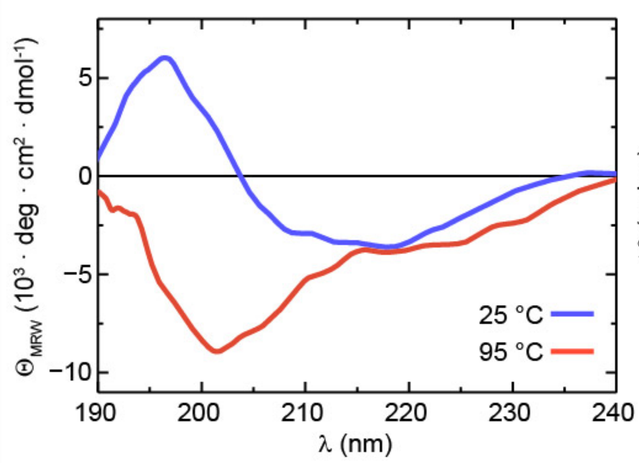	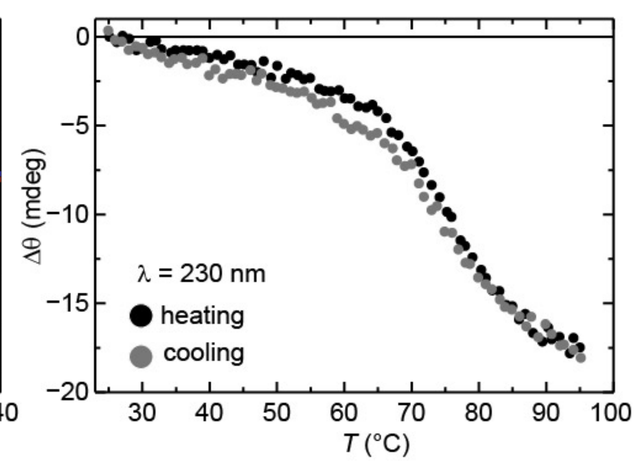
***Mj*Spt5-KOW**	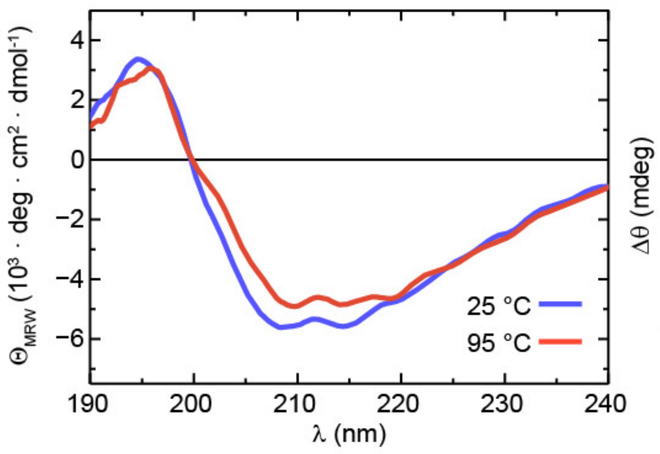	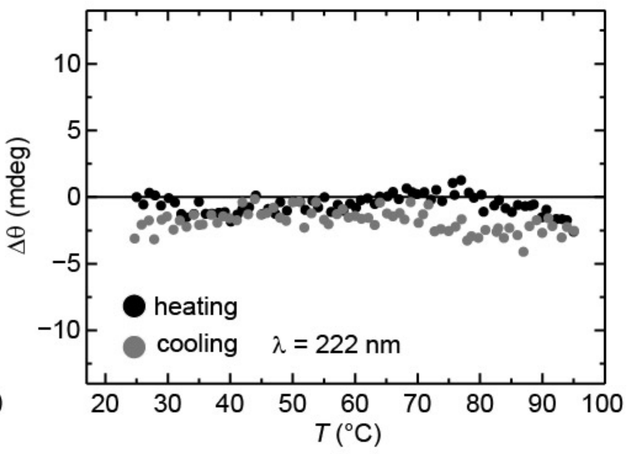	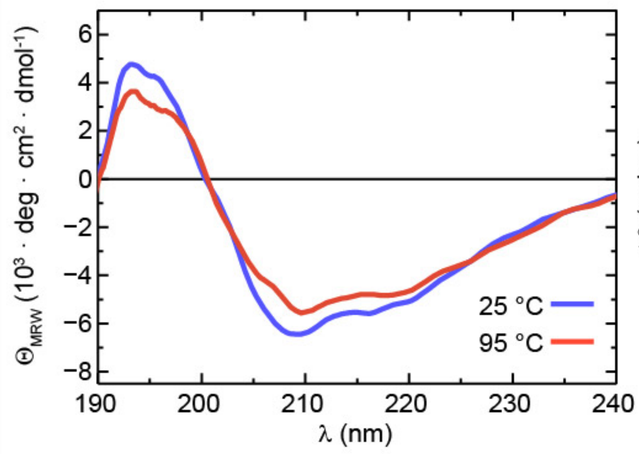	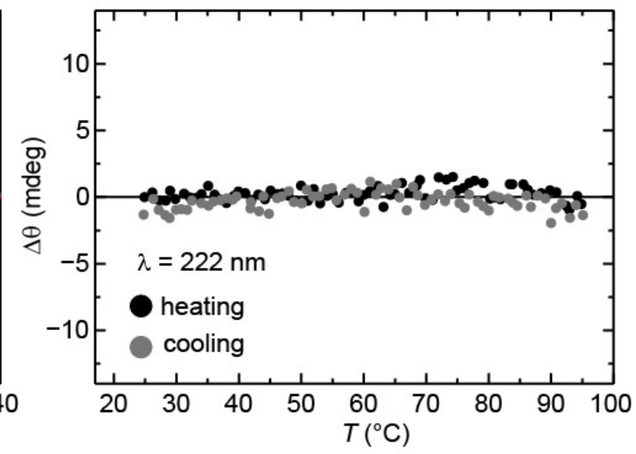
hSpt5-KOW5	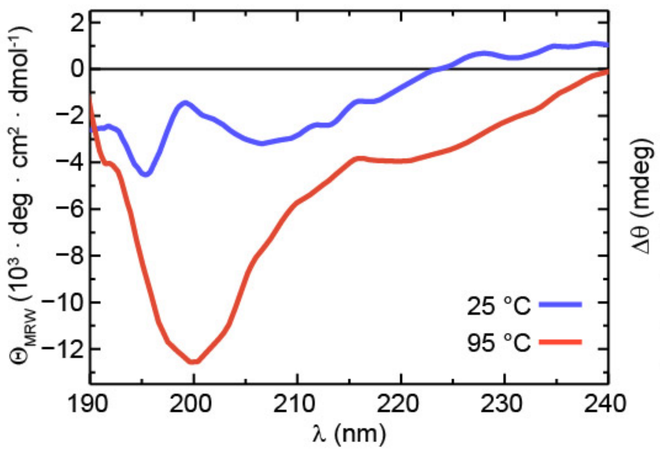	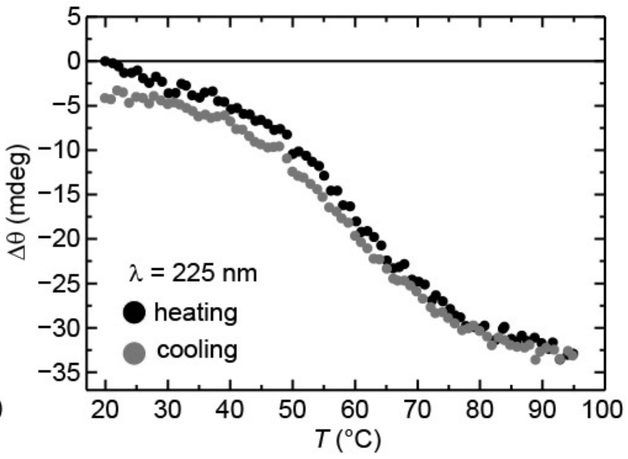	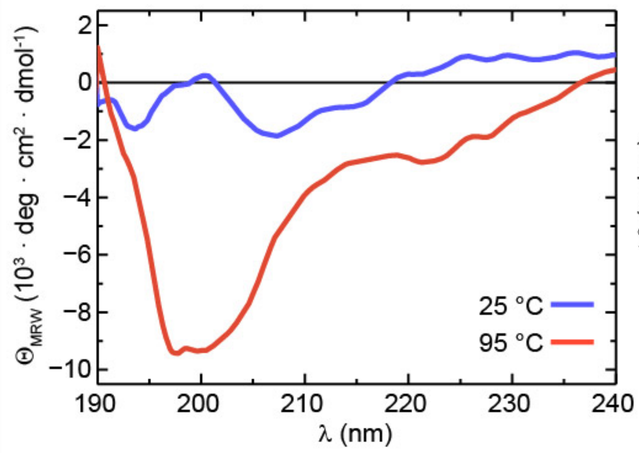	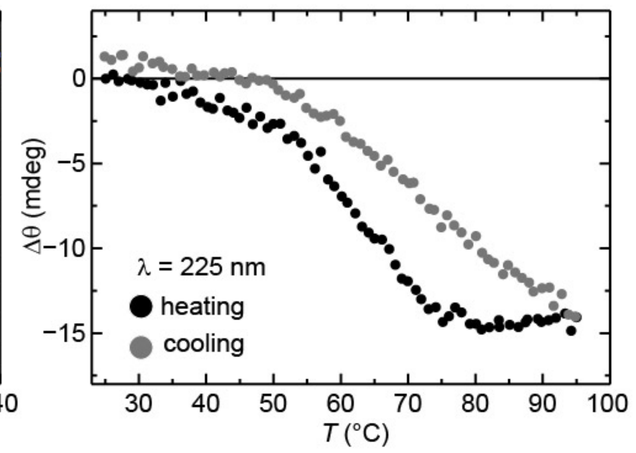
***Vc*RfaH-KOW**	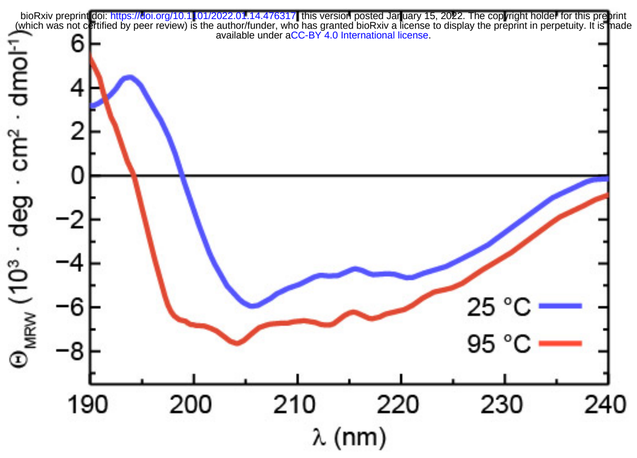	n.a.	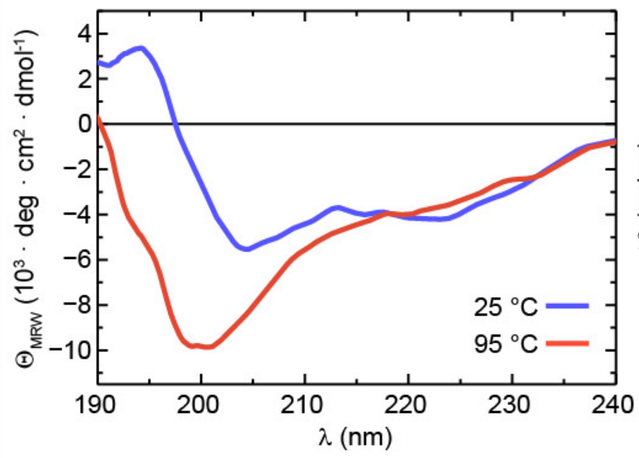	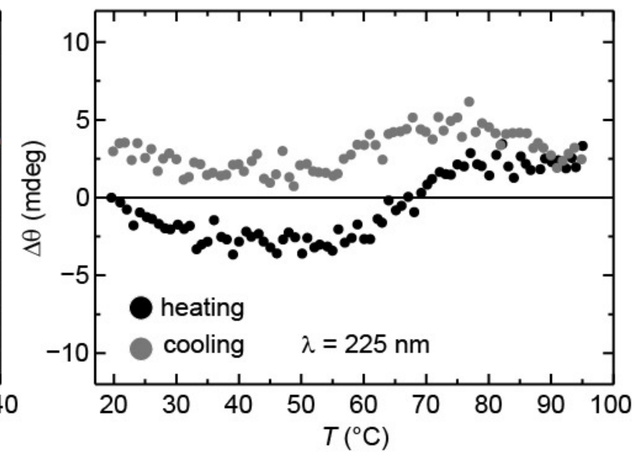
***Ec*RfaH-KOW**	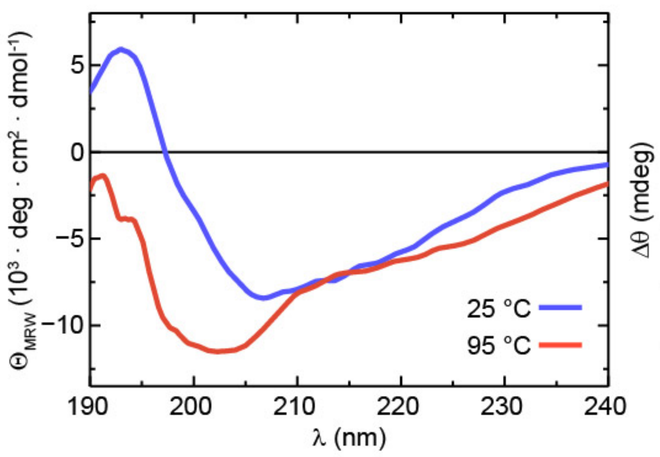	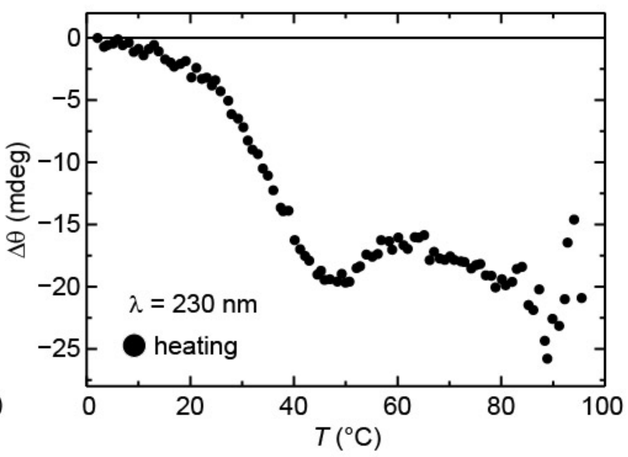	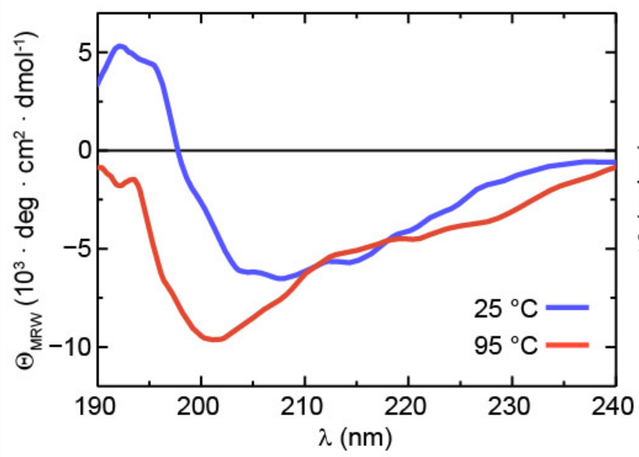	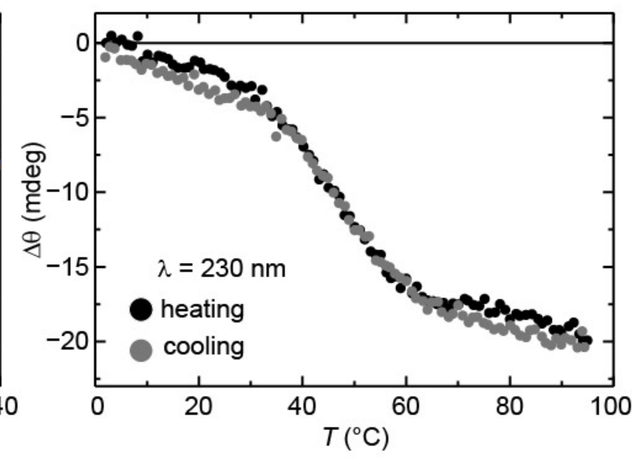

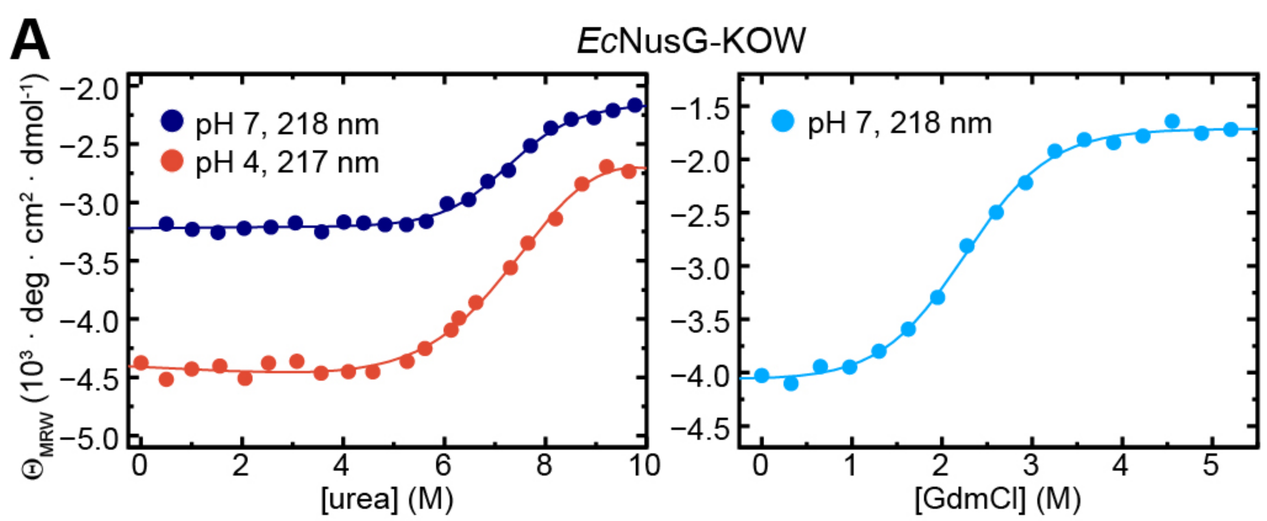

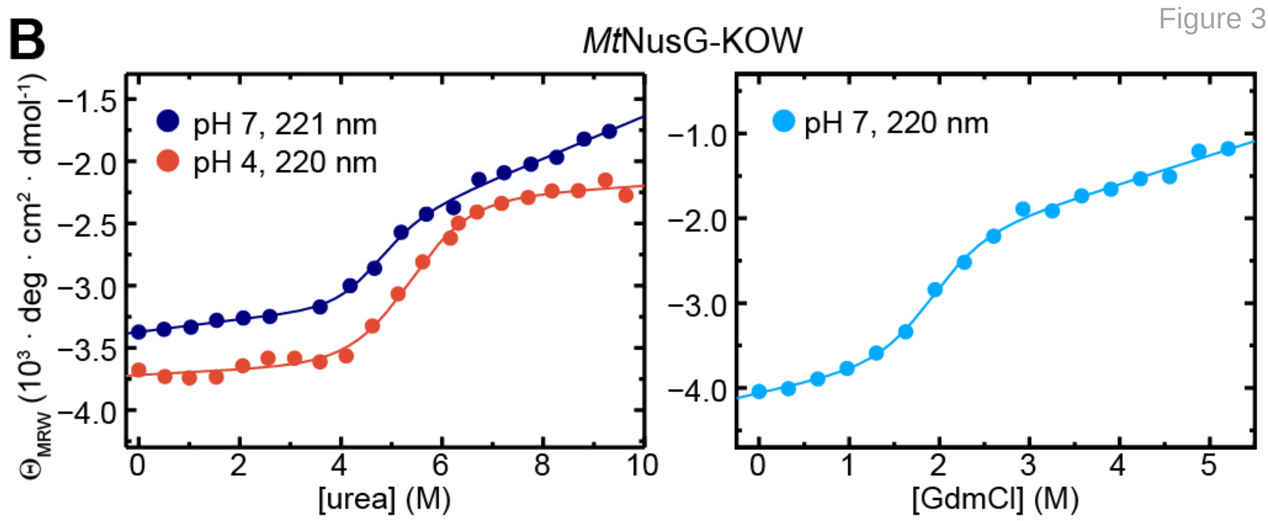

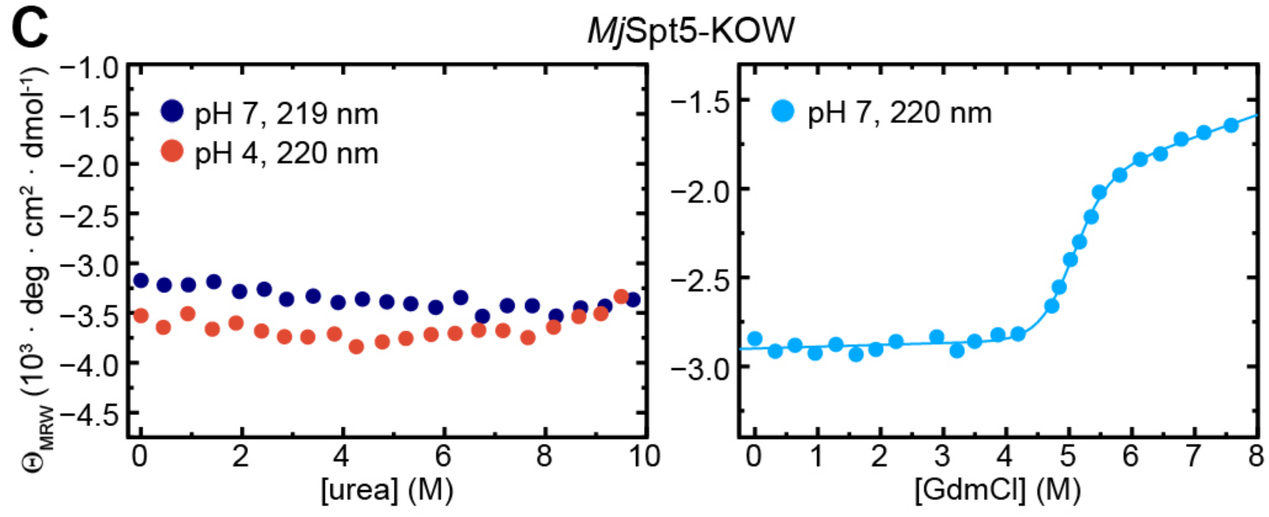

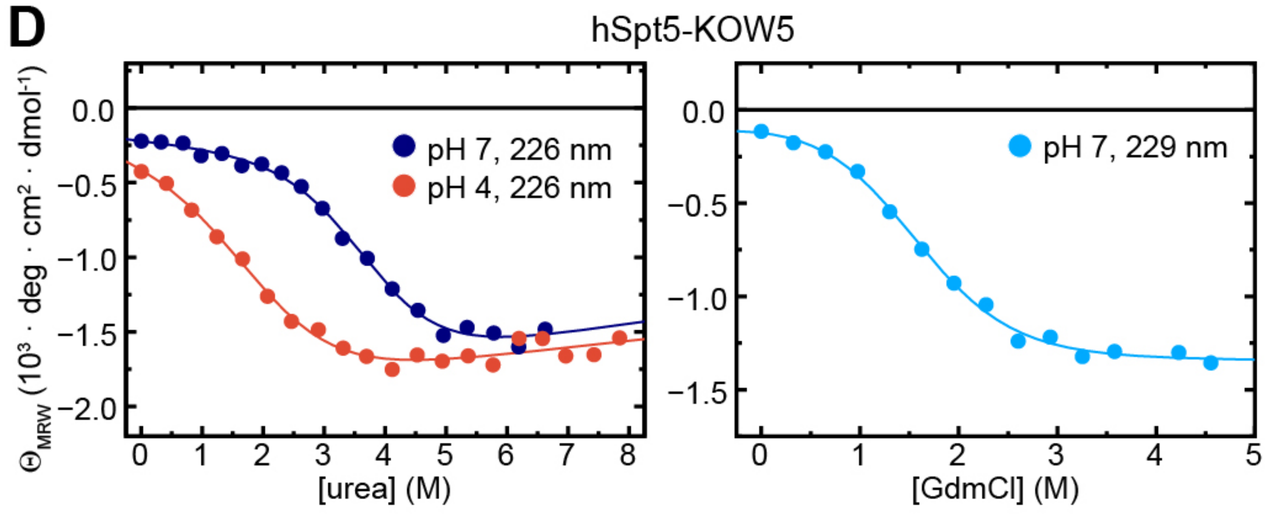

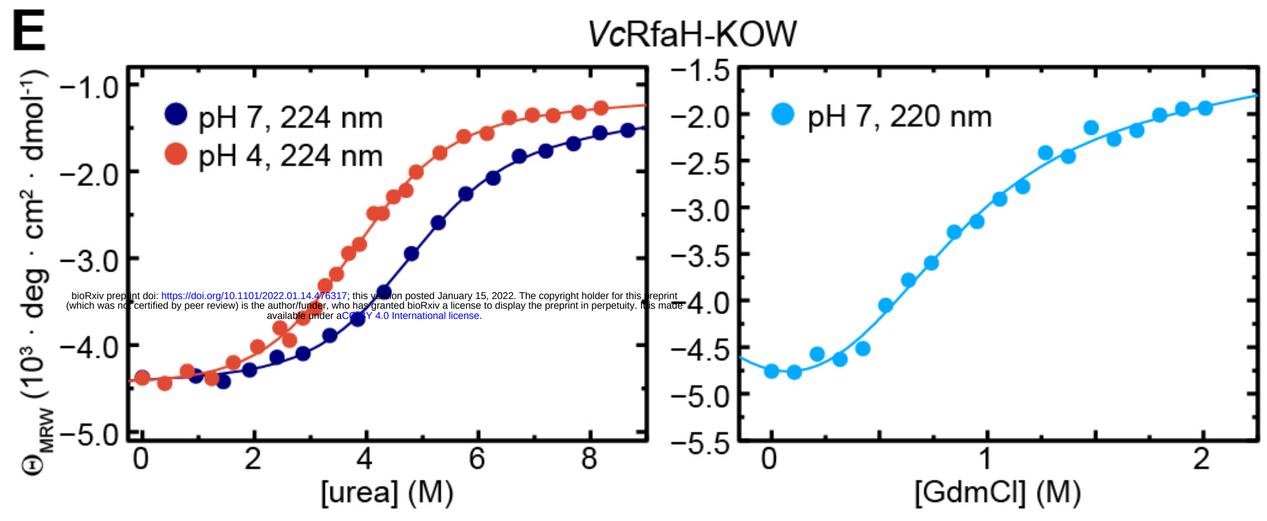

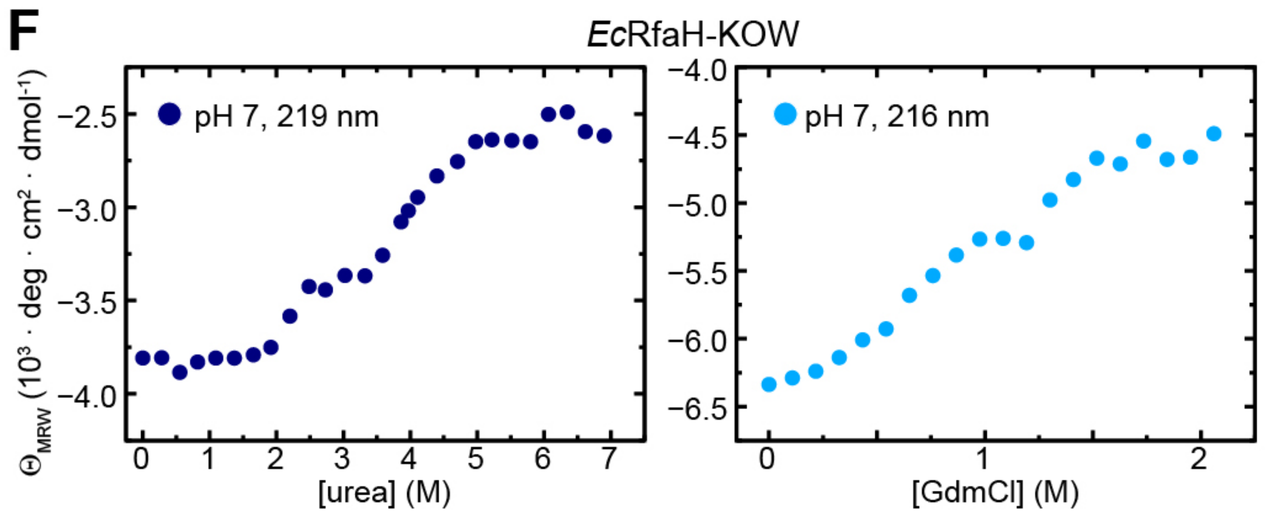

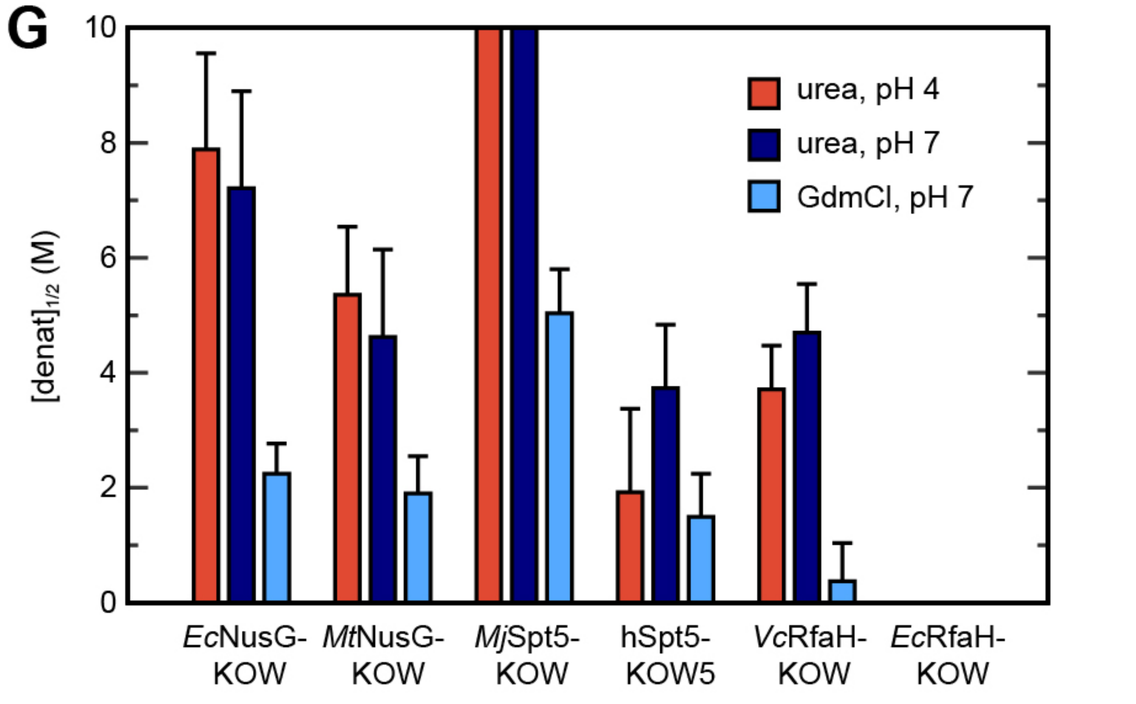

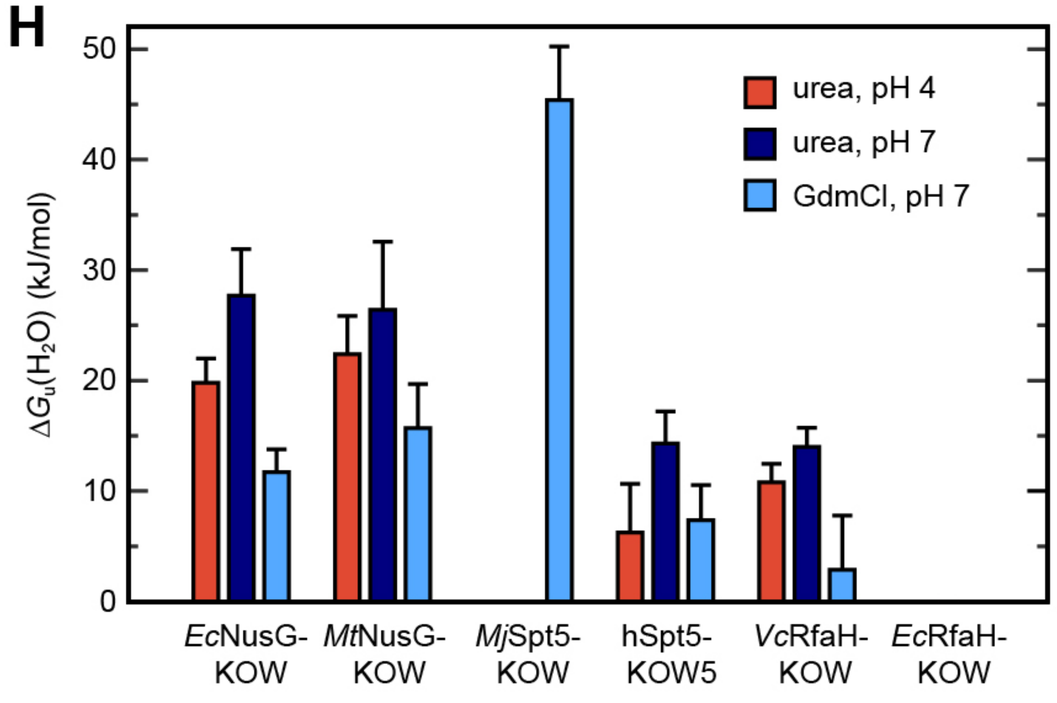

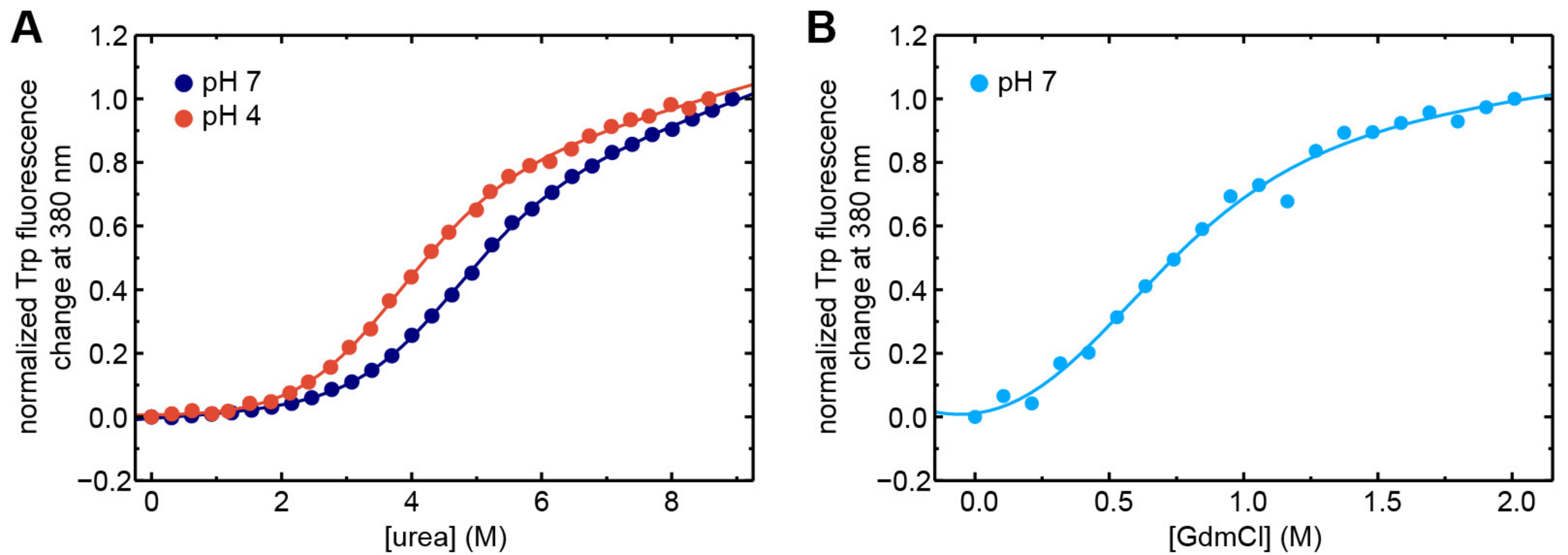
A
B
pH 7
pH 4
normalized Trp fluorescence change at 380 nm
[urea] (M)
[GdmCl] (M)
1.2
1.0
0.8
0.6
0.4
0.2
0.0
−0.2
0
2
4
6
8
0.0
0.5
1.0
1.5
2.0

	urea, K-phosphate (pH 7.0)	urea, K-acetate (pH 4.0)	GdmCl, K-phosphate (pH 7.0)
***Ec*NusG-KOW**	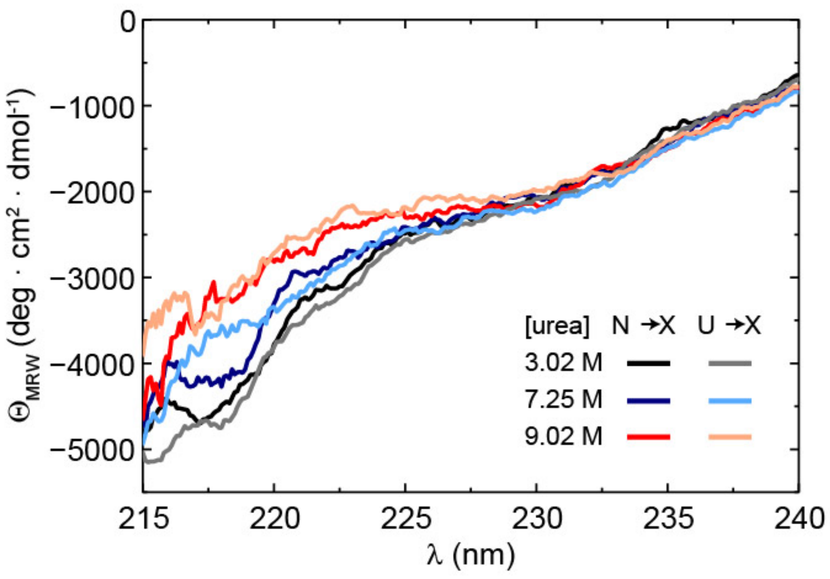	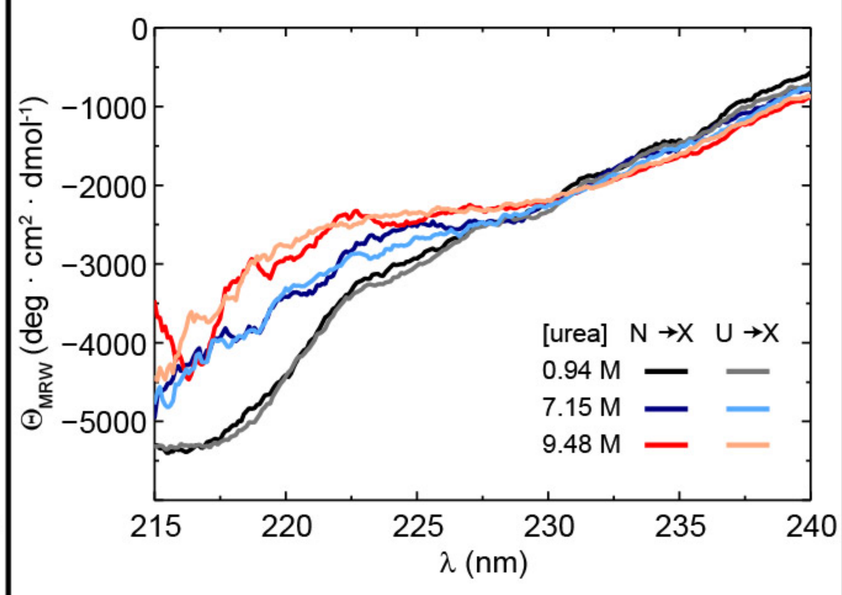	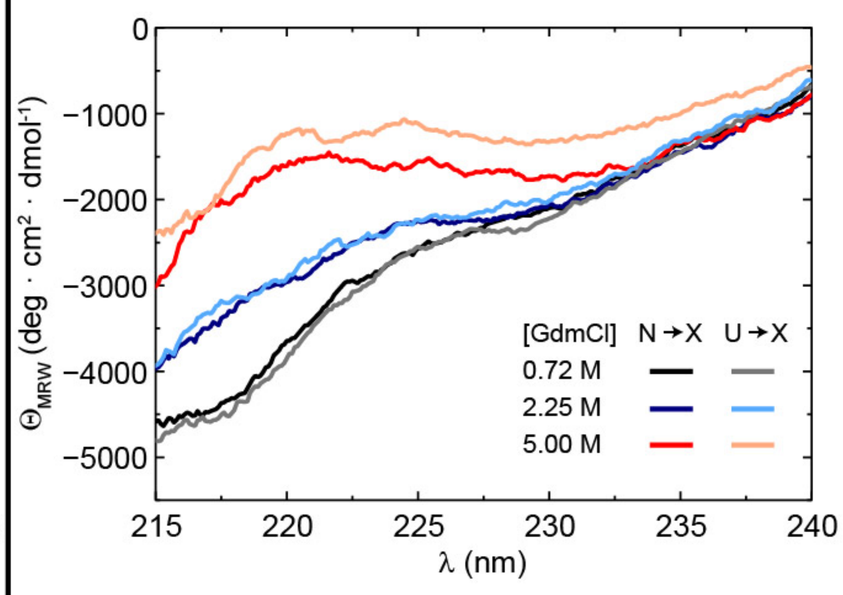
***Mf*NusG-KOW**	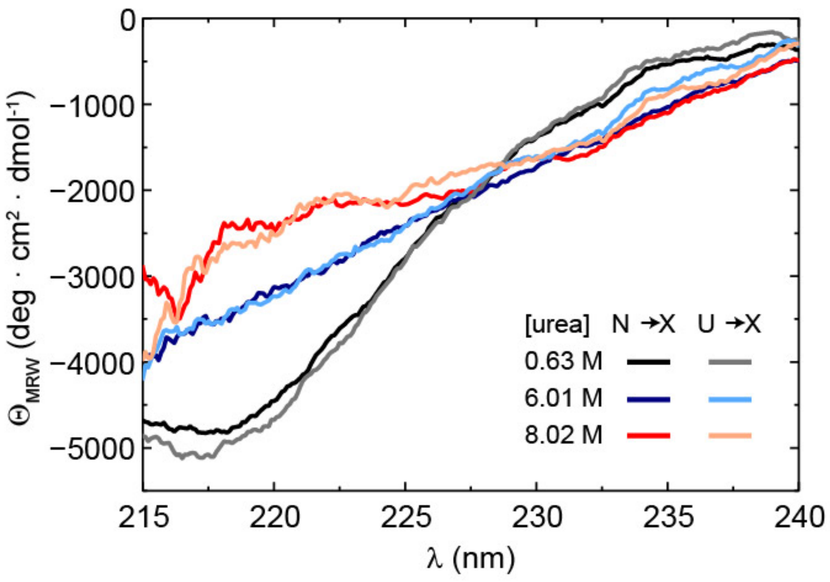	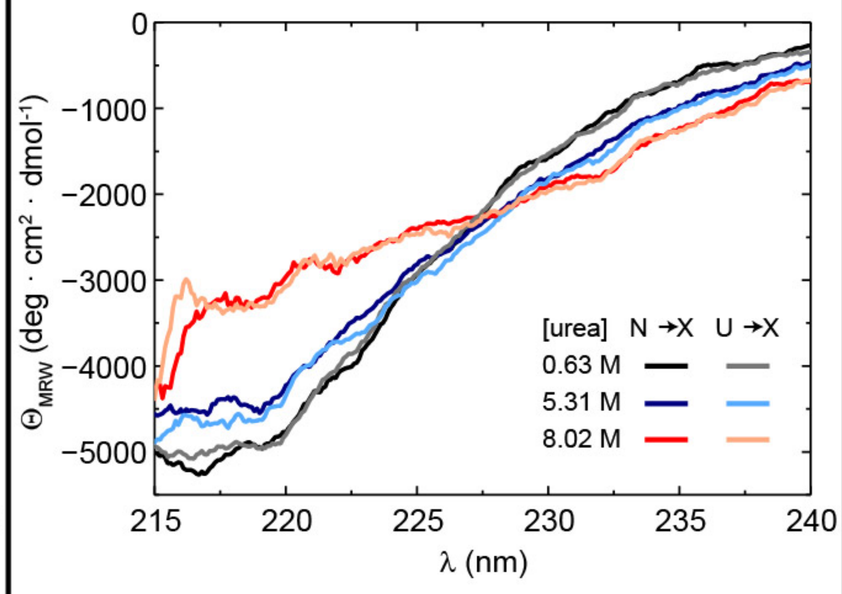	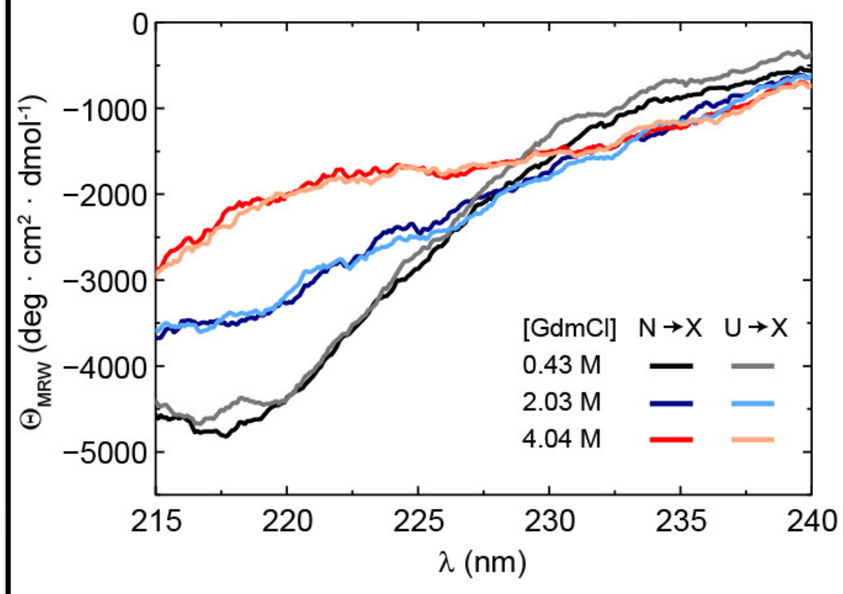
***Mj*Spt5-KOW**	n.a. (no unfolding possible)	n.a. (no unfolding possible)	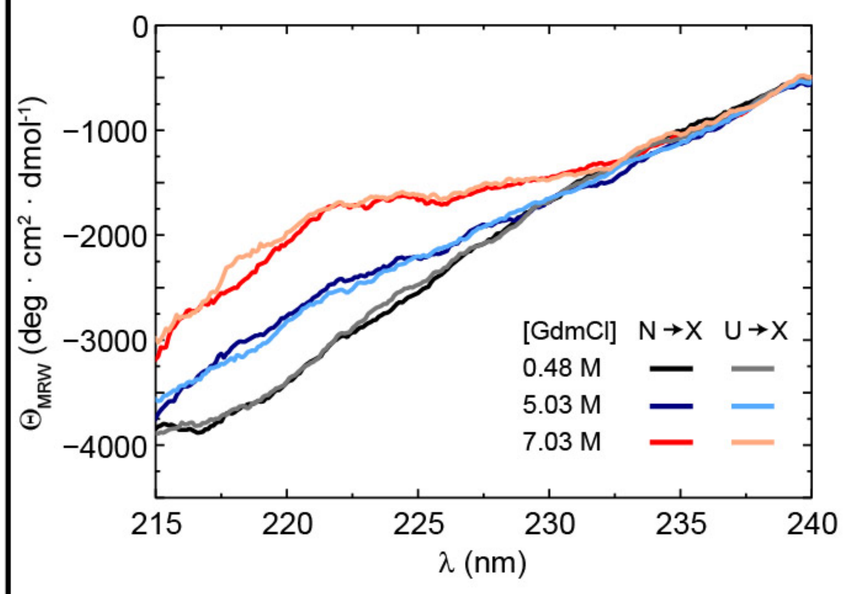
hSpt5-KOW5	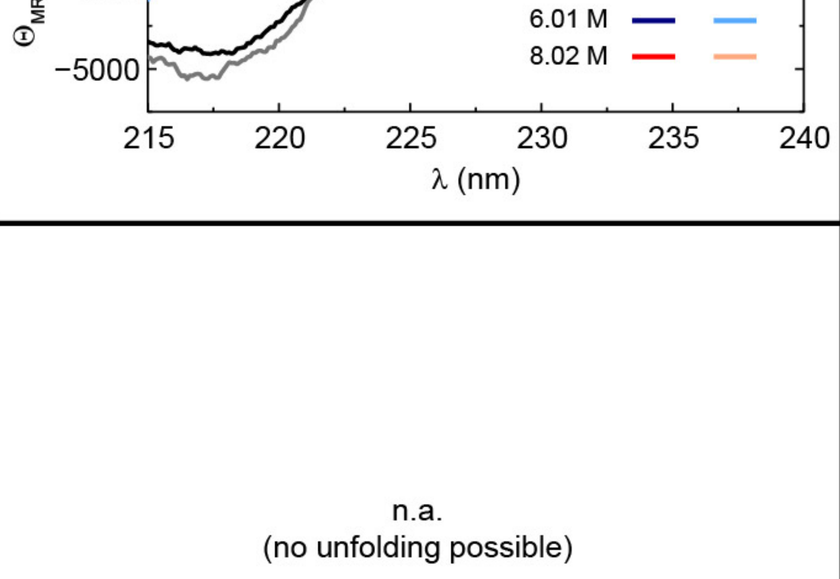	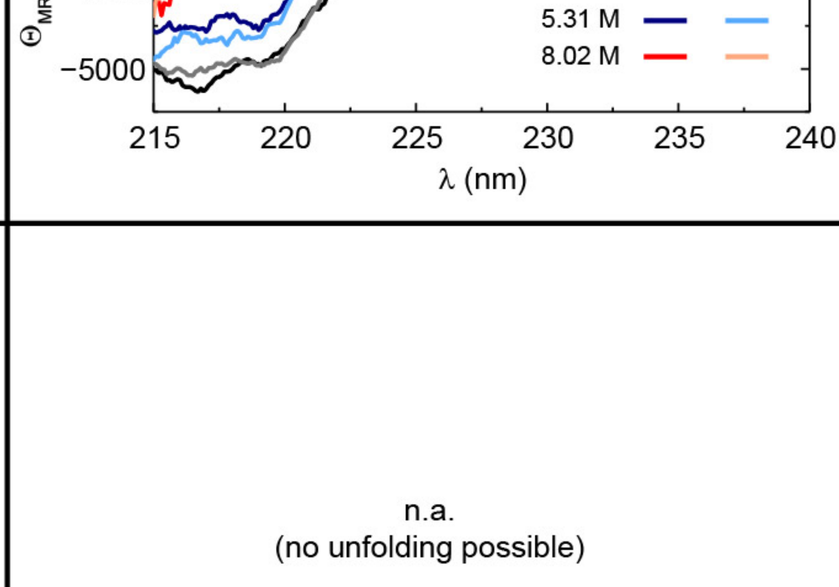	
***Vc*RfaH-KOW**	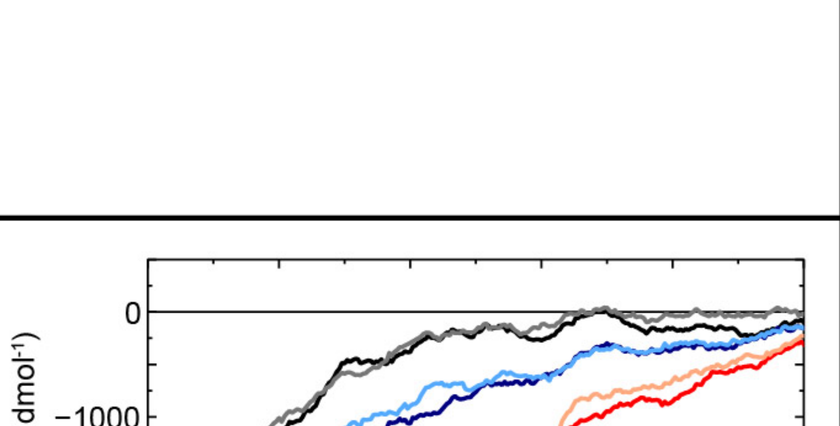	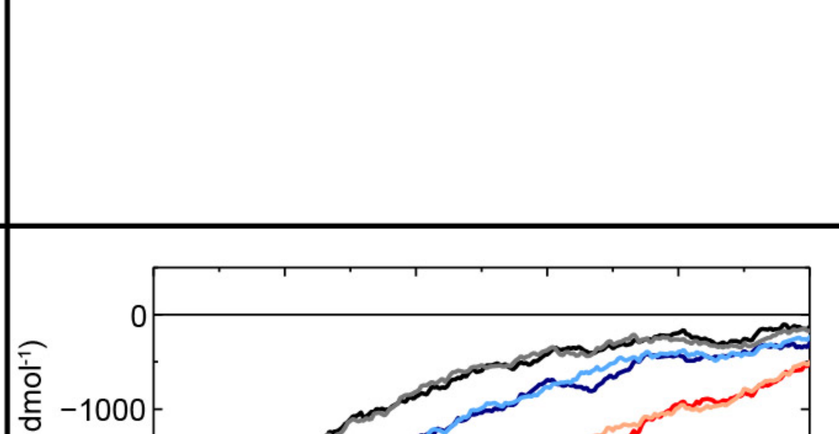	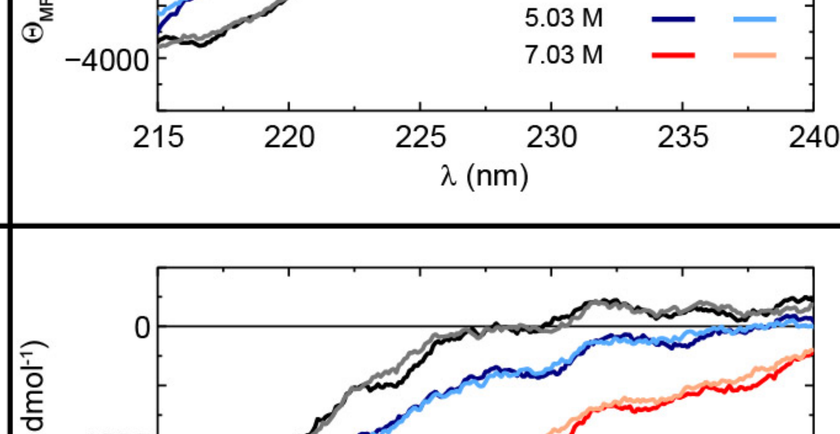
***Ec*RfaH-KOW**	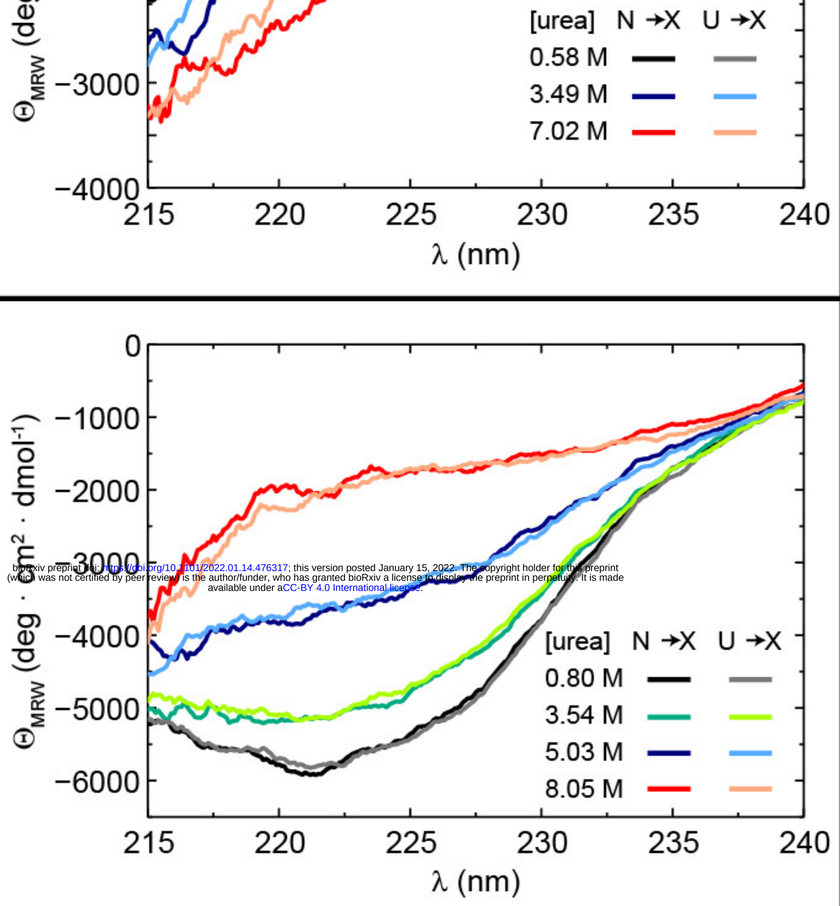	n.a. (native state aggregation)	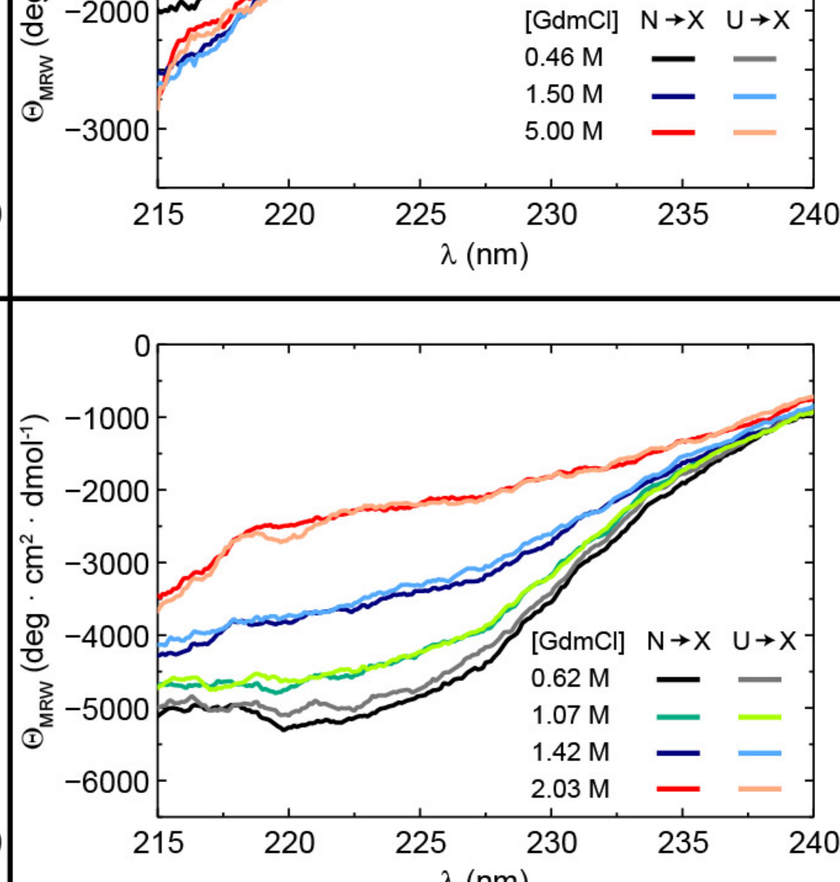

A

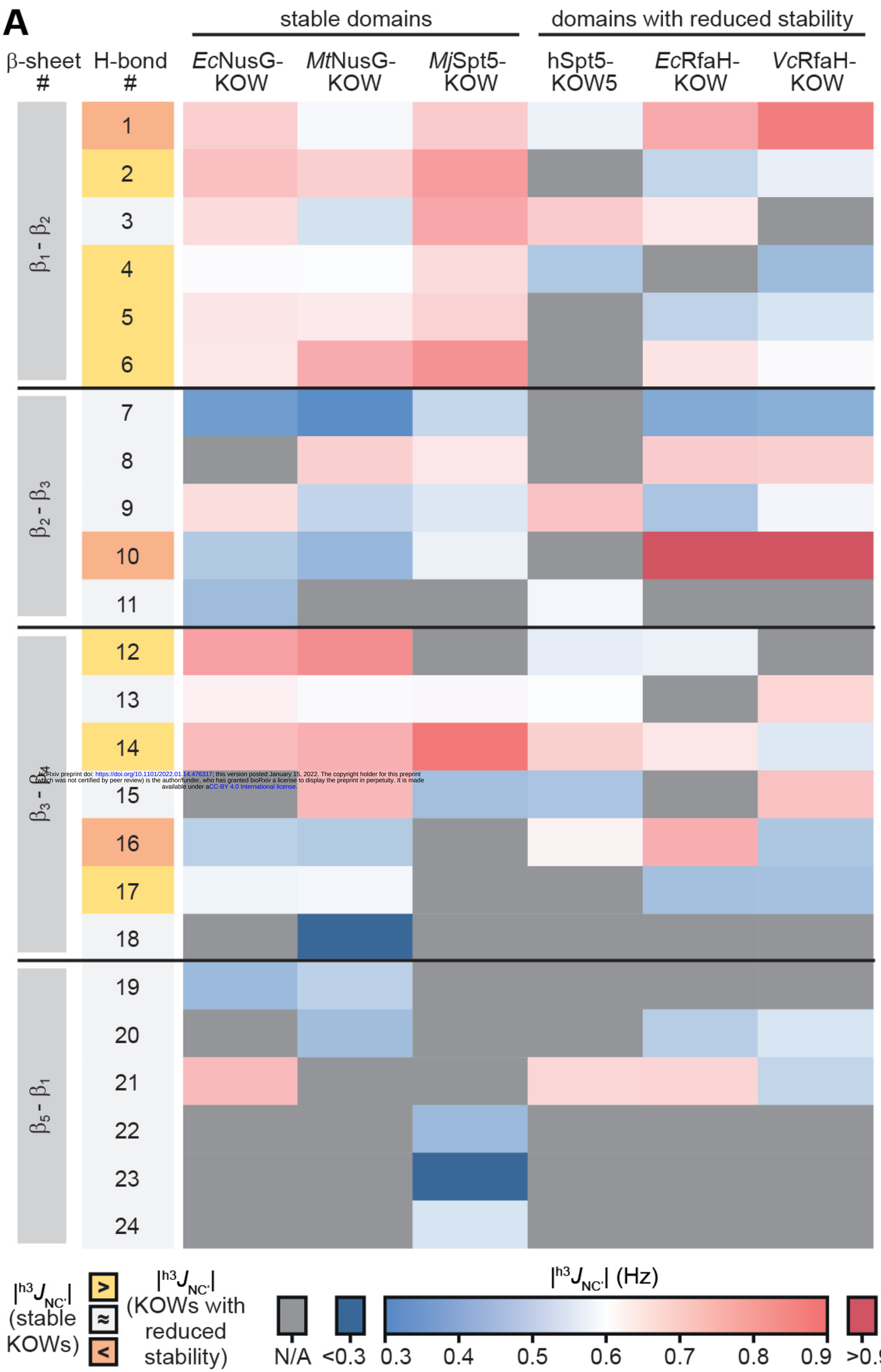

B

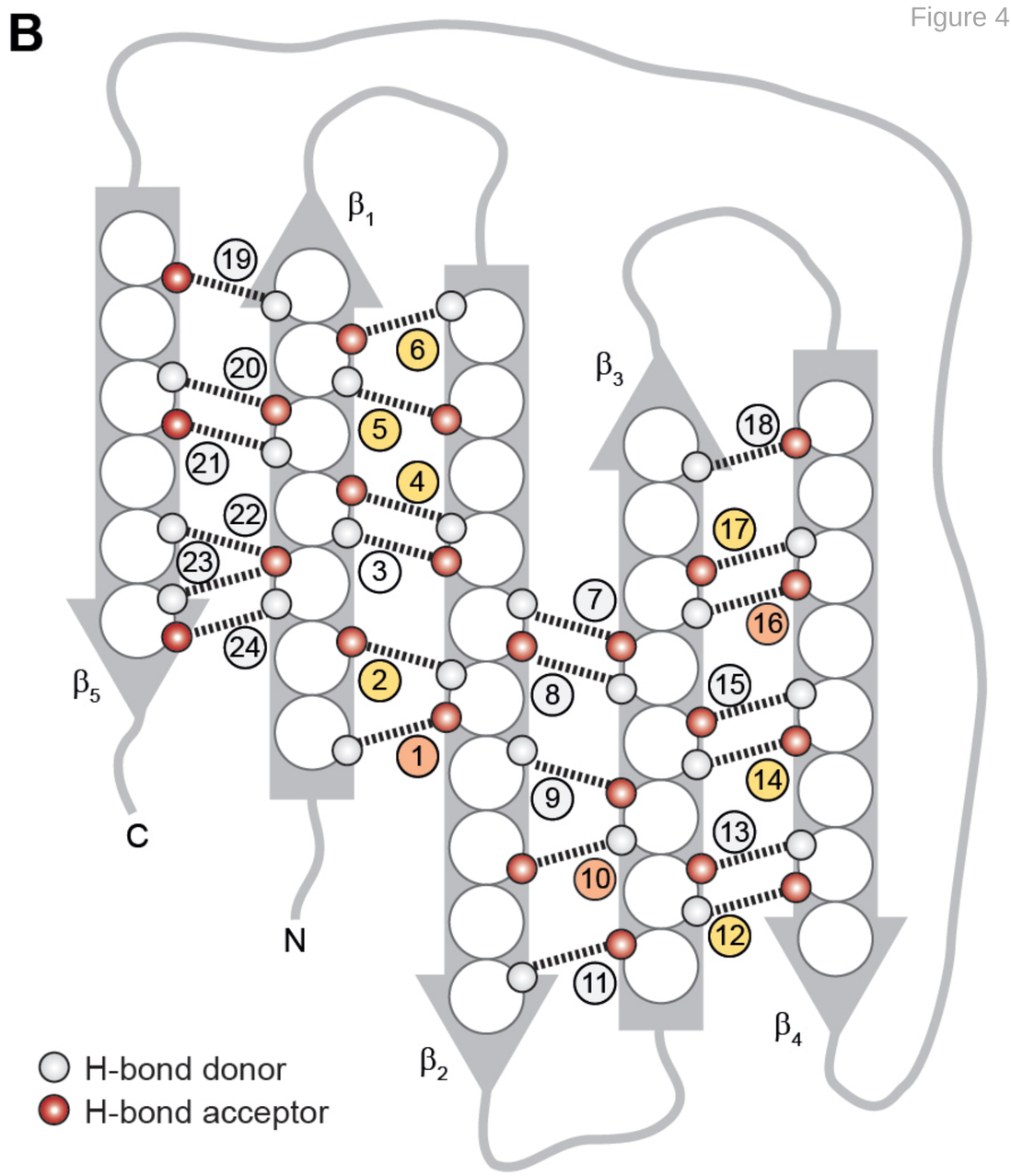

C

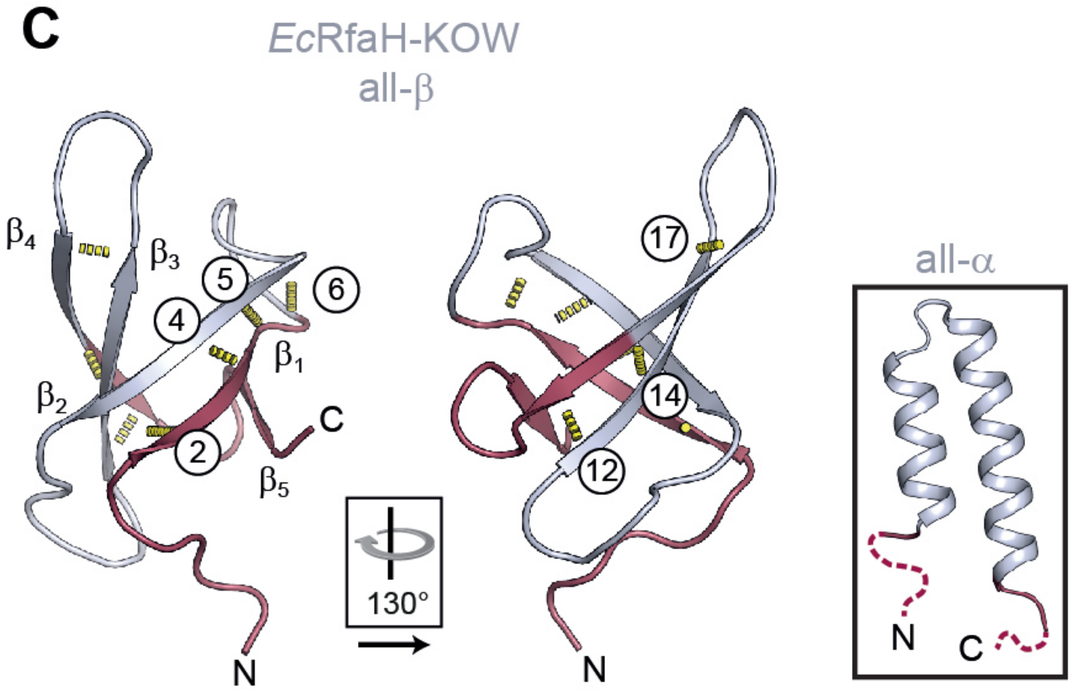

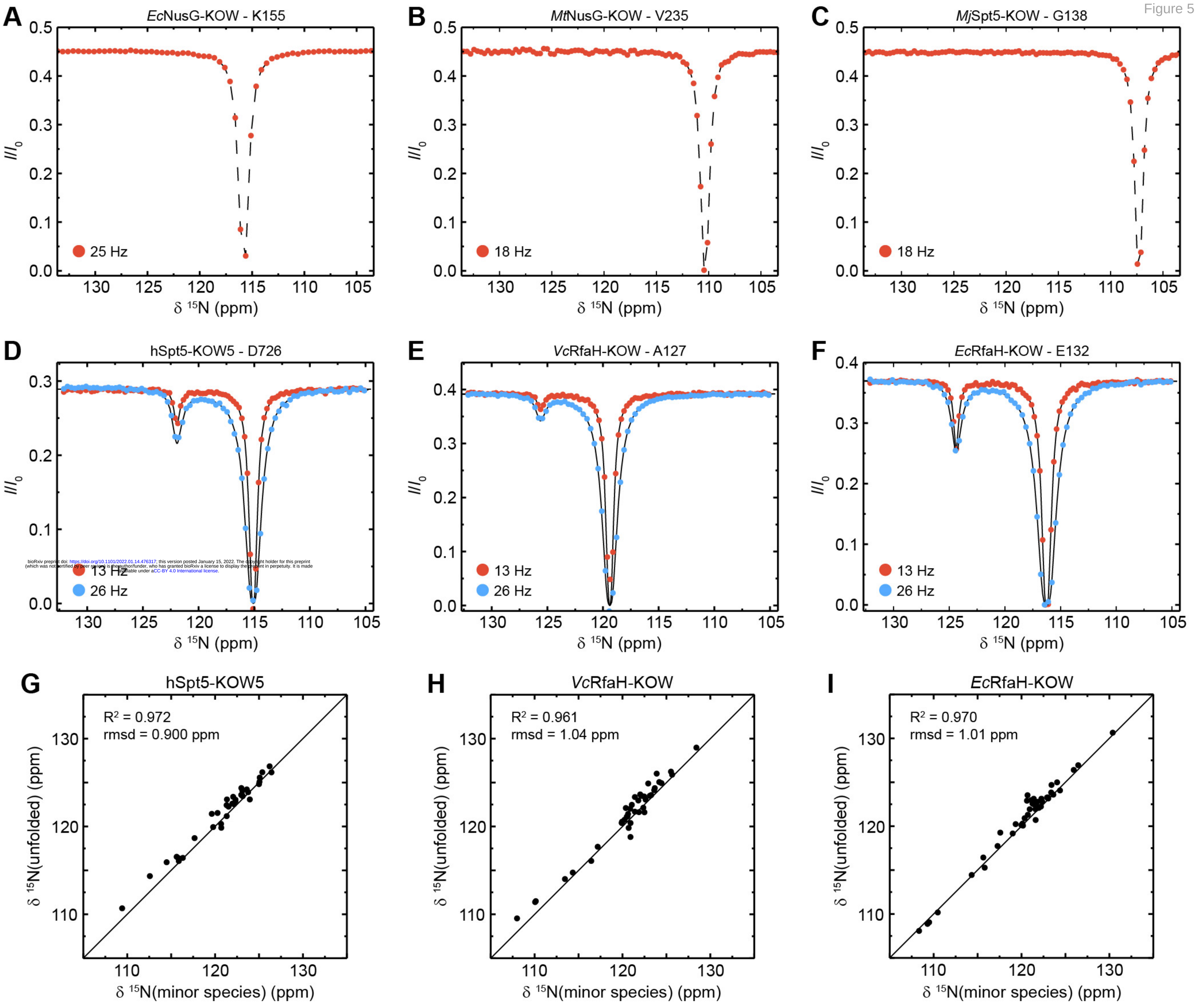

A

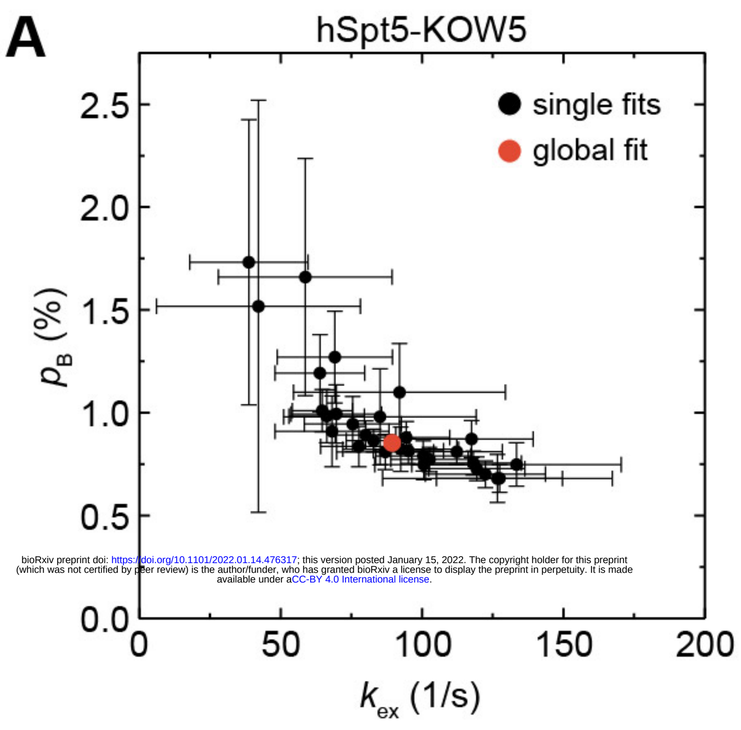

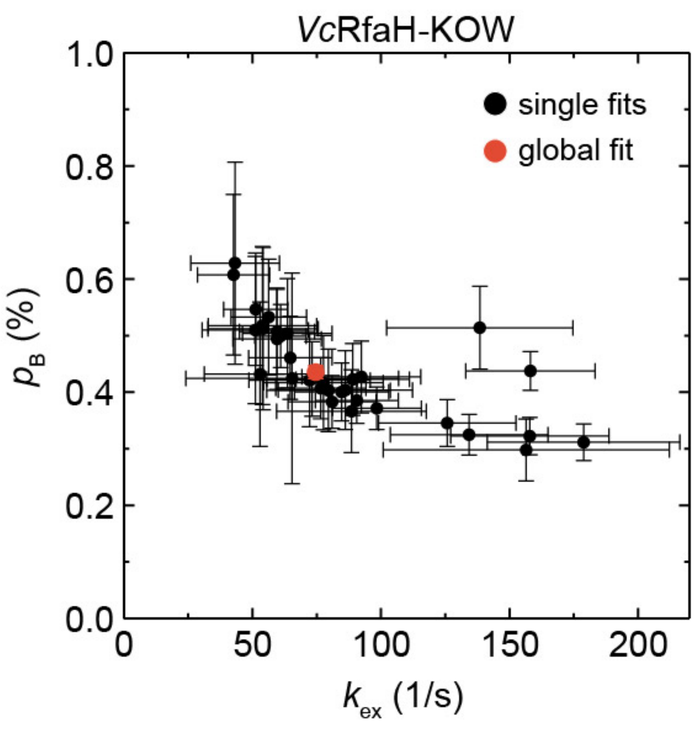

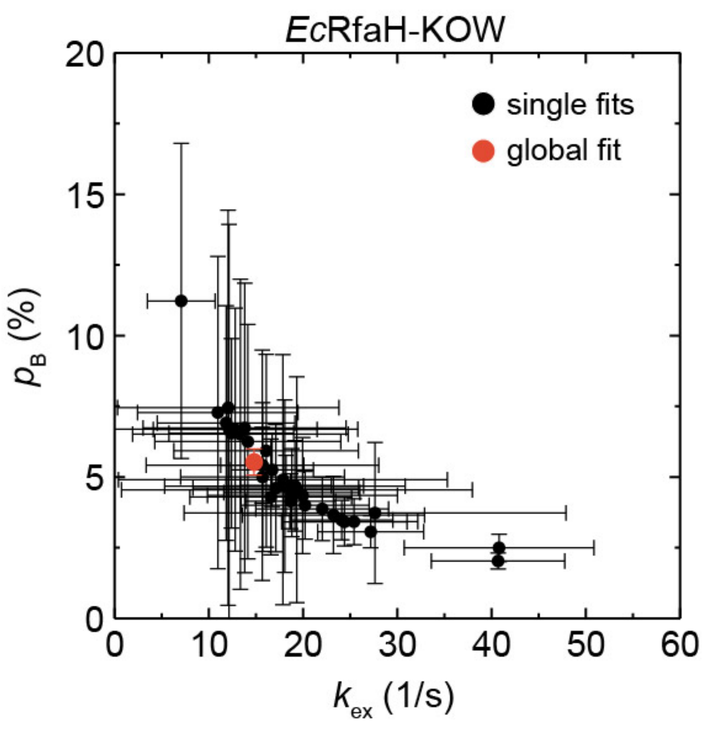

B

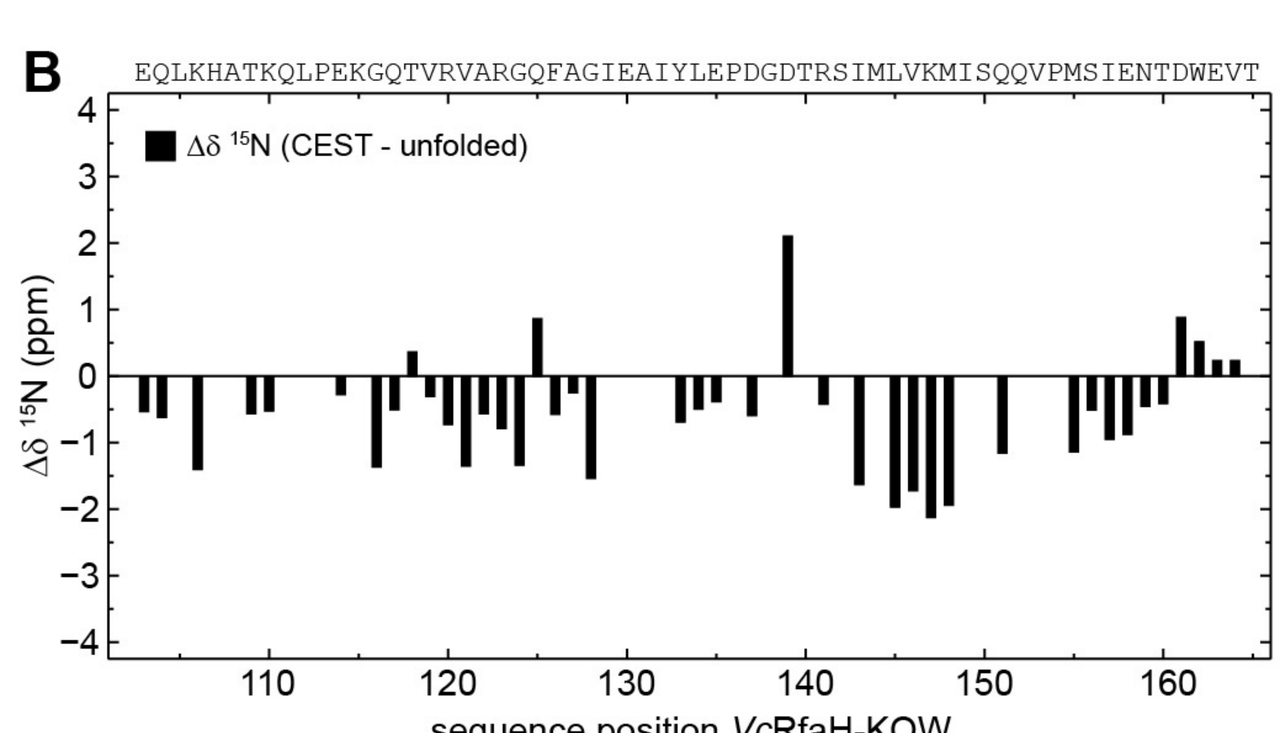

C

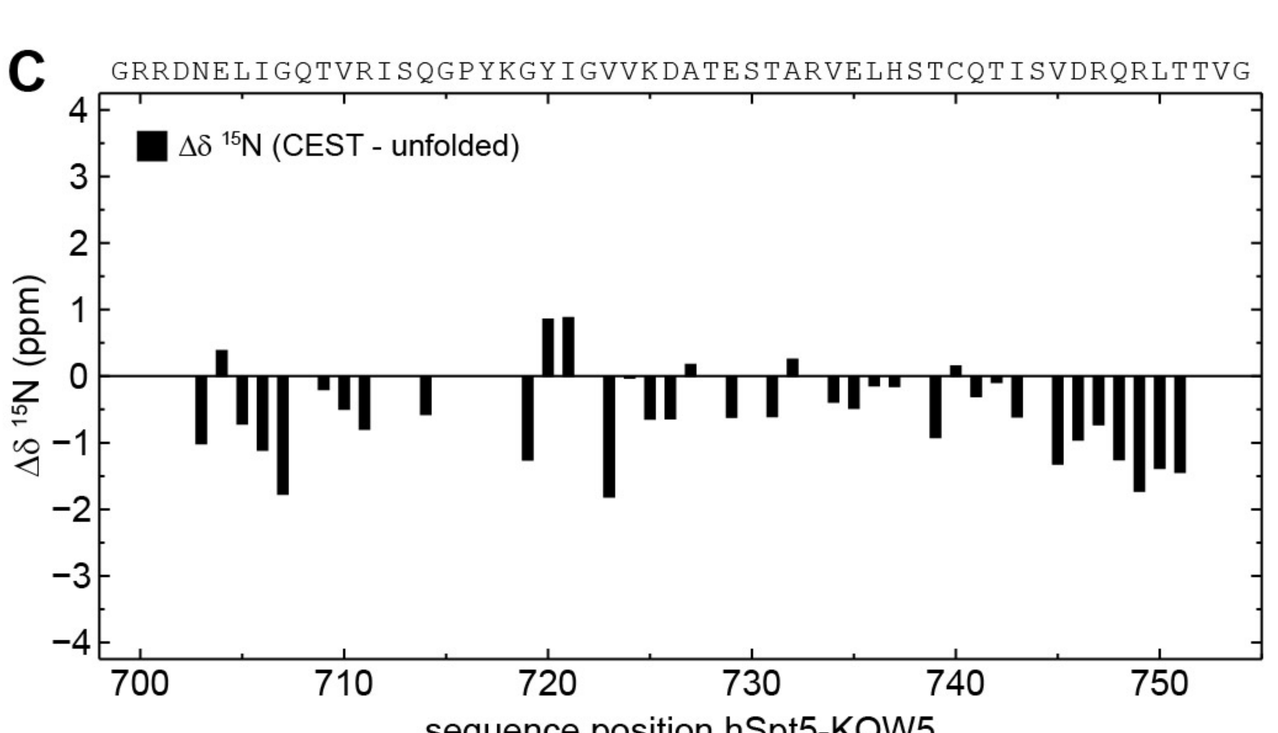

*Ec*NusG-KOW

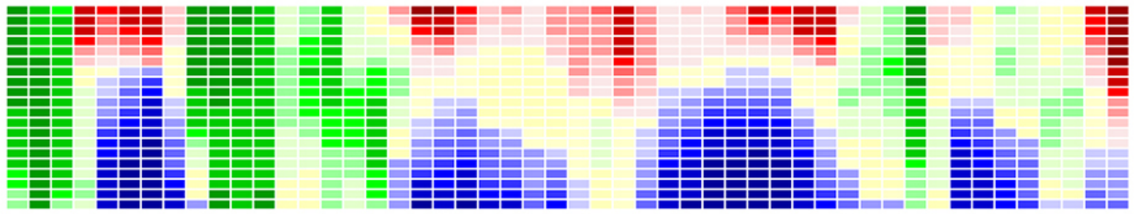

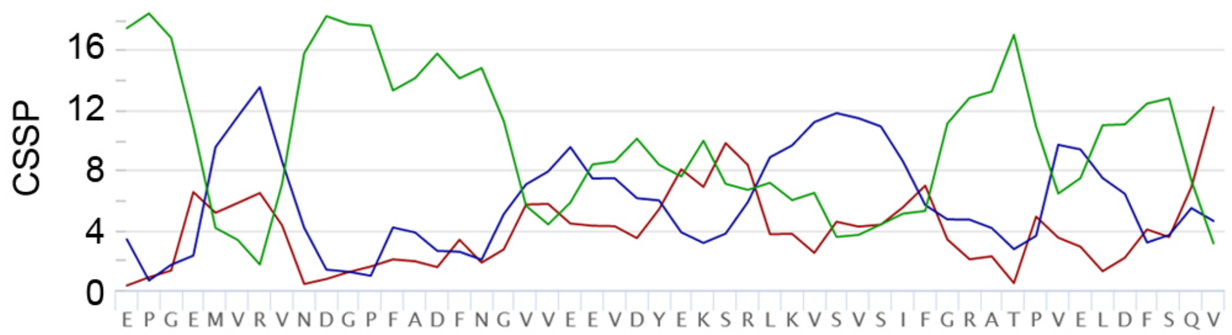

hSpt5-KOW5

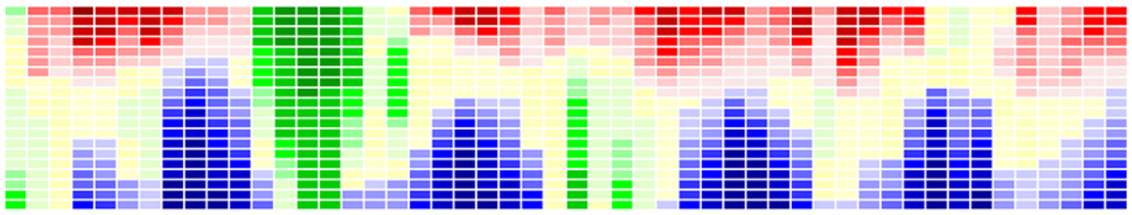

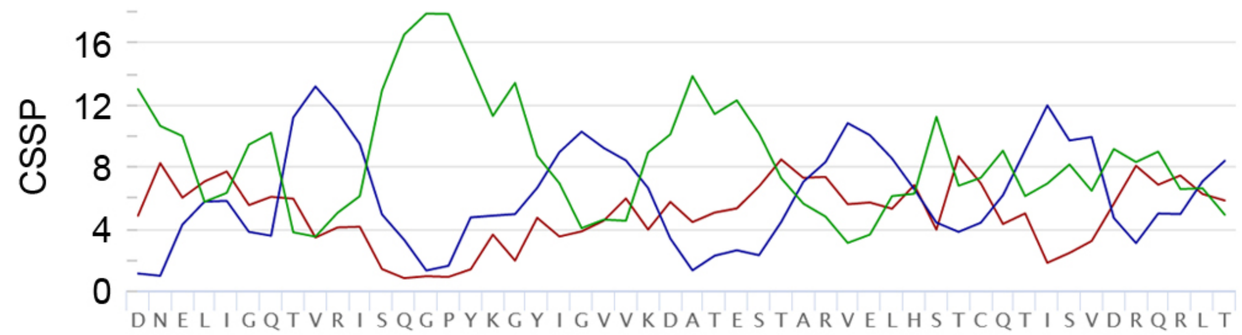

*Mt*NusG-KOW

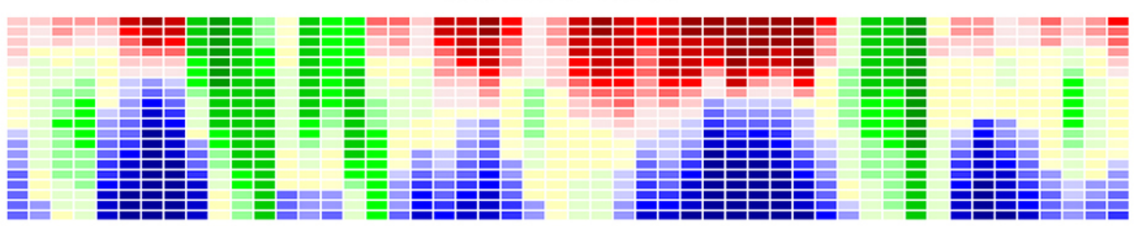

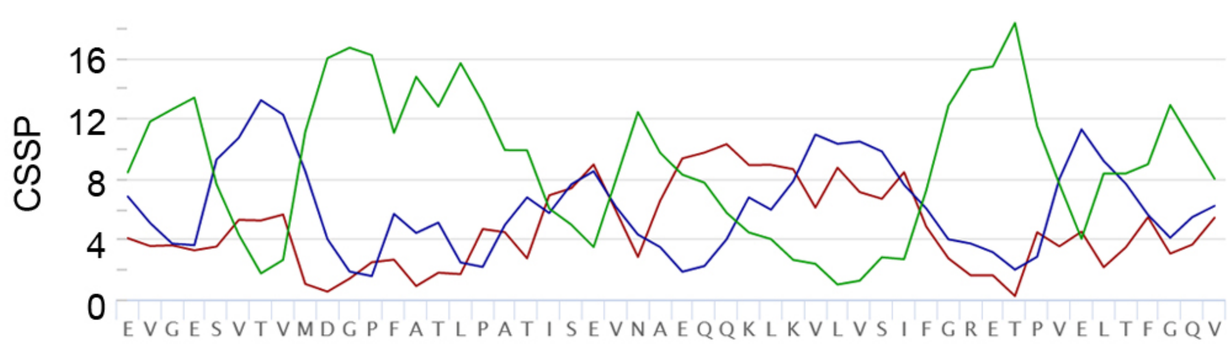

*Vc*RfaH-KOW

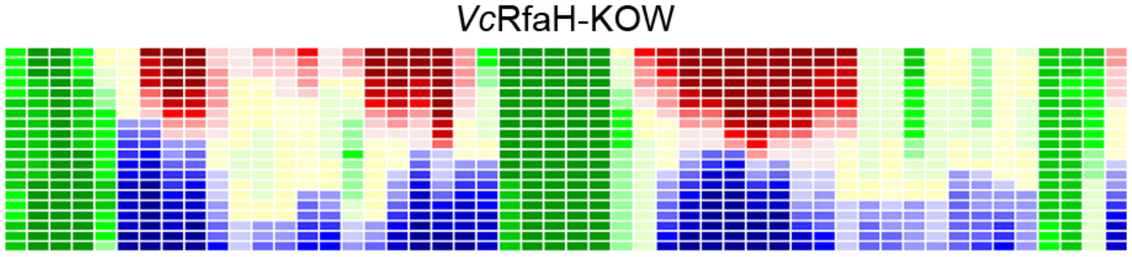

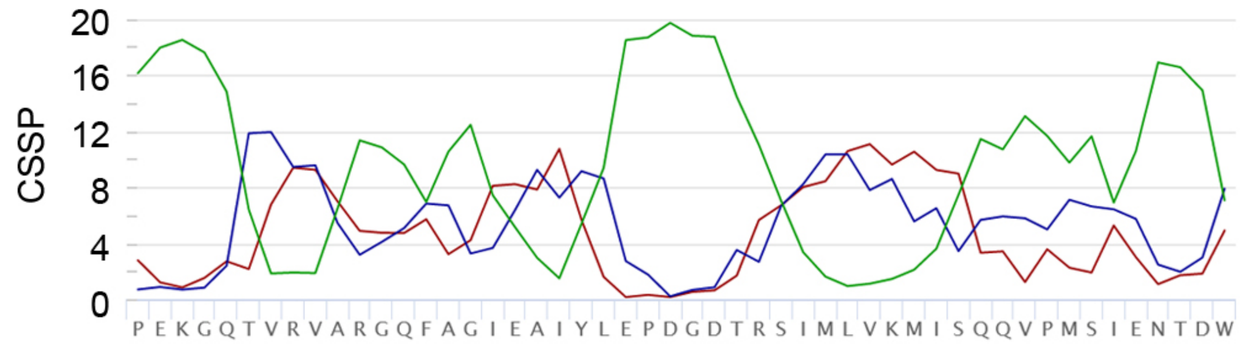

*Mt*NusG-KOW

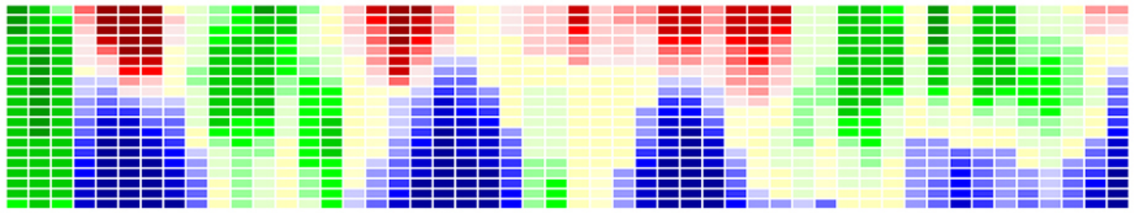

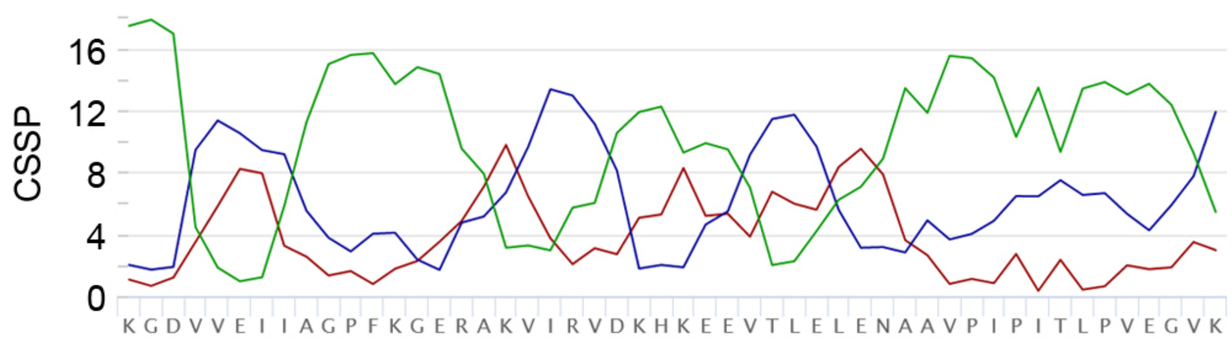

*Ec*RfaH-KOW

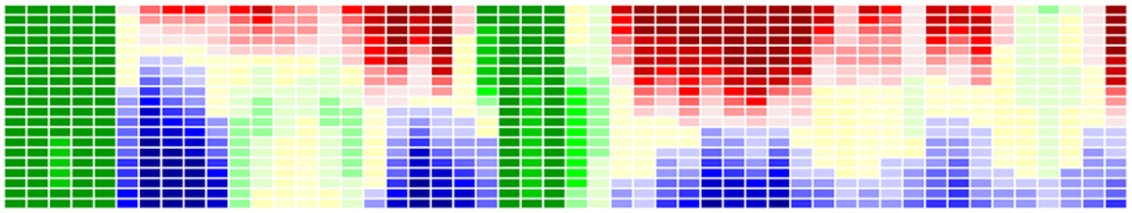

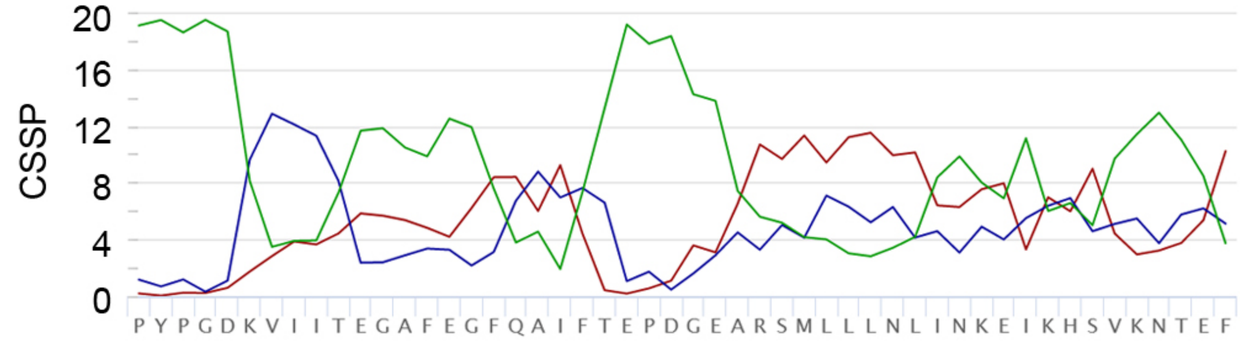

Secondary structure propensities (top)

Helix propensity

Sheet propensity

Random coil propensity

CSSP values (bottom)

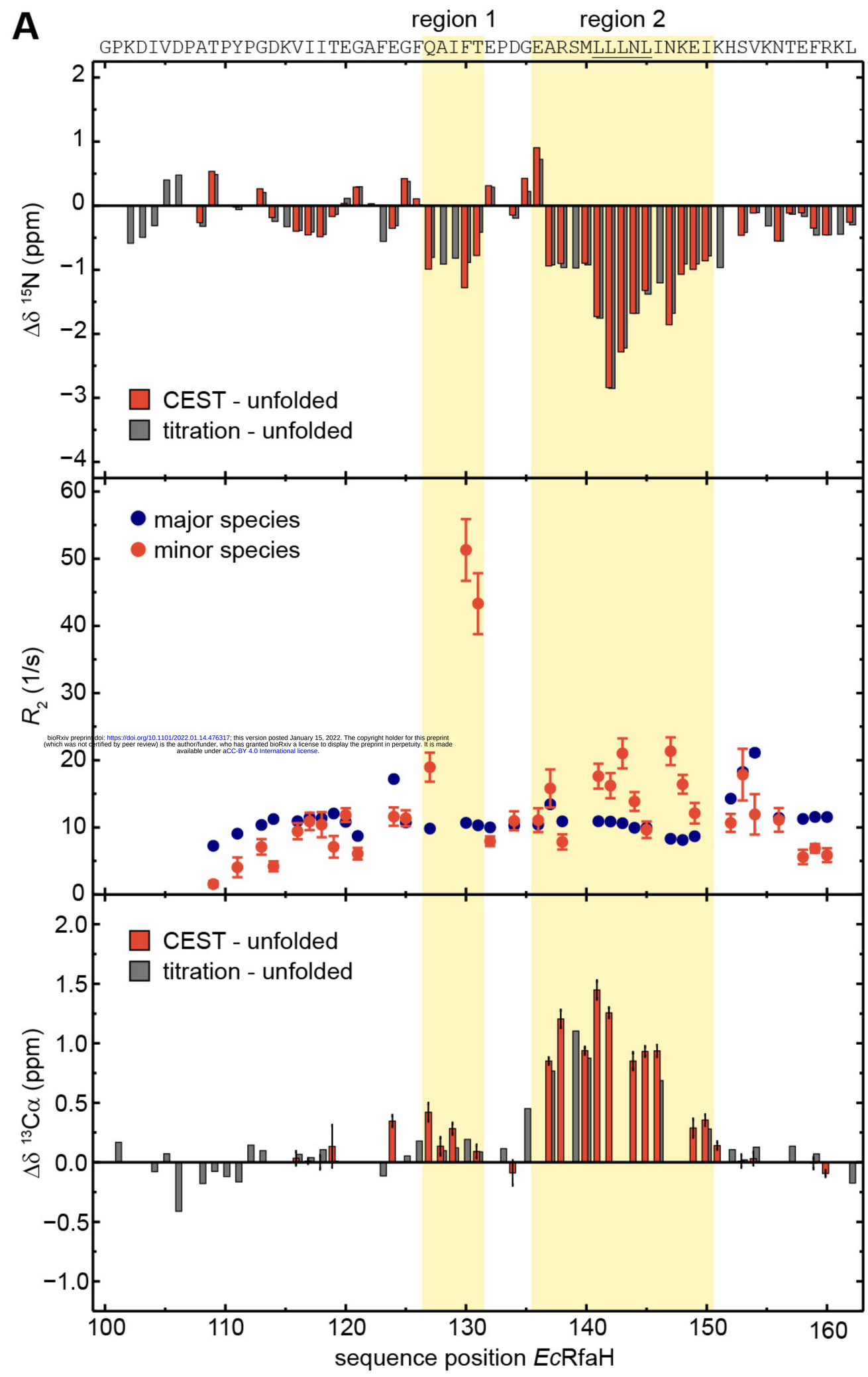

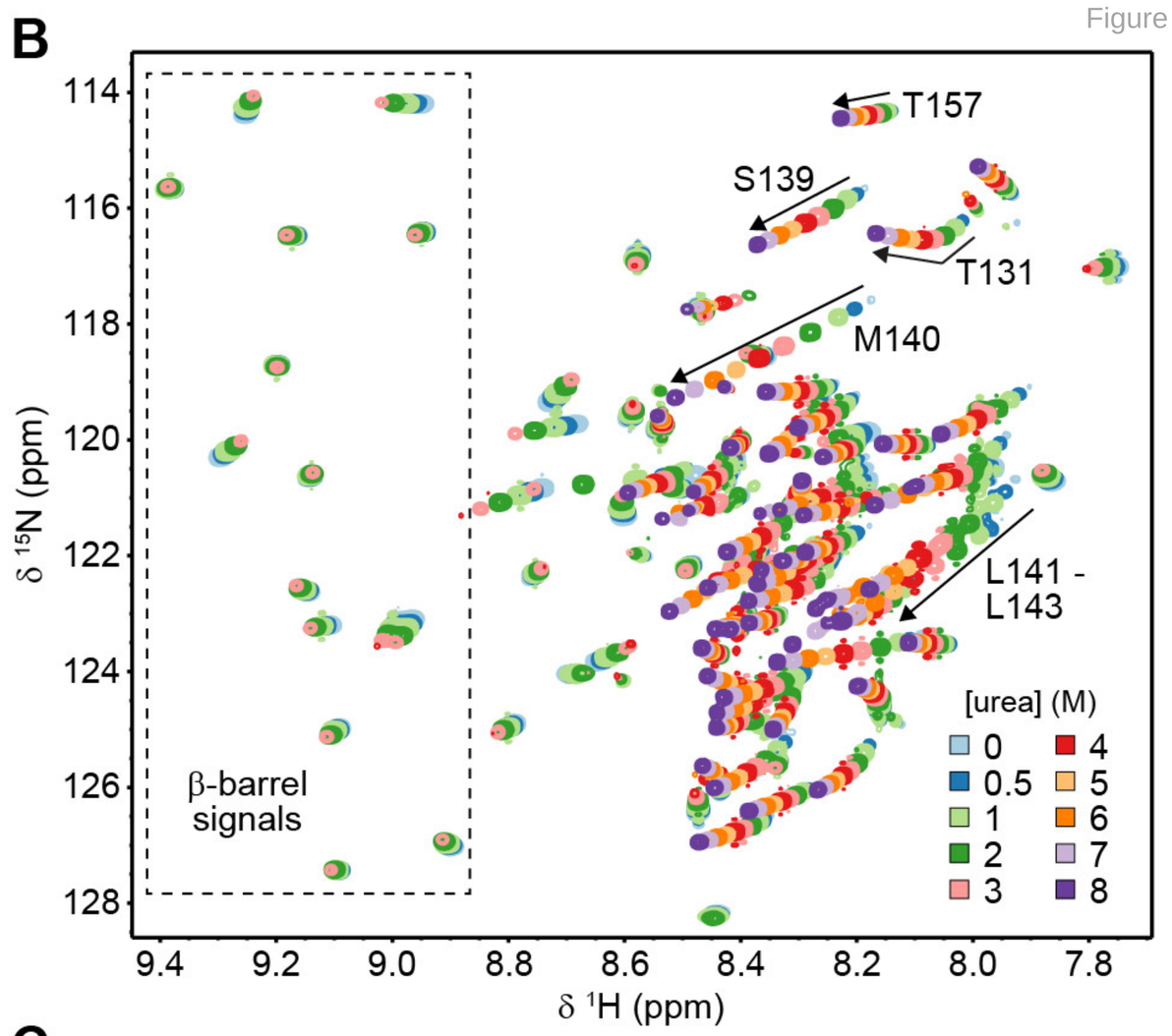

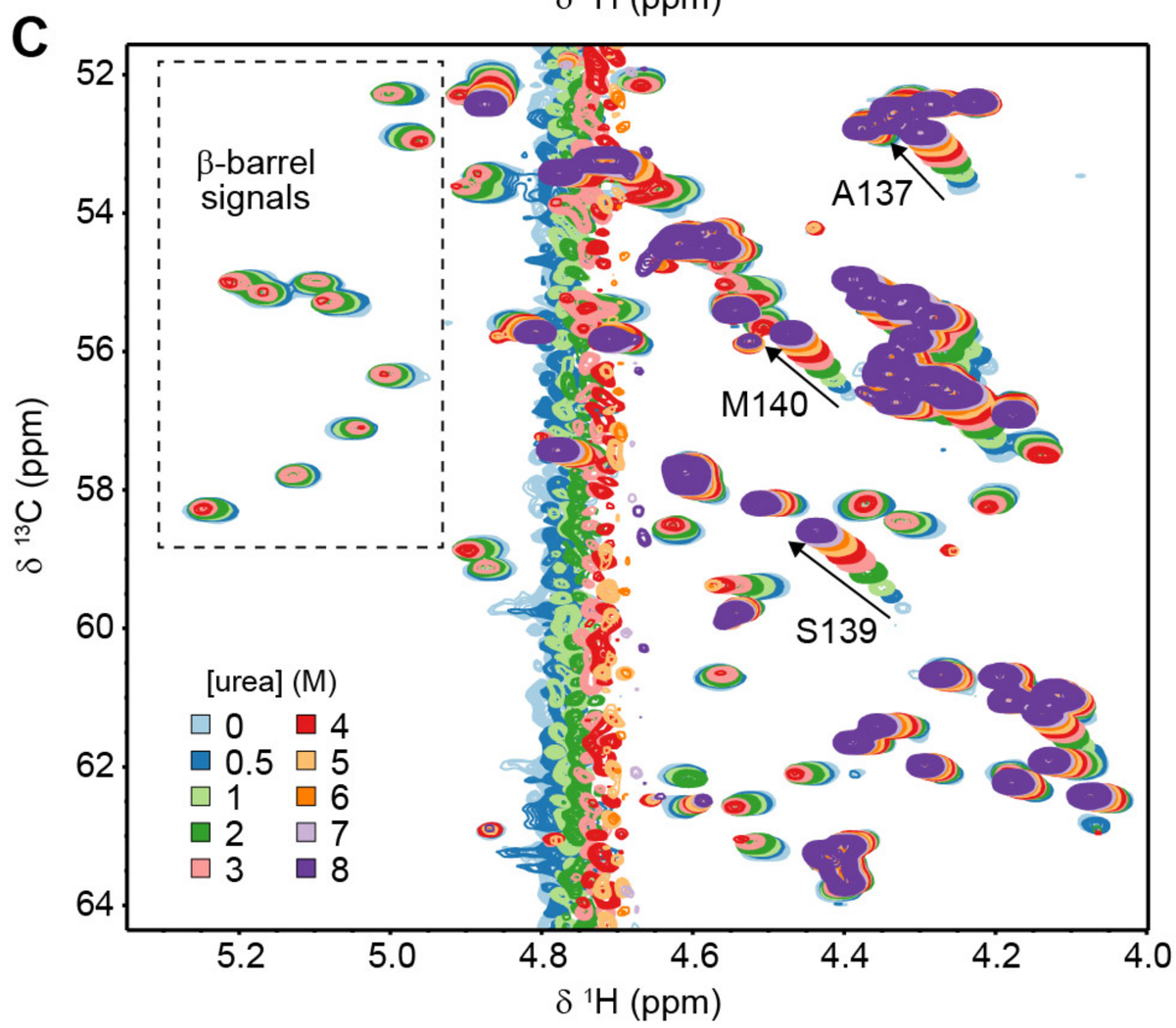

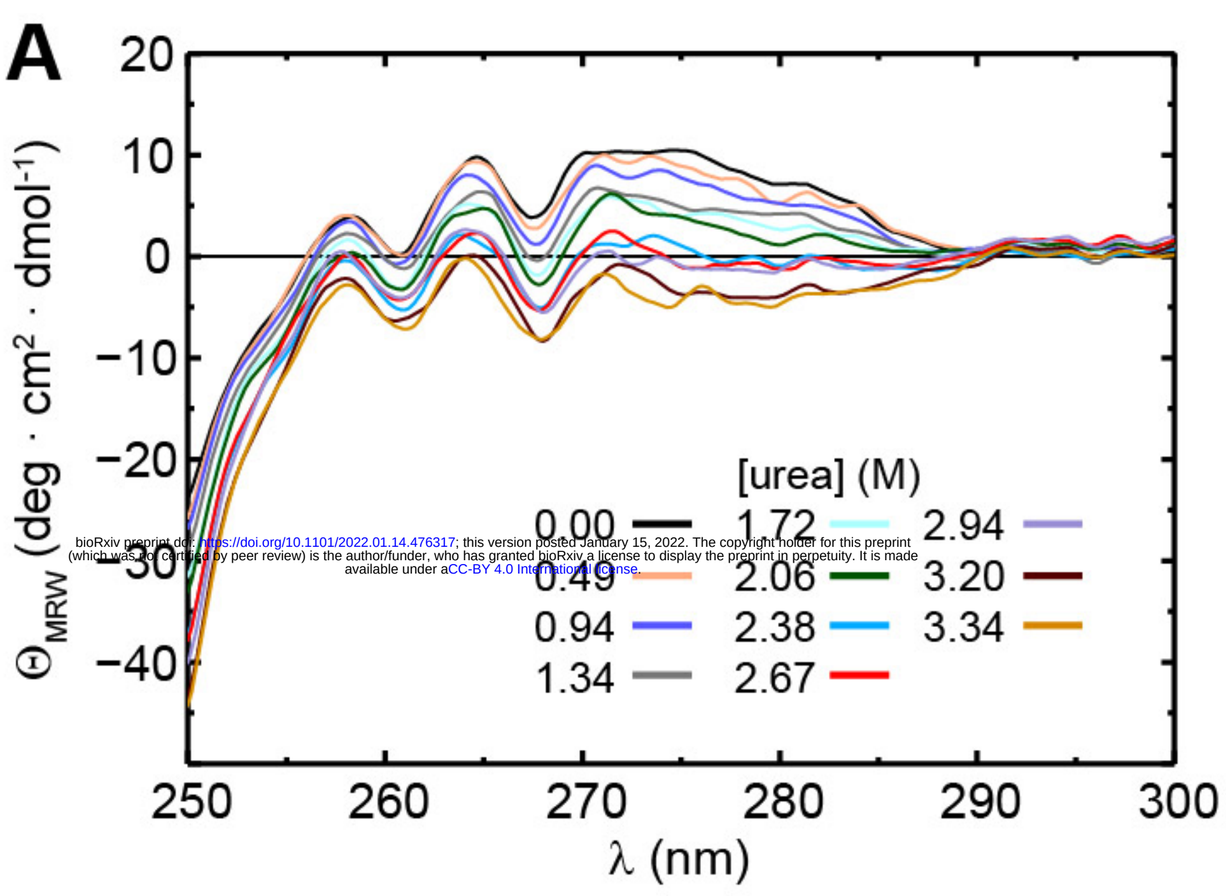

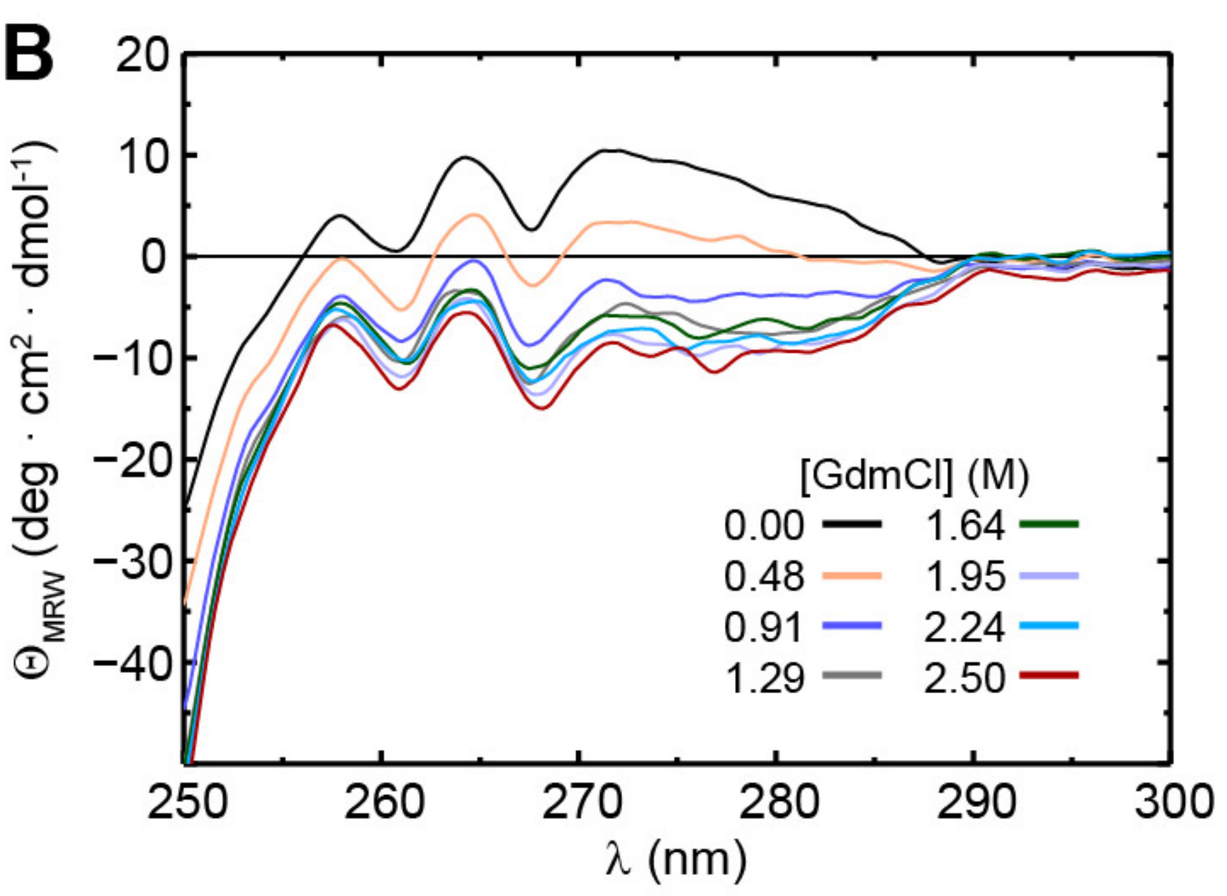

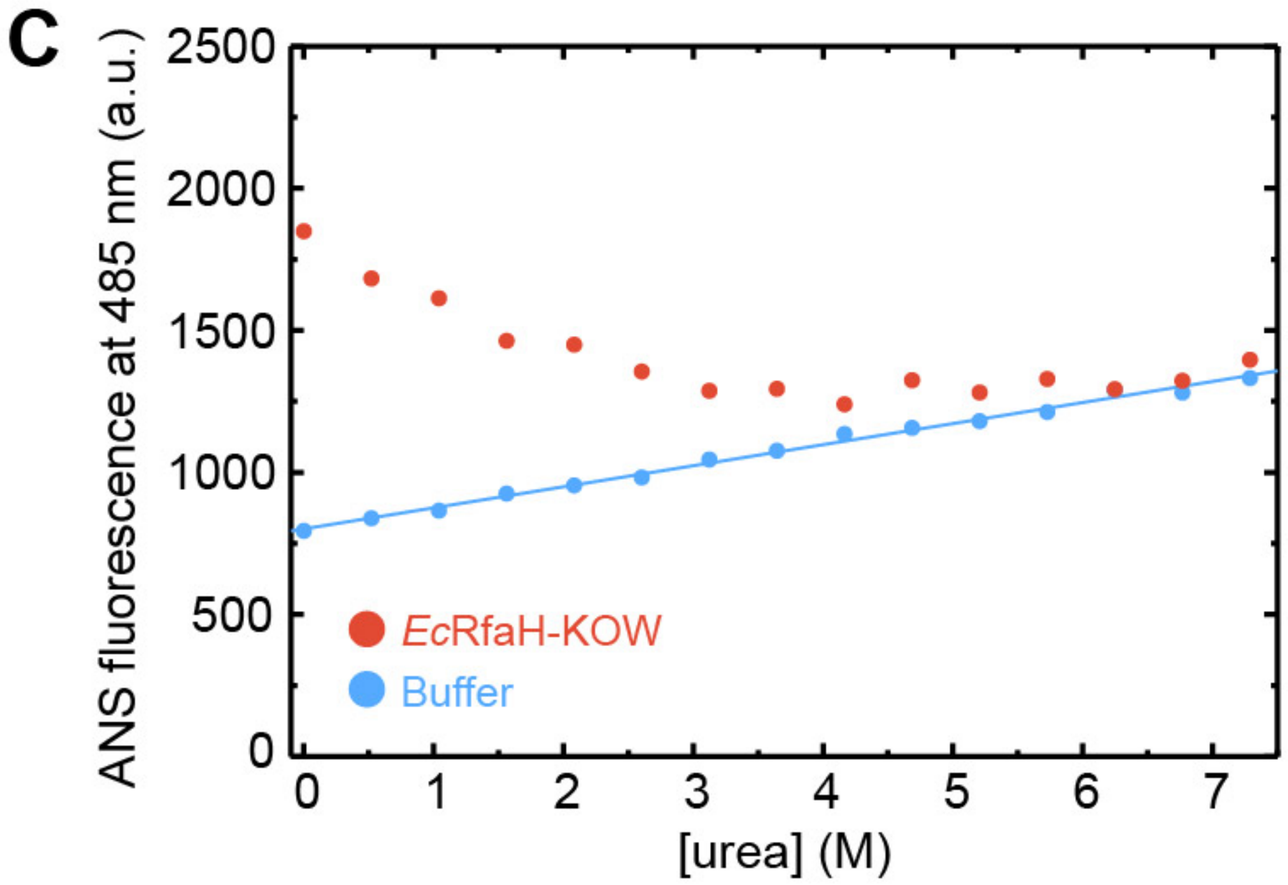

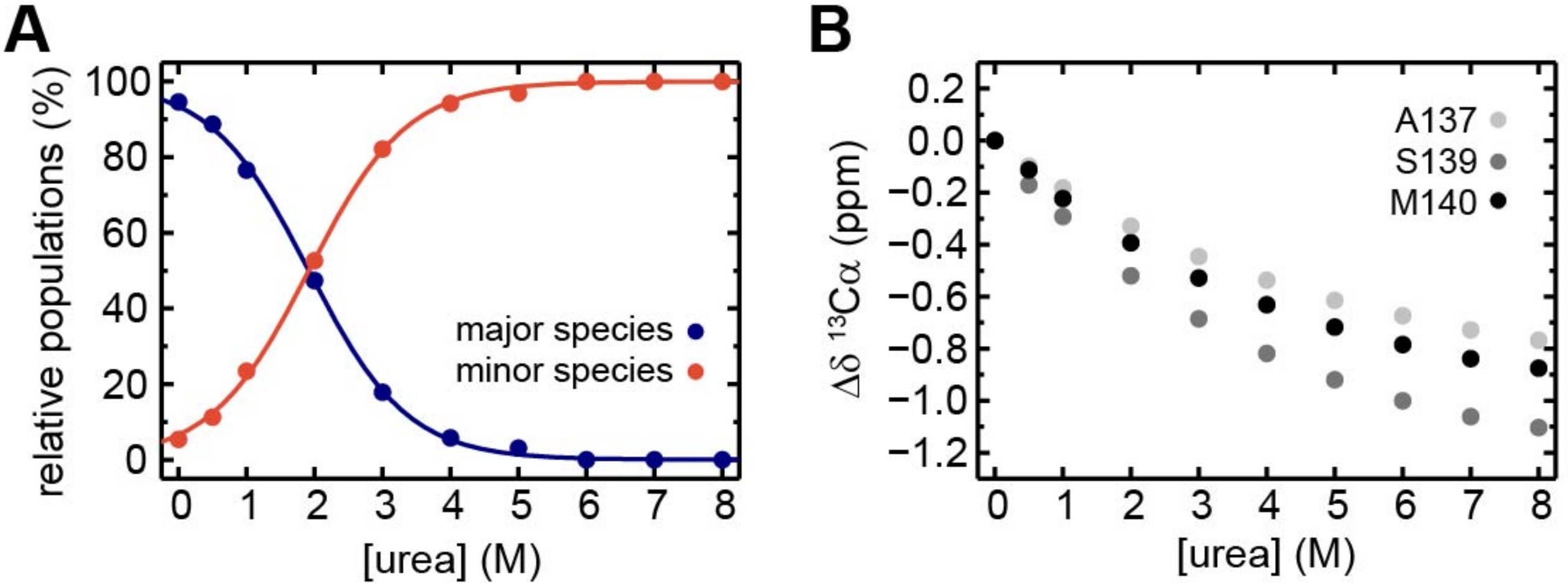
A
relative populations (%)
100
80
60
40
20
0
0 1 2 3 4 5 6 7 8
[urea] (M)
major species
minor species
B
Δδ ¹³Cα (ppm)
0.2
0.0
−0.2
−0.4
−0.6
−0.8
−1.0
−1.2
0 1 2 3 4 5 6 7 8
[urea] (M)
A137
S139
M140